The influence of thermodynamic versus dynamic processes on sea ice thickness in observations and models

By

James F. Anheuser

A dissertation submitted in partial fulfillment of

the requirements for the degree of

Doctor of Philosophy

(Atmospheric and Oceanic Sciences)

at the

UNIVERSITY OF WISCONSIN-MADISON

2022

Date of final oral examination: 11/28/2022

The dissertation is approved by the following members of the Final Oral Committee:
    Tristan L'Ecuyer, Professor, Atmospheric and Oceanic Sciences
    Jeff Key, Adjunct Professor, Atmospheric and Oceanic Sciences
    Elizabeth Maroon, Assistant Professor, Atmospheric and Oceanic Sciences
    Till Wagner, Assistant Professor, Atmospheric and Oceanic Sciences
    Jon Martin, Professor, Atmospheric and Oceanic Sciences
    Dan Vimont, Professor, Nelson Institute Center for Climatic Research
    Yinghui Liu, Physical Scientist, National Oceanic and Atmospheric Administration

Abstract

The influence of thermodynamic versus dynamic processes on sea ice thickness in observations and models

by James F. Anheuser

Sea ice thickness is affected by thermodynamic growth via phase change and dynamic effects via movement of ice parcels. Independent observational datasets of each are essential for model validation and accurate projections of future sea ice conditions. By linking an algorithm for retrieving snow–ice interface temperature from passive microwave satellite data to a thermodynamic sea ice energy balance relation known as Stefan's Law, I have developed a retrieval method for estimating thermodynamic sea ice thickness growth from space: Stefan's Law Integrated Conducted Energy (SLICE). The advantages of the SLICE retrieval method include daily basin-wide coverage, no atmospheric reanalysis product input requirement, and a potential for use beginning in 1987. Validation of the retrieval against daily sea ice thickness growth rates from ten ice mass balance buoys show a mean correlation of 0.71 and a mean bias of 0.0004 m d^{-1}. Next, I partition weekly overall sea ice growth rates from 2010 to 2021 into thermodynamic and dynamic sea ice thickness effects. Basin-wide estimates of thermodynamic effects are determined using the SLICE methodology and dynamic effects are calculated as the difference between these thermodynamic effects and overall growth from a weekly satellite altimeter-based sea ice thickness dataset. Climatological thermodynamic growth varies from less than 0.04 m wk^{-1} in the central Arctic to greater than 0.08 m wk^{-1} in the seasonal ice zones. Positive climatological dynamic effects of greater than

0.04 m wk^{-1} are found north of the Canadian Arctic Archipelago where the Transpolar Drift and Beaufort Gyre deposit ice and are twice the effects of thermodynamics in some regions. Last, in a comparison between four model simulations and this climatology of thermodynamic and dynamic sea ice thickness effects, all model datasets exhibit similar patterns of underestimated dynamic sea ice thickness increase and overestimated thermodynamic sea ice thickness growth in the central Arctic. The opposite pattern is found in the regions where the Transpolar Drift originates and in the Chukchi, Barents and Kara Seas. These patterns of thermodynamic growth and dynamic effect sum to an overall sea ice thickness change and overall sea ice thickness patterns that more closely match observations than the individual processes themselves.

"I want to know God's thoughts."

Albert Einstein

For Eliza

Acknowledgements

This work is as much mine as it is that of my advisors and committee, my colleagues, my family and my friends. Particular recognition goes to my wife, whose encouragement years ago, support during the last few years and patience as I completed this work form the foundation upon which this document was built. To all of you, thank you.

Portions of Chapter 1, Chapter 2 and Chapter 3 have been published as a part of:
Anheuser, J., Y. Liu, and J. Key, 2022: A simple model for daily basin-wide thermodynamic sea ice thickness growth retrieval. The Cryosphere, 16, 4403–4421, doi:10.5194/tc-16-4403-2022.
All authors together conceived of the idea to use satellite retrieved snow–ice interface in a sea ice thickness satellite retrieval method. JA completed all analysis and wrote the first draft under guidance from YL and JK. All authors worked together towards a final draft.

Portions of Chapter 2 and Chapter 4 have been published as a part of:
Anheuser, J., Liu, Y., and Key, J. R.: A climatology of thermodynamic vs. dynamic Arctic wintertime sea ice thickness effects during the CryoSat-2 era, The Cryosphere Discuss. [preprint], doi:10.5194/tc-2022-218, in review, 2022.
JA completed all analysis and wrote the first draft under guidance from YL and JK. All authors worked together towards a final draft.

Contents

List of Figures

List of Tables

Abbreviations

AEM	Airborne ElectroMagnetic
AMOC	Atlantic Meridional Overturning Circulation
AMSR	Advanced Microwave Scanning Radiometer
ATM	Airborne Topographic Mapper
AVHRR	Advanced Very High Resolution Radiometer
AWI	Alfred Wegener Institute
CAM	Community Atmosphere Model
CESM	Community Earth System Model
CESM1-LE	Community Earth System Model Version 1 Large Ensemble
CESM2-LE	Community Earth System Model Version 2 Large Ensemble
CHINARE	Chinese National Arctic Research Expedition
CICE	Community Ice Code
CMIP	Community Model Intercomparison Project
CPOM	Centre for Polar Observation and Modelling
CRREL	Cold Regions Research and Engineering Laboratory
CS2SMOS	CryoSat-2/SMOS sea ice thickness product
EASE	Equal-Area Scalable Earth
ECMWF	European Centre for Medium-Range Weather Forecasts
ESA	European Space Agency
FOSI	Forced Ocean Sea Ice
FYI	First Year Ice

GOCC	Generalized Orthogonal Curvilinear Coordinate
GSFC	Goddard Space Flight Center
IABP	International Arctic Buoy Program
ICESat	Ice, Cloud and land Elevation Satellite
IMB	Ice Mass Balance buoy
JAXA	Japan Aerospace Exploration Agency
JRA	Japanese Atmospheric Reanalysis
LANL	Los Alamos National Laboratory
MIRAS	Microwave Imaging Radiometer using Aperture Synthesis
MIZ	Marginal Ice Zone
MOSAiC	Multi-disciplinary drifting Observatory for the Study of Arctic Climate
MYI	Multi-Year Ice
N-ICE2015	Norwegian young ICE
NASA	National Aeronautic and Space Administration
NCAR	National Center for Atmospheric Research
NCEP	National Centers for Environmental Protection
NOAA	National Oceanic and Atmospheric Administration
NSIDC	National Snow and Ice Data Center
OMIP	Ocean Model Intercomparison Project
OIB	Operation Ice Bridge
PIOMAS	Pan-Arctic Ice–Ocean Modeling and Assimilation System
POP	Parallel Ocean Program
RCP	Representative Concentration Pathway
RGPS	RADARSAT Geophysical Processor System
RMSE	Root Mean Squared Error
SHEBA	Surface HEat Budget of the Arctic Ocean
SIRAL	SAR/Interferometric Radar Altimeter
SITU	Sea Ice Tracking Utility
SLICE	Stefan's Law Integrated Conducted Energy

SMMR	Scanning Multichannel Microwave Radiometer
SMOS	Soil Moisture Ocean Salinity
SSM/I	Special Sensor for Microwave Imager
SSMIS	Special Sensor Microwave Imager/Sounder
SSP	Shared Socioeconomic Pathway
SST	Sea Surface Temperature
TED	Thickness and Enthalpy Distribution
ULS	Upward Looking Sonar
WCRP	World Climate Research Programme

Chapter 1

Introduction

In a phenomenon known as Arctic Amplification, the Arctic region is warming at a faster rate than any other region on Earth (Bekryaev et al., 2010; Taylor et al., 2022). While the causes of Arctic Amplification remain under investigation (Pithan and Mauritsen, 2014), changes to Arctic climate are manifest in temperature, precipitation, and sea ice (Box et al., 2019). In particular, sea ice area, thickness and age have all decreased substantially in recent decades (Stroeve and Notz, 2018). The presence of sea ice significantly increases the albedo of the ocean, meaning this observed reduction in sea ice leads to the ocean absorbing more shortwave radiation. This positive ice-albedo climate feedback is a likely contributor to Arctic Amplification (Jenkins and Dai, 2021; Screen and Simmonds, 2010). Sea ice also impacts the exchange of energy, momentum and mass between the ocean and

the atmosphere, further stressing the importance of understanding sea ice and its role in the current and future climate system.

Individual sea ice parcels experience thermodynamic processes that affect their thickness via phase change and dynamic processes that affect thickness via their motion. Thorndike et al. (1975) provides a governing equation for sea ice thickness that accounts for both of these thermodynamic and dynamic effects. This equation serves as the basis for modern sea ice thickness modelling and is as follows:

$$\frac{\partial g}{\partial t} = \frac{\partial}{\partial h}(fg) - \nabla \cdot (\mathbf{u}g) + \psi \,, \tag{1.1}$$

where g is a thickness distribution, t is time, f is a function of time, thickness and position vector $\mathbf{x}$ describing thermodynamic sea ice thickness increase, $\mathbf{u}$ is the ice motion vector and ψ is a thickness redistribution function. The thickness distribution, g, allows for thickness within a grid cell to be defined by a distribution of thicknesses that is discretized by some number of thickness categories, meaning the entire grid cell need not be the same thickness. The thickness redistribution function, ψ, moves grid cell area between thickness categories through the formation of ridges and fractures (known in sea ice science as leads) in order to conserve area and volume. The thickness distribution and thickness redistribution functions are found in modern sea ice models. Thorndike et al. (1975) also highlights the importance of both thermodynamic and dynamic processes in shaping the observed ice pack—while thermodynamic effects seek to reach an equilibrium thickness value, dynamic processes seek the extreme thickness values.

The thermodynamics of sea ice thickness growth were first described by Stefan (1891). The key insight described by the author is that sea ice thickness growth at the bottom of the ice layer is controlled by the vertical temperature gradient at this lower interface, a fundamental characteristic of sea ice growth that is universally accepted today. The authors describe the conduction of the latent heat of fusion released from the bottom boundary of the sea ice layer where growth is occurring to the top boundary of the sea ice layer. In the first published mathematical description of sea ice thermodynamics, the authors set a latent heat of fusion term equal to a conduction term, defined only by boundary condition temperatures at the top and bottom of the ice (which is set to the freezing point temperature). This relationship is now known as Stefan's Law. Stefan's Law in this basic form requires the following assumptions: neglect horizontal conduction, neglect thermal inertia, neglect internal heat sources, and neglect heat flux from the ocean to the ice. Stefan's Law is a useful relationship for many multi-phase systems, even beyond sea ice growth.

Major advancements to the mathematical description of sea ice growth were next made with the advent of numerical modelling (Untersteiner, 1964; Maykut and Untersteiner, 1971). The nodal structure of numerical modelling allowed for the vertical temperature profile in the ice to be defined at many more vertical positions beyond the two boundary conditions within Stefan's Law, allowing for the inclusion of thermal inertia and internal heat sources. These one-dimensional numerical modelling frameworks also included other heat terms such as a term for heat flux from the ocean to the ice and various radiative terms. In Maykut and Untersteiner (1971), this more complete representation of the sea ice system is forced

by a typical central Arctic seasonal cycle and the model is run until a temperature and ice thickness seasonal cycle equilibrium is reached. The results of this exercise, a 288 cm equilibrium thickness and 40 cm equilibrium annual ablation, are reasonable and agreed well with contemporary observed seasonal cycles. Maykut and Untersteiner (1971) continues to form the foundation of thermodynamic sea ice modelling today.

The model structure described by Maykut and Untersteiner (1971) was too complex for large scale modelling using computers at the time. To address this, Semtner (1976) proposed a simplified interpretation that reduced the vertical snow and ice temperature profile to only three points, reducing the total data points by 90%. This three-layer model reproduced the results from Maykut and Untersteiner (1971) within 10 inches of thickness in 75% of cases. In the appendix to Semtner (1976), the author proposes a further simplification of this three-layer model in the form of a zero-layer model. This zero-layer model reduces temperature profile tracking to a singular, snow–ice interface temperature. Though this simplified model slightly distorted the annual cycle of sea ice thickness, the annual mean values are similar to those produced by the three-layer model. It was this simplified, zero-layer model that became the basis of early climate scale sea ice thickness modelling (e.g., Manabe et al., 1991). The zero-layer model is also similar to the model described in Section 3.

A complication to the treatment of sea ice as a continuous media is the inclusion of pockets of brine within the sea ice. These brine pockets disrupt the isotropic nature of both thermodynamic and mechanical sea ice properties. Bitz and Lipscomb (1999) took an important step towards addressing these effects. The size and salinity of a brine pocket changes with

the local ice temperature. In order to maintain thermal equilibrium, a decrease in local temperature prompts freezing along the brine pocket edges, increasing salinity and decreasing the size of the pocket. The opposite process occurs with an increase in ice temperature. These changes to brine pocket size change the porosity and density of the ice, which must be reflected in the specific heat in order to conserve energy. The authors find that their energy conserving model that contains a parameterization of temperature effects on specific heat results in an increase in surface ablation of 12-22% and a decrease in equilibrium sea ice thickness of 50-124 cm. The model and parameterization described in Bitz and Lipscomb (1999) is used in the global climate models described in Section 2.

A final key building block for the thermodynamics of sea ice growth in modern global climate models is the mathematical thickness growth scheme found in Lipscomb (2001). A major advantage to the sea ice thickness distribution approach from Thorndike et al. (1975) and Eq. 1.1 is the clean mathematics used to define sea ice thickness and movement within the thickness space. Lipscomb (2001) realized that when the redistribution function and sea ice motion terms are ignored, the resultant equation (representing purely thermodynamic growth) resembles the classical fluid dynamics continuity equation. With this realization in hand, the author applied a solution scheme from Dukowicz and Baumgardner (2000), originally applied to ocean dynamics, to movement within sea ice thickness space. The scheme is more computationally efficient as well as more accurate than previously demonstrated schemes. This solution strategy is also used in the global climate models described in Section 2.

Modelling of the dynamic effects on sea ice thickness begins with an understanding of the ice motion vectors. A two-dimensional momentum balance of the forces applied to an infinitesimal sea ice volume element yields a motion vector field (Hibler, 1979):

$$m\frac{\partial \mathbf{u}}{\partial t} = -mf\mathbf{k} \times \mathbf{u} + \tau_a + \tau_w - mg\nabla H + \mathbf{F} \,, \tag{1.2}$$

where m is ice mass per unit area, f is the Coriolis parameter, k is the unit vector in the direction normal to the surface plane, τ_a and τ_w are forces due to air and water stresses, respectively, H is sea surface dynamic height, g is the acceleration due to gravity and $\mathbf{F}$ is the force due to internal stresses. Especially in the ice interior, the force due to internal stresses is particularly important. Modelling the internal stresses, however, is a more difficult exercise.

Internal stresses in the ice are calculated using a constitutive law for the rheology of the ice. In material science, the rheology of a material is the relationship between the stress and strain of a material—i.e., how forces applied to a material manifest in movement within the material and vice versa. Using observations from the Arctic Ice Dynamics Joint Experiment (AIDJEX), Coon et al. (1974) proposed an elastic-plastic rheology. Under this rheology structure, a yield stress is defined, below which the material deforms elastically (may return to it's original shape) and beyond which the material deforms plastically (deformation is permanent). The local sea ice yield strength is related to sea ice thickness and concentration. During elastic deformation, the work applied to the material via stress is stored and is recovered when the deformation is reversed, while plastic deformation results in the loss of

the energy applied to the material as work. The authors contend that sea ice has strong visual similarities to other materials which have successfully been modelled using plastic or elastic-plastic rheologies, such as sand, gravel, clay, and rocks. While this rheology structure is no longer considered state of the art, it laid the framework for those that are.

The modern standard rheological model is a nonlinear viscous-plastic rheology, first proposed by (Hibler, 1979). The viscous-plastic rheology is similar to the elastic-plastic rheology, except that the stress is determined by strain rate rather than strain itself and the elastic regime is replaced by a viscous regime. The viscous regime only occurs at very low strain rates, meaning the ice is nearly always in a state of plastic yielding except at low strain rates, when the ice is nearly rigid. In these low strain rate conditions, viscosity values can become very large, introducing instabilities in the numerical solutions. To remedy this, Hunke and Dukowicz (1997) proposed an important modification that is known as the elastic-viscous-plastic rheology. The key mechanism for reduction in computation time with the elastic-viscous-plastic rheology over the viscous-plastic rheology is the replacement of the viscous regime with an elastic regime at very small, daily time scales. The elastic-viscous-plastic model reduces to the viscous-plastic rheology at wind forcing time scales. Incidentally, the authors found that not only did this modification increase computational efficiency, it also increased the accuracy of the model on the daily time scale. Hunke and Dukowicz (2002) adapted the elastic-viscous-plastic rheology for use on curvilinear coordinates and is used within the global climate models referenced in Section 2.

The final component of Eq. 1.1 is the thickness redistribution function, ψ. This function

is intended to transfer sub-grid ice area between thickness categories within the thickness distribution, g, in order to replicate the formation of ridges and leads. This function applies when the divergence term leads to total sea ice areas greater than unity or less than zero, necessitating area be transferred between thickness categories to conserve area and volume. Parmenter and Coon (1972) is an early attempt to model the ridging of sea ice using computers. Specifically, the authors use a kinematic model to model the ridging of sea ice where parcels meet. The results show that the forces required to create ridges of similar size to those found in the Arctic are similar to the forces acting on Arctic ice due to winds. However, this kinetic model is too complex for implementation in climate scale models. Thorndike et al. (1975) proposed a framework for the thickness redistribution function that stands in modern models. The redistribution is parameterized based on thickness, sub-grid thickness distribution and drift velocity. The ridging function satisfies two conditions: the total area and total volume of ice within a grid cell must be conserved. Following this, some portion of ice within the grid cell is transferred to higher thickness categories during convergence and some portion of ice within the grid cell is transferred to lower thickness categories during divergence.

Large scale validation of sea ice models is best accomplished with satellite datasets. Observing sea ice concentration and areal extent from satellites is a well established practice (Liu et al., 2016; Meier et al., 2017; Markus and Cavalieri, 2000; Markus and Cavalieri, 2009; Comiso, 2009; Lavergne et al., 2019). There are methods based on data in the visual, infrared and microwave wavelength bands and climate data records produced from these

methods are commonly cited as polar climate indicators (Stroeve et al., 2012; Screen and Simmonds, 2010; Liu et al., 2009). While sea ice concentration is more readily observed, sea ice thickness provides a more complete characterization of the state of the climate system because it allows for calculation of sea ice volume and latent heat release. Recent literature has made clear that reliable long-term observations of basin wide sea ice thickness are needed in order to constrain the representations of sea ice in global climate models (Mayer et al., 2019). Sea ice thickness based observations of sea ice volume can be used along with other observations to refine the large range of historical and projected sea ice area and volume across coupled global climate models (Docquier and Koenigk, 2021). Indeed, the lack of reliable long term sea ice thickness observation constraints is the primary barrier to reducing the uncertainty in future sea ice area and volume projections (Massonnet et al., 2018).

Sea ice thickness derived from space-based altimetry data collected by satellites like CryoSat-2 and ICESat-2 stand as the current state of the art (Connor et al., 2009; Kwok and Cunningham, 2008; Markus et al., 2017, Wingham et al., 2006; Laxon et al., 2013). However, their low spatial coverage and orbit characteristics make for incomplete and infrequent sampling across the Arctic basin while uncertainties in snow depth and ice density lead to high uncertainties in sea ice thickness estimations from these instruments (Wang et al., 2016). A method of combining data from CryoSat-2 and ICESat-2 has been shown to alleviate some of these concerns (Kwok et al., 2020). Additional satellite based methods include estimating the thickness of thin sea ice using low-frequency passive microwave satellite data (Tian-Kunze et al., 2014) and combining low frequency passive microwave data with altimetry data in

order to take advantage their complementing data and spatial coverage (Ricker et al., 2017b; Zhou et al., 2018; Shi et al., 2020). Other strategies for retrieving sea ice thickness include a one-dimensional surface energy balance model driven by satellite products (Key et al., 2016) and correlating sea ice thickness with sea ice age (Liu et al., 2020). The various available products are discussed and compared against one another both qualitatively and quantitatively in Wang et al. (2016) and against upward looking sonar (ULS) in Sallila et al. (2019). While these observation techniques are able to produce estimates of sea ice thickness, none are able to differentiate between the effects of sea ice dynamics and sea ice thermodynamics.

Sea ice models account separately for both thermodynamic and dynamic processes in order to determine ice thickness and predict how it will respond in a changing climate (Thorndike et al., 1975; Zhang and Rothrock, 2001; Hibler, 1980). These models are evaluated against sea ice thickness observations (Boe et al., 2009; Massonnet et al., 2012; Shu et al., 2020;) but current state of the art, Arctic basin-wide observations capture only overall ice thickness (Markus et al., 2017; Laxon et al., 2013) and are unable to distinguish between thermodynamic and dynamic processes, which are independently affected through different mechanisms in a changing climate. In order to properly predict how sea ice will respond in a changing climate, these independent processes must be individually evaluated within models, requiring independent observations of each.

In this work, I address the issue of a lack of large scale observations of thermodynamic and dynamic sea ice thickness processes and their comparison to models. In Chapter 2, I introduce the data sources that are used throughout the work. This includes various

observational datasets and model outputs. In Chapter 3, I present a novel thermodynamic sea ice thickness growth rate satellite retrieval. This novel retrieval methodology is what enables the development of a wintertime climatology of sea ice thickness thermodynamic growth and dynamic effects, presented in Chapter 4. Finally, Chapter 5 begins to compare the results shown in Chapter 4 to the output from three global climate model simulations and a sea ice model reanalysis product. This work is only the beginning of an exciting line of inquiry, along which there is still much more to be done.

Chapter 2

Data

The retrieval method and climatology development described here utilizes passive microwave brightness temperatures, a passive microwave based sea ice concentration dataset, motion vectors and a satellite based thickness dataset. A preliminary validation of the retrieval method references sea ice thickness from ice mass balance buoy data, satellite and airborne altimeter based sea ice thickness data, and sea ice models. Global climate model output data is used for comparison with the climatology.

2.1 Passive microwave brightness temperatures and sea ice concentration

The Advanced Microwave Scanning Radiometer (AMSR)-Earth Observing System (-E), aboard National Aeronautics and Space Administration's (NASA) Aqua satellite and AMSR2,

aboard Japan Aerospace Exploration Agency's (JAXA) Global Change Observation Mission - W1 (GCOM-W1) satellite brightness temperatures available from the National Snow and Ice Data Center (NSIDC) were used in this study (Cavalieri et al., 2014; Markus et al., 2018). The AMSR-E data is available from June 2002 through October 2011 and the AMSR2 data is available from July 2012 to the present. The AMSR2 data has been intercalibrated with the AMSR-E data and the brightness temperatures between these two instruments are treated here as a continuous dataset (Markus et al., 2018). The data is provided on a 25 km polar stereographic grid, but when needed on a basin-wide scale for use with the sea ice thickness retrieval method described here, the data were linearly interpolated to a 25 km Equal-Area Scalable Earth (EASE)-Grid 2.0.

The NASA Team 2 algorithm is a passive microwave brightness temperature sea ice concentration algorithm (Markus and Cavalieri, 2000). It is an enhancement to the original NASA Team algorithm (Cavalieri et al., 1984; Gloersen and Cavalieri, 1986) in that it adds 85 GHz frequency brightness temperatures to the original algorithm, which used only 19 GHz and 37 GHz data, in order to better account for interference from surface effects. The algorithm utilizes open ocean and 100% ice concentration tie points in polarization and spectral gradient ratios to determine sea ice concentration. While originally developed for use with Special Sensor for Microwave Imager (SSM/I) data (Markus and Cavalieri, 2000), the algorithm was planned to be and is now in use with AMSR-E and AMSR2 data. Here we use this AMSR-E and AMSR2 sea ice concentration data, which is available from the NSIDC as a part of the same dataset that contains the brightness temperatures used to calculate snow–ice interface

temperature (Cavalieri et al., 2014; Markus et al., 2018).

2.2   Sea ice motion vectors

Sea ice is not static, but rather a dynamic collection of variably sized parcels that are each in constant horizontal motion under the effects of wind, ocean currents and internal stress. In order to treat sea ice in a Lagrangian sense, the motion of these parcels must be understood. Here we use the Polar Pathfinder Daily 25 km EASE-Grid Sea Ice Motion Vectors, Version 4 available from the NSIDC (Tschudi et al., 2019; Tschudi et al., 2020). The product is available from 1978 to present at daily and weekly temporal resolution, each with basin-wide coverage and each on the 25 km EASE-Grid. Using an optimal interpolation scheme, ice motion vectors are created from cross correlated satellite brightness temperature data from AMSR-E, Advanced Very High Resolution Radiometer (AVHRR), Scanning Multichannel Microwave Radiometer (SMMR), SSM/I and Special Sensor Microwave Imager/Sounder (SS-MIS), along with International Arctic Buoy Program (IABP) buoy locations and a National Centers for Environmental Protection (NCEP)/National Center for Atmospheric Research (NCAR) wind reanalysis data derived free drift estimate. Each satellite and buoy dataset are included in the optimal estimation scheme only when available within the life span of the ice motion product. This means input data sources vary throughout the record. DeRepentigny et al. (2016) found the weekly sea ice motion vectors to have a 7% median error when compared against IABP buoys between 1988 and 2011.

2.3   Airborne and satellite based sea ice thickness products

CryoSat-2 carries the SAR/Interferometric Radar Altimeter-2 (SIRAL-2) instrument (Wingham et al., 2006; Laxon et al., 2013) and was launched by the European Space Agency (ESA) in 2010. Similar to other satellite altimeters, ice thickness is determined from CryoSat-2 data by first calculating the thickness of the sea ice above sea level—known as the freeboard— by determining the distance traveled by the radar signal between the satellite and the ice surface and subtracting that distance from the satellite orbit altitude above sea level. A climatological snow loading provides a correction for the reduced propagation speed of the radar signal through snow. Then, the assumed snow loading and a hydrostatic balance is used to determine sea ice mass which in turn is converted to thickness using an assumed density (Laxon et al., 2013). Gridded ice thickness products derived from ESA CryoSat-2 Level 1b data are provided by numerous sources (Tilling et al., 2018; Kurtz et al., 2014a; Ricker et al., 2014; Hendricks and Ricker, 2020; Ricker et al., 2017a; Kwok and Cunningham, 2015; Hendricks et al., 2018; Guerreiro et al., 2017). The primary differences between these datasets relate to averaging period, grid sizing and radar response waveform retracking procedure.

The ESA Soil Moisture and Ocean Salinity (SMOS) satellite carries the Microwave Imaging Radiometer using Aperture Synthesis (MIRAS) instrument which measures 1.4 GHz passive microwave brightness temperatures at 35 to 50+ km resolution (Mecklenburg et al., 2012).

While originally intended for measuring soil moisture and ocean salinity, the high penetration depth of the 1.4 GHz channel into sea ice allows for retrieval of an ice temperature that when incorporated into a radiative transfer model yields a sea ice thickness estimate (Tian-Kunze et al., 2014). This approach has associated uncertainties in sea ice below 0.5 m thick that are lower than those of satellite altimeters.

Sea ice thickness observations from SMOS and CryoSat-2 have complementing uncertainties. SMOS has high uncertainties when measuring thick ice and CryoSat-2 has high uncertainties when measuring thin ice (Ricker et al., 2017b). This creates an opportunity for synergy between the instruments. The AWI CryoSat-2/SMOS combination product (CS2SMOS) dataset takes advantage of this synergy. By combining the datasets through a weighted averaging scheme, root mean squared errors (RMSEs) are reduced from 76 cm with CryoSat-2 alone to 66 cm and the squared correlation coefficient is increased from 0.47 with CryoSat-2 to 0.61 when compared against NASA Operation Ice Bridge (OIB) data (Ricker et al., 2017b). The AWI CS2SMOS dataset is available at a weekly time resolution and on a 25 km EASE-Grid 2.0 and was used with the method demonstrated here due to the high spatial coverage.

The NASA OIB mission is an airborne campaign comprising a series of flights covering the years 2009-2020, bridging the gap between the NASA Ice, Cloud and land Elevation Satellite (ICESat) and NASA ICESat-2 laser altimeter satellite missions (Kurtz et al., 2013). Among the instruments aboard each OIB flight, of primary importance to this study are the Airborne Topographic Mapper (ATM) instrument (Krabill et al., 1995) and snow radar (Panzer et al.,

2013). The ATM is a laser altimeter whose return signal is used along with an aerial photography based sea ice lead (fracture) discrimination algorithm to retrieve sea ice total freeboard height—i.e., freeboard plus snow depth—at 40 m spatial resolution. The snow radar return signal is used to determine snow depth. Sea ice freeboard and snow depth are used in conjunction with a hydrostatic balance to determine sea ice thickness at the sea ice freeboard resolution of 40 m. We use OIB sea ice thickness from the IceBridge L4 Sea Ice Freeboard, Snow Depth, and Thickness, Version 1 and its Quick Look counterpart as provided by the NSIDC (Kurtz et al., 2015; Kurtz et al., 2016). The data from 2014-2019, covering all of the data used here except those from 2013, are only available in the Quick Look format and may have increased uncertainties due to a roughly 5 cm underestimation of snow depths by the snow radar waveform retracking method applied in this version (Kwok et al., 2017). The Quick Look product fits the snow radar response waveform to a model simulated waveform in order to determine snow depth while the standard product merely identifies the depth of the first peak waveform response above a designated threshold. Figure 2.1 shows OIB flight paths used in this study.

2.4   Ice mass balance buoys

In order to statistically characterize the sea ice thickness retrieval method described herein, ice mass balance buoy (IMB) data served as the reference. The IMBs were deployed and maintained by the United States Army Corps of Engineers Cold Regions Research and Engineering Laboratory (CRREL) (Perovich et al., 2021). Undeformed ice floes are chosen

for buoy sites to ensure the buoy data is representative of the surrounding ice (Polashenski et al., 2011).

Data fields used from the buoys were sea ice thickness and geolocation in latitude and longitude. Ice thickness is observed using two acoustic rangefinder sounders, one positioned above and one positioned below the ice. Winter sea ice growth is derived from the under–ice sounder. Each sounder has an accuracy of 0.005 m (Richter-Menge et al., 2006). An Argos antenna mounted on the buoy transmits the geolocation and other observations at minimum twice per day (Richter-Menge et al., 2006). For this study, all data fields were resampled to 1 d resolution by calculating daily mean values. All buoys from the years 2003 to 2016 showing an entire season of sea ice thickness growth were used for comparison with the exception of buoys installed in landfast ice and those that show obvious ice deformation effects, which often damage the instrument and lead to the end of data acquisition. As such, sea ice thickness growth observed by the buoys is assumed to be caused strictly by thermodynamic processes. Table 2.1 provides details pertaining to the buoys used. Buoy 2013F spanned two winter seasons and as such has been divided into two buoy numbers, 2013F and 2013Fb, with 2013Fb covering the second winter season during which the buoy was deployed. As such, a deployment date is not listed for 2013Fb. Drift tracks from 1 November to 1 April for the buoys are shown in Fig. 2.1, showing that the buoys are concentrated in the Central Arctic and Beaufort Sea.

Efforts to compare satellite based records of sea ice thickness with ground truth are hampered by the spatial scale mismatch between satellite and ground observations. Ground truth
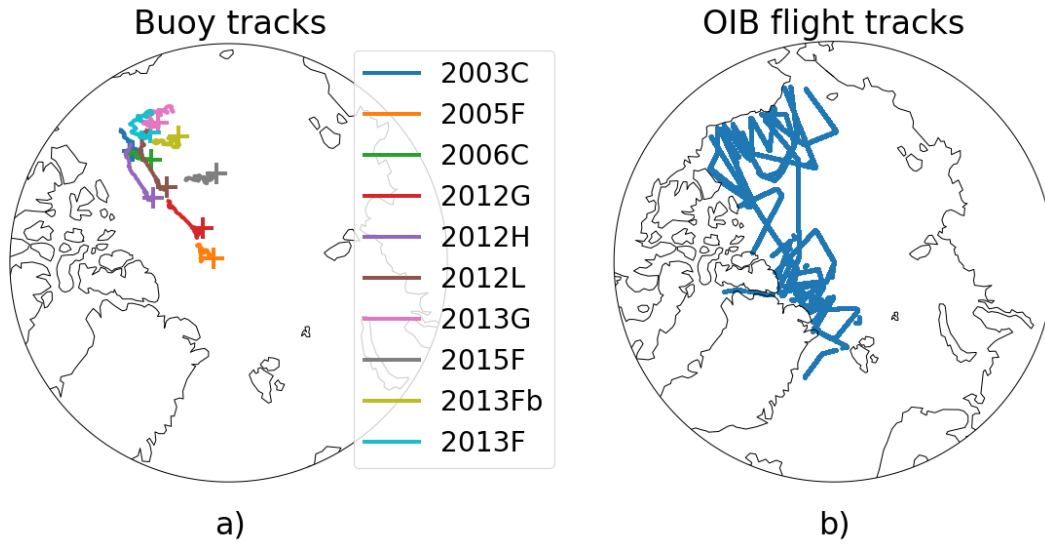
FIGURE 2.1: Tracks traveled by a) ice mass balance buoys and b) Operation IceBridge flights used in this study. Initial buoy location is signified with a plus symbol and all buoy tracks are from 1 November to 1 April.

TABLE 2.1: A listing of United States Army Corps of Engineers Cold Regions Research and Engineering Laboratory (CRREL) Ice Mass Balance buoys used in this work. All buoys from 2003 to 2016 containing a full season of sea ice thickness growth are included, excluding those in landfast ice or showing obvious dynamic effects.

Buoy	Region	Ice Type	Deployment date	Final Acquisition Date
2003C	Beaufort Sea	Multi-year	2002/8/31	2004/7/12
2005F	Central Arctic	Multi-year	2005/9/3	2007/3/22
2006C	Beaufort Sea	Multi-year	2006/9/4	2009/8/22
2012G	Central Arctic	First year	2012/10/1	2015/5/20
2012H	Beaufort Sea	First year	2012/9/10	2014/1/16
2012L	Beaufort Sea	Multi-year	2012/8/27	2013/9/25
2013F	Beaufort Sea	Multi-year	2013/8/25	-
2013Fb	Beaufort Sea	Multi-year	-	2015/8/27
2013G	Beaufort Sea	Multi-year	2013/9/4	2014/5/5
2015F	Central Arctic	Multi-year	2015/8/13	2016/8/2

measurements of sea ice are typically taken from a single point while satellites observe sea ice thickness on the scale of kilometers. The variability of sea ice conditions across those kilometers leads to uncertainty in the comparison. It has been shown, however, that while

variability in absolute ice thickness may be significant on the spatial scale of a satellite observation, sea ice growth and melt are relatively uniform on the satellite length scale (Polashenski et al., 2011). Therefore, while absolute comparisons of sea ice thickness between a ground truth and satellite observation may be tenuous, comparisons of growth over a winter season between single point ground truth and satellite based observations are more robust.

2.5 Sea ice models

The Pan-Arctic Ice–Ocean Modeling and Assimilation System (PIOMAS) is a numerical model reanalysis product that couples the Parallel Ocean Program (POP) model developed at Los Alamos National Laboratory with a thickness and enthalpy distribution (TED) model (Zhang and Rothrock, 2003). The TED model includes a viscous–plastic sea ice rheology (Hibler, 1979) and a sea ice thickness distribution scheme that accounts for redistribution due to ridging (Thorndike et al., 1975). The model utilizes a generalized orthogonal curvilinear coordinate (GOCC) grid. The northern grid pole is shifted to be over Greenland where there is no ocean or sea ice, avoiding the need to deal with converging meridians and grid cell areas that approach zero. This shift also allows the highest grid resolutions to occur in the Canadian Archipelago, Baffin Bay and the Greenland Sea where the geography is intricate. Mean grid resolution over the oceans is roughly $1°$ and less than this over the Arctic. The model is driven by daily surface forcing and sea surface temperatures (SSTs) provided by a NCEP/NCAR reanalysis and NSIDC sea ice concentration in order to produce daily Arctic sea ice thickness distributions from 1978 to present (Schweiger et al., 2011). Here we use

the daily effective sea ice thickness output which converts sea ice thickness distribution into a single effective thickness value for each grid cell.

Additionally, the data output from the sea ice model described in Kang et al. (2021), henceforth K21, was used to provide additional context. K21 nudged a one-dimensional sea ice thermodynamic model with satellite retrieved snow–ice interface temperatures. The model itself is based on Maykut and Untersteiner (1971) and is a multi-layer numerical approximation for the snow and sea ice system. While the model is driven by European Centre for Medium-Range Weather Forecasts (ECMWF) ERA-Interim reanalysis data, temperatures at the snow–ice interface are nudged using the snow–ice interface temperature retrieval described by Lee and Sohn (2015) in a non-physical correction term. This method was extrapolated to basin-wide results on the 25 km EASE-Grid 2.0 by Lagrangian tracking of individual sea ice parcels. The retrieval methodology described here in Chapter 3 is similar but greatly simplified and driven directly by the snow–ice interface temperature retrieval.

2.6   Global climate models

The NCAR Community Earth System Model Version 1 (CESM1) and Version 2 (CESM2) are open source, fully coupled Earth system models consisting of biogeochemistry, atmosphere, land, ocean, and sea ice components (Hurrell et al., 2013; Danabasoglu et al., 2020). They were created in order to facilitate research into how the Earth system works and are commonly used as tools to predict how a changing climate will affect various aspects of the

Earth system (Moore et al., 2013; Wolf and Toon, 2015; Lehner et al., 2017; Alexander et al., 2018; Ford et al., 2018; Muntjewerf et al., 2020; Dalaiden et al., 2020).

A single climate model simulation represents one outcome of a multitude of potential naturally occurring possibilities given the forcing in question. As such, it is difficult to distinguish errors in the model results from the internal climate variability inherent to the Earth system with only a single model simulation result. In order to address this, a model forcing is often repeated some number of times with only slight, round-off level differences between model initial conditions in order to more fully illustrate the range of possible realizations given by the system's inherent internal variability. This concept was initially applied to numerical weather model forecasting (Lorenz, 1963) and is now applied to climate modelling in the form of model ensembles. Here we utilize the CESM1-Large Ensemble (CESM1-LE) (Kay et al., 2015) and the CESM2-LE (Rodgers et al., 2021).

2.6.1 CESM1 Large Ensemble

CESM1 is a World Climate Research Programme (WCRP) Community Model Intercomparison Project Phase 5 (CMIP5) (Taylor et al., 2012) era model available with a number of different configurations consisting of various combinations of Earth system model components and forcings scenarios as defined by the CMIP5 protocols (Hurrell et al., 2013). The CESM1 model was identified as one of the most reliable of the CMIP5 class models based on a normalized distance from observations metric for temperature and precipitation (Knutti et al., 2013). Most relevant to the present study is the sea ice model component, the Los Alamos National Laboratory (LANL) Community Ice Code (CICE) Version 4 (CICE4) sea

ice model (Hunke and Lipscomb, 2010). CICE 4 includes the thermodynamics described by Bitz and Lipscomb (1999) that conserves brine pocket energy storage into the melt season and the dynamic component described by Hunke and Dukowicz (2002) which incorporates an elastic-viscous-plastic sea ice rheology into curvilinear coordinates. The CICE 4 model uses the same POP model derived, 1° nominal, Greenland Pole, GOCC grid that is used in PIOMAS. The ice thickness distribution within each grid cell is accounted for using the scheme described by Thorndike et al. (1975) and is discretized into four thickness categories. The fundamental equation solved by the CICE model is found in Thorndike et al. (1975) and is very similar to Equation 3.1 and 4.1. The ocean model underlying the sea ice model in CESM1 is the Parallel Ocean Program, version 2 (POP2; Smith et al., 2010).

The CESM1-LE is a collection of 40 model realizations for the years 1920 to 2100, all using the same model configuration and forcing (Kay et al., 2015). The model configuration is the CESM1 model with the Community Atmosphere Model version 5 (CESM1(CAM5); Hurrell et al., 2013) and the external forcing is a combination of historical forcing from 1920 to 2005 (Lamarque et al., 2010) and representative concentration pathway 8.5 (RCP8.5) forcing from 2005 to 2100 (Meinshausen et al., 2011). Round-off level differences in the initial air temperature field across the ensemble members produce the ensemble range which replicates the internal variation that the experiment was designed to capture. Output data for the CESM1-LE was accessed through the NCAR Climate Data Gateway via the CESM Large Ensemble Community Project website (`https://www.cesm.ucar.edu/projects/community-projects/LENS/`, last access: 6 October 2022).

2.6.2 CESM2 Large Ensemble

The latest version of the NCAR coupled Earth system model is CESM2 which is a WCRP CMIP Phase 6 (Eyring et al., 2016) class model (Danabasoglu et al., 2020). The new model offers a series of improvements to the atmosphere, ocean, land, land ice, river transport and coupler components of the model. Additionally, CESM2 utilizes an updated sea ice model component in CICE Version 5.1.2 (CICE5; Hunke et al., 2015). The CICE5 model includes a parameterization of multi-phase thermodynamics as described by Turner and Hunke (2015). The parameterization seeks to replicate the phenomenon described by Feltham et al. (2006) and discussed in Section 3.2.2.3 whereby local temperature and salinity change the thermodynamic properties of the sea ice due to it being a two-phase, saline, porous medium. The model also includes an updated melt pond parameterization (Hunke et al., 2013) and a salinity dependent freezing temperature. Once again, the CICE 5.1.2 model uses the same $1°$ nominal, GOCC grid that is found in both PIOMAS and CICE 4 (CESM1). Finally, the model vertical resolution has been increased to eight sea ice layers whereas CESM1 and CICE4 included only four layers. CESM2 includes the same POP2 ocean model as CESM1 (Smith et al., 2010) but includes several improvements per Danabasoglu et al. (2012).

As the name implies, CESM2-LE is an update to CESM1-LE using the CESM2 model (Rodgers et al., 2021). In contrast to the 40 members of CESM1-LE, CESM2-LE includes 100 ensemble members and includes the updated Community Atmosphere Model version (CAM6) (Danabasoglu et al., 2020). The model forcing is also updated. Half of the 100 members are forced by the historical and future Shared Socioeconomic Pathway (SSP) 3-7.0

as outlined by the CMIP6 protocol (Eyring et al., 2016), while the remaining half are forced by the same forcing but with biomass burning emissions smoothed by an 11-year running mean due to highly time-variable emissions during the 1990-2020 period caused by the inclusion of certain observations. A key difference between CESM1-LE and CESM2-LE lies in the initialization scheme. Whereas CESM1-LE used only round-off level differences across ensemble members, CESM2-LE includes differing Atlantic Meridional Overturning Circulation (AMOC) states, in what is termed macro-ensembles, in addition to the round-off level differences, which are termed micro-ensembles. While the memory of these differences between the macro-ensemble members does expire in time, it does not do so until the year 1960. As such, any variation in results between the macro-ensemble members during the time period of this analysis can be considered due to internal variability. The Northern Hemisphere ocean and sea ice data from the CESM2-LE is on the same Greenland Pole grid as CESM1-LE and was accessed via the CESM2 Large Ensemble Community Project website (`https://www.cesm.ucar.edu/projects/community-projects/LENS2/`, last access: 13 October 2022).

2.6.3 Forced ocean sea ice

In order to isolate the ocean and sea ice components of the CESM2 model, an additional simulation called the Forced Ocean Sea Ice (FOSI) was utilized. The ocean and sea ice only model run served as the NCAR contribution to phase 2 of the Ocean Model Intercomparison Project (OMIP-2) which was endorsed as part of CMIP6 (Tsujino et al., 2020; Eyring et al., 2016). The model consists of the POP2 ocean component and CICE5 sea ice component

and is forced by an adapted version of the Japanese 55-year atmospheric reanalysis product (JRA-55; Kobayashi et al., 2015) that was purpose-built for driving ocean-sea ice models and is called JRA55-driving ocean (JRA55-do; Tsujino et al., 2018). For this reason, the results of the FOSI CESM2 simulation are expected to more closely mimic observed conditions during the historical period than the large ensemble datasets. The single FOSI simulation covers 61 years covering the years 1958 to 2018 and is spun up by repeating the 61 year forcing cycle five times prior to the sixth cycle, which serves as the analysis period. The output variables from the FOSI simulation are on the same nominal 1° Greenland Pole grid as the sea ice outputs from CESM1 and CESM2. Data from this simulation was accessed via the Earth System Grid Federation (`https://esgf.llnl.gov/index.html`, last access: 10 October 2022).

Chapter 3

A simple model for daily basin-wide thermodynamic sea ice thickness growth retrieval

3.1 Background

Simple models have been used in the past to investigate various aspects of the sea ice systems. Semtner (1976) proposed a 0-layer model driven by snow–ice interface temperature designed to reduce the computational expense of more complex numerical modelling schemes like that of Maykut and Untersteiner (1971) for use with global climate scale modelling. The model performs similar the the Maykut and Untersteiner (1971) model and a 3-layer model also proposed in Semtner (1976), albeit with a slightly skewed seasonal cycle. The 0-layer model

is similar to SLICE in that it defines the sea ice vertical temperature profile and growth rate using a singular temperature at the snow–ice interface. Thorndike (1992) introduced the concept of a "toy" model which uses simplified physics to investigate the fundamental physical relationships within the sea ice system. Bjork and Soderkvist (2002) used a slightly more sophisticated "toy" model to investigate the effects of poleward energy flux on sea ice thickness. Eisenman and Wettlaufer (2009) and Eisenman (2012) utilized a simple single column model predicated on tracking an internal energy quantity in order to determine whether certain non-linear threshold sea ice behaviors predicted to occur in a changing climate have any basis in the fundamental physics of the system.

Recent efforts to retrieve temperature at the boundary between snow and sea ice, referred to as the snow–ice interface temperature, have opened a new door in polar climate observation (Kilic et al., 2019; Lee and Sohn, 2015; Lee et al., 2018). These methods take advantage of radiances from AMSR, AMSR2, SSM/I and SSMIS passive microwave instruments using channels whose wavelengths carry information from the snow–ice interface. Kang et al. (2021) demonstrated the utility of these snow–ice interface temperature data by using them to nudge a sea ice model, improving the model's results. By coupling this newly available snow–ice interface temperature data with Stefan's Law governing the thermodynamics of sea ice growth (Stefan, 1891; Lepparanta, 1993), I introduce a new method of retrieving thermodynamic sea ice thickness growth called Stefan's Law Integrated Conducted Energy (SLICE).

As sea ice accretes on the underside of the ice layer, the latent heat of fusion conducts up

through the ice to the snow–ice interface. In Stefan's Law, that conducted heat and therefore

rate of accretion is calculated using a heat conduction equation with the snow–ice interface

temperature as the upper boundary condition and the local freezing temperature of sea

water set as the lower boundary condition (Stefan, 1891; Lepparanta, 1993). By inserting

the satellite retrieved snow–ice interface temperature into this relationship, SLICE retrieves

daily rates of ice accretion and model sea ice thickness on a basin-wide scale during the sea

ice growth season by integrating these retrieved growth rates from an initial sea ice thickness

condition.

3.2 Methodology

Sea ice grows thicker through two primary physical mechanisms: thermodynamic phase

change and dynamic changes due to the relative motion of the ice pack. The governing

equation for an Eulerian sea ice thickness field can be written as

$$\frac{\partial H}{\partial t} = f(t, H, \mathbf{x}) - \nabla \cdot (\mathbf{u}H) , \tag{3.1}$$

where H is plane slab sea ice thickness; t is time; f is a function of time, thickness and

position vector $\mathbf{x}$ describing thermodynamic sea ice thickness increase; and $\mathbf{u}$ is the ice

motion vector and is itself a function of time and position. This equation is analogous to

Eq. (3) in Thorndike et al. (1975), but does not include the redistribution term because

here a plane slab thickness H was used rather than a thickness distribution. The second

term on the right hand side of Eq. (3.1) captures dynamic thickness changes, including both

advection and deformation of sea ice. Through the following methodology called Stefan's Law Integrated Conducted Energy (SLICE), the first term on the right hand side of Eq. (3.1) is retrieved and a parcel tracking approach approximates the sea ice advection component of the second term on the right in order to model basin-wide thickness.

3.2.1 Snow–ice interface temperature

In order to retrieve snow–ice interface temperature from passive microwave brightness temperatures, a multi-linear regression algorithm described by Kilic et al. (2019) was used. The algorithm was developed on the premise that low frequency passive microwave brightness temperatures are well correlated with snow–ice interface temperature as demonstrated using a radiative transfer model by Tonboe et al. (2011).

The algorithm first determines an estimated snow depth with an algorithm developed using multi-linear regression of ground truth snow depth to AMSR2 passive microwave brightness temperatures in vertical polarization at 6.9 GHz, 18.7 GHz, and 36.5 GHz (6V, 18V, and 36V). The ground truth snow depth training dataset is taken from the 2012G, 2012H, 2012J, and 2012L CRREL IMBs. Another multi-linear regression was performed between ground truth snow–ice interface temperature from the same CRREL IMBs, the estimated snow depth and AMSR2 passive microwave brightness temperatures from the 6.9 GHz vertical polarization channel, which was found to have the highest correlation to the buoy snow–ice

interface temperature. The resulting algorithm for T_{si} in K is as follows:

$$D_s = 1.7701 + 0.0175T_{B,6V} - 0.0280T_{B,18V} + 0.0041T_{B,36V} \tag{3.2}$$

$$T_{si} = 1.086T_{B,6V} + 3.98log(D_s) - 10.70\,, \tag{3.3}$$

where D_s is snow depth in m and $T_{B,6V}$, $T_{B,18V}$, and $T_{B,36V}$ are the observed 6V, 18V and 36V channel brightness temperatures in K, respectively. When evaluated against a set of IMBs consisting of 2013F, 2013G, 2014F and 2014I, the regression shows an RMSE of 2.9 K.
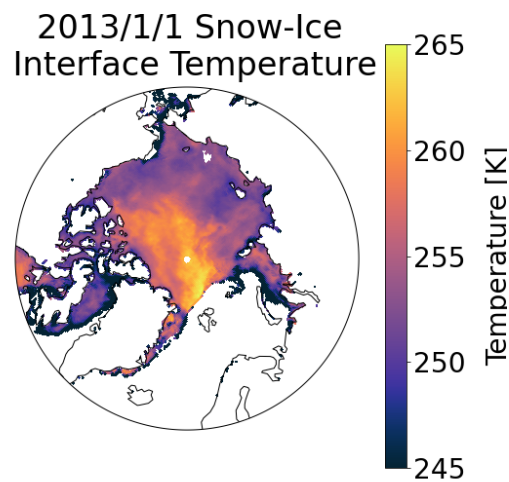
FIGURE 3.1: Snow–ice interface temperatures on 1 January 2013 derived from AMSR2 radiances.

Liquid water at the emitting layer in the form of open ocean or melt ponds interferes with the snow–ice interface temperature algorithm. As such, the snow–ice interface is only calculated here in grid cells with greater than 95% sea ice concentration. While the algorithm was developed for use with AMSR2, it was applied to brightness temperatures from both AMSR2

and AMSR-E using the continuous and intercalibrated dataset provided by NSIDC (Markus et al., 2018). Figure 3.1 shows snow-ice interface temperatures on January 1, 2013 derived from AMSR2 data.

3.2.2 Thermodynamic sea ice thickness growth

A simple model of one-dimensional thermodynamic sea ice thickness growth is a balance of heat fluxes where phase change is occurring, i.e., at the interface between the solid sea ice and liquid sea. These heat fluxes are latent heat released during the phase change of liquid sea water to solid sea ice, F_l; basal sensible heat flux from the liquid sea to the solid ice, F_w; and heat conducted through the ice and away from the phase change interface, F_c. These three fluxes are balanced at the phase change interface as follows:

$$F_l + F_w = F_c. \tag{3.4}$$

When the snow–ice interface temperature drops below the temperature at the bottom of the ice, heat provided by basal sensible flux and the latent heat of freezing is pulled to the snow–ice interface. In the method described here, a satellite observation of snow–ice interface temperature (Kilic et al., 2019) drives this energy balance in order to determine sea ice thickness growth.

3.2.2.1 Stefan's Law

By balancing the conductive heat equation with a latent heat of freezing and basal sensible heat flux term, Stefan's Law relates the rate of thermodynamic sea ice thickness increase to the temperature difference between the snow–ice interface and bottom of the ice layer, the latter of which is at or very near to the freezing temperature of sea ice (Stefan, 1891; Lepparanta, 1993).

Conduction is the transfer of heat across a solid medium and is always accompanied by a temperature difference across that medium. The equation governing one-dimensional, steady state conduction through sea ice is

$$F_c = \frac{\kappa_{eff}}{H} \left(T_f - T_{si} \right) , \tag{3.5}$$

where κ_{eff} is the thermal conductivity of sea ice, H is sea ice thickness, T_f is the freezing point of sea water and T_{si} is the snow–ice interface temperature.

A change in the phase of a material must either release or accept energy as the molecular bonds and motion within the material change. In the case of a phase change from liquid to solid, energy is released as the molecular motion is reduced with the introduction of molecular bonds. The equation describing the one-dimensional, latent heat release as sea

water changes phase from liquid to solid is:

$$F_l = \rho_i L \frac{dH}{dt} \,, \tag{3.6}$$

where ρ_i is the density of the solid phase of the material, L is the latent heat of fusion and $\frac{\partial H}{\partial t}$ is the change in sea ice thickness per unit time.

In Stefan's Law, Eqs. (3.5) and (3.6) are substituted into Eq. (3.4) to form

$$\rho_i L \frac{\partial H}{\partial t} = \frac{\kappa_{eff}}{H} (T_f - T_{si}) - F_w \,. \tag{3.7}$$

Isolating for sea ice thermodynamic growth rate,

$$\frac{\partial H}{\partial t} = \frac{\kappa_{eff}}{\rho_i L H} (T_f - T_{si}) - \frac{F_w}{\rho_i L} \,. \tag{3.8}$$

Equation (3.8) defines the thermodynamic growth function, f, found in Eq. (3.1) and is equivalent to Eq. (3.1) when dynamic growth is neglected. There are three assumptions inherent to this relationship (Lepparanta, 1993). First, heat conduction in the horizontal direction is assumed to be negligible. Second, it is assumed that there is no thermal inertia present in the ice. This means that the local derivative of temperature with respect to sea ice depth is constant throughout the sea ice layer—i.e., the temperature profile is linear—and the system is in equilibrium. The spatial derivative of temperature found in a typical heat equation reduces to the temperature difference between the snow–ice interface temperature

and the freezing point of water due to these first two assumptions. Third, it is assumed that there is no internal heat source, such as the absorption of short wave radiation. The second and third assumptions are only valid during polar winter and times of the year when solar incidence angles are very shallow.

Eqs. (3.7) and (3.8) can be integrated to give:

$$H = \sqrt{H_0^2 + \delta t \frac{2\kappa_{eff}}{\rho_i L}(T_f - T_{si})} - \delta t \frac{F_w}{\rho_i L}, \tag{3.9}$$

where H_0 is the initial sea ice thickness. The time interval δt chosen for the results shown herein is one day based on the daily availability of snow–ice interface temperature and both snow–ice interface temperature and basal sensible flux are assumed to be constant during each day.

At each time step, SLICE determines sea ice thickness by solving Eq. (3.9) for H given an H_0 using the snow–ice interface temperature calculated at the nearest AMSR-E or AMSR2 grid cell. The change in sea ice thickness at each time step is dependent on initial sea ice thickness. This necessitates SLICE be applied in a Lagrangian sense as the sea ice thickness must be tracked and stored in order to accurately calculate the change at the next time step. In Eq. (3.8), thicker sea ice grows slower than thinner sea ice with a given snow–ice interface temperature. This means that in the presence of only thermodynamic effects, a SLICE sea ice thickness profile that is biased relative to ground truth will correct towards the unbiased SLICE thickness profile. This relationship replicates the phenomenon described in Bitz and

Roe (2004), whereby thick ice recovers from climate related perturbations slower than thin ice and has experienced greater thinning on a decadal time scale.

3.2.2.2   Basal heat flux

Observation of basal sensible heat flux from liquid sea water to solid sea ice is inherently difficult. Typically, basal sensible heat flux is calculated as a residual of other more readily observed quantities in the heat budget of a one-dimensional sea ice profile, typically from a drifting station or buoy. Using this methodology, McPhee and Untersteiner (1982) observed March through May basal sensible heat fluxes of less than 2 W m^{-2} using data from the FRAM I drift station in the Arctic Ocean, Perovich and Elder (2002) report oceanic sensible heat flux values of just a few W m^{-2} from November to May during the Surface HEat Budget of the Arctic Ocean (SHEBA) field experiment and Lei et al. (2014) examined Chinese National Arctic Research Expedition (CHINARE) buoy data to discover relatively high basal sensible heat fluxes of greater than 10 W m^{-2} through December that gradually decreased to near 0 by mid-February.

Maykut and Untersteiner (1971) completed a sensitivity analysis using their thermodynamic sea ice model, investigating the equilibrium mean annual sea ice thickness corresponding to basal sensible heat flux values ranging from 0 to 8 W m^{-2}. Realistic mean annual sea ice thickness resulted when basal sensible heat flux was set between 1.3 W m^{-2} and 2.6 W m^{-2}. They chose a constant basal sensible heat flux value of 2 W m^{-2} for their model based on this analysis and available observational data. The coupled ocean–sea ice model PIOMAS

supplies oceanic sensible heat fluxes to the sea ice model component as modeled by the ocean model component. Zhang and Rothrock (2003) show these modeled ocean sensible heat fluxes in most of the Arctic basin to be near 2 W m^{-2}. K21 also employed a constant basal sensible heat flux of 2 W m^{-2}.

In keeping with these studies, a constant basal sensible heat flux $F_w = 2$ W m^{-2} was applied in the SLICE methodology. The effect of basal sensible heat flux on thermodynamic sea ice growth is independent of thickness and can be easily quantified as the last term of Eq. (3.9). For a given snow—ice interface temperature, the reduction of sea ice thickness growth by inclusion of a basal sensible flux is linearly related to the flux value by a factor of $1/\rho_i L$. With a density of 917 kg m^{-2} and a latent heat of fusion of 3.32 x 10^5 J kg^{-1}, each 1 W m^{-2} of basal sensible heat flux from the liquid sea water to solid sea ice decreases sea ice thickness growth by 2.84×10^{-4} m d^{-1}. Removal of the 2 W m^{-2} basal sensible heat flux would increase sea ice growth by 5.67×10^{-4} m d^{-1} and an increase from 2 W m^{-2} to 10 W m^{-2} would decrease thermodynamic sea ice thickness growth by 2.27×10^{-3} m d^{-1}. This corresponds to a 0.0857 m increase and a 0.343 m decrease, respectively, when summed from 1 November to 1 April.

3.2.2.3 Multi-phase properties of sea ice

Sea ice is best described not as a homogeneous solid medium but rather as a heterogeneous, multi-phase material including solid ice and pockets of liquid brine whose size and salinity change with varying ice temperatures. In turn, these brine pocket changes significantly affect

the bulk thermodynamic properties of the ice layer (Feltham et al., 2006). Equation (3.9) includes effective thermal conductivity, κ_{eff}, a property that is subject to this effect. As such, the parameterization of effective conductivity described in Feltham et al. (2006) was adopted.

First, a constant ocean salinity, S, of 33 ppt is assumed. Next, it is assumed that the ice is in thermal equilibrium relative to phase change between liquid brine and solid ice and calculate freezing point temperature (in °C), T_f, as a function of salinity (in ppt) per Notz (2005):

$$T_f(S) = -0.0592S - 9.37 \times 10^{-6}S^2 - 5.33 \times 10^{-7}S^3. \tag{3.10}$$

The latent heat of fusion for liquid to solid phase change is defined as the difference between the enthalpies of the two states. In this case, a latent heat of fusion (in J kg^{-1}), L, as calculated as a function of temperature (in °C) by Notz (2005) is used:

$$L(T_f) = 333700 + 762.7T_f - 7.929T_f^2. \tag{3.11}$$

Next, Eq. (15) from Feltham et al. (2006) defines the effective thermal conductivity (in W m^{-1} K^{-1}) as function of sea ice temperature, T_i and sea ice salinity, S_i:

$$\kappa_{eff} = \kappa_{bi} - (\kappa_{bi} - \kappa_b)\frac{(T_f(0) - T_f(S_i))}{(T_f(0) - T_i)}, \tag{3.12}$$

where κ_{bi} is the thermal conductivity of bubbly ice and κ_b is the thermal conductivity of liquid brine and are defined per Schwerdtfeger (1963), Batrak et al. (2018) and Bailey et al.

(2010) (all in W m^{-1} K^{-1}):

$$\kappa_{bi} = \kappa_i(2\kappa_i + \kappa_a - 2V_a(\kappa_i - \kappa_a))/(2\kappa_i + \kappa_a + V_a(\kappa_i - \kappa_a)) \tag{3.13}$$

$$\kappa_b = 1.162(0.45 - 1.08 \times 10^{-2}T + 5.04 \times 10^{-5}T^2) \tag{3.14}$$

$$\kappa_i = 1.162(1.905 - 8.66 \times 10^{-3}T + 2.97 \times 10^{-5}T^2) \tag{3.15}$$

$$\kappa_a = 0.03 \tag{3.16}$$

$$V_a = 0.025 \, , \tag{3.17}$$

where κ_i is the thermal conductivity of pure ice, κ_a is the thermal conductivity of air and V_a is the fractional volume of air in the sea ice. Effective conductivity calculated with surface conditions was used for SLICE which is similar to the approach adopted by Cox and Weeks (1988) who also used conductivity calculated from the surface to determine conductive flux through the ice layer.

A first-year sea ice (FYI) density of 917 kg m^{-3} and multi-year sea ice (MYI) density of 882 kg m^{-3} was reported by Alexandrov et al. (2010) and these values have seen use in the sea ice thickness calculations from CryoSat-2 data (Laxon et al., 2013; Tilling et al., 2018; Hendricks and Ricker, 2020; Kwok and Cunningham, 2015). A sea ice density of 915 kg m^{-3} is also in use with altimeter data (Kurtz et al., 2014b; Petty et al., 2020) and a sea ice density of 925 kg m^{-3} has been used with IceSat data (Kwok and Rothrock, 2009). Choice of sea ice density is a significant source of uncertainty in altimeter-based estimates of sea ice thickness. Kurtz et al. (2014b) report that the range of densities from 882 kg m^{-3} to 925 kg

m^{-3} yields a 1.1 m range in sea ice thickness estimates from a 60 cm snow—ice freeboard with 35 cm of snow. The SLICE system of equations uses a FYI sea ice density of 917 kg m^{-3}. For a given snow—ice interface temperature, basal sensible heat flux and sea ice thickness, a change to 915 kg m^{-3} would increase sea ice thickness growth rate by at most only 0.2% and a change to 925 kg m^{-3} would decrease sea ice thickness growth by at most only 0.8%.

3.2.3   Parcel tracking of advection

The divergence term on the right hand side of Eq. (3.1) represents sea ice dynamics and includes the effects of both advection and deformation on local sea ice thickness. Advection moves sea ice parcels horizontally and deformation redistributes sea ice volume vertically through ridging or lead formation.

The advection effects contained within the divergence term can be approximated using a parcel tracking approach, allowing for the modelling of basin-wide results. This parcel tracking methodology is initialized with the CS2SMOS data from the first week of November and each 25 km x 25 km grid cell is divided into 5 km x 5 km parcels, which are advected daily throughout the winter using the Polar Pathfinder motion vectors interpolated to their position. This parcel tracking methodology is similar to the Sea Ice Tracking Utility (SITU, http://icemotion.labs.nsidc.org/SITU/) described by DeRepentigny et al. (2016). Each parcel adds sea ice thickness thermodynamically using the SLICE thermodynamic model. At any given time step, the parcels can be gridded to the EASE-Grid 2.0 by taking the mean thickness of parcels within each grid cell. This approach leaves out deformation effects.

While taking the sum of all parcel volume within each grid cell and dividing by grid cell area would be a more physically sound methodology for this regridding, the results from such a method proved unrealistic. Figure A.1 found in the Appendix shows a comparison between the chosen method using grid cell mean and the method using grid cell sum. New parcels are initiated at any grid cell not containing a sea ice parcel but showing 95% or greater sea ice concentration. New ice parcels are initialized at a thickness of 0.05 m. Any parcel that is located in a region with less than 95% sea ice concentration at any time step is removed. The result is a daily gridded Arctic basin-wide sea ice thickness dataset representing thermodynamic sea ice growth in the 95% sea ice concentration ice pack.

3.3   Results

The SLICE sea ice thickness retrieval methodology can be applied on a single one-dimensional, vertical profile basis or across a large area. Here, results comparing one-dimensional SLICE data to ice mass balance buoy thicknesses and Arctic basin-wide results to OIB and AWI CS2SMOS data are presented.

3.3.1   Ice mass balance buoy comparison

The SLICE retrieval method results were compared to data from ice mass balance buoys. First, the SLICE results and buoy data were compared from an instantaneous perspective. The input snow–ice interface temperature retrieval results were compared to buoy snow–ice interface temperature in Fig. 3.2a. The snow–ice interface temperature retrieval shows a
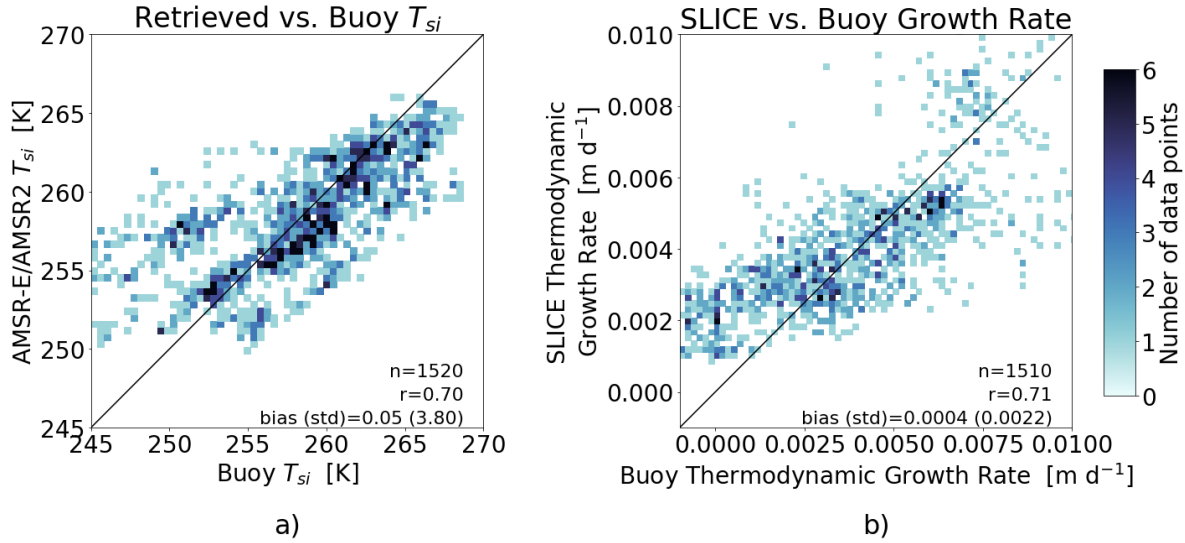
FIGURE 3.2: An instantaneous comparison of (a) AMSR-E/AMSR2 retrieved snow–ice interface temperature to buoy snow–ice interface temperature and (b) SLICE retrieved thermodynamic growth rate using buoy thickness to buoy thermodynamic growth rate. Linear correlations are 0.70 and 0.71, respectively.

mean bias of 0.05 K with a standard deviation of 3.80 K. The linear correlation value between retrieved snow–ice interface temperature and buoy snow–ice interface temperature is 0.70. This analysis does include the 2012G, 2012H, and 2012L buoys that were also included in the training dataset used in creation of the multilinear regression snow–ice interface temperature retrieval algorithm, because the intention is not to validate this retrieval, rather to investigate sources of error in the SLICE results. Figure 3.2b shows daily instantaneous SLICE thermodynamic growth rate retrieved via Eq. 3.8 using buoy thickness versus buoy provided daily thermodynamic growth rate. Because the CRREL IMB thickness data is provided to only the hundredths of a meter and daily variations in thickness are typically much small than this, a 14 day rolling average is applied to the buoy data. The linear correlation of this comparison is 0.71 and SLICE shows a mean bias of 4 x 10^{-4} md^{-1} with a standard deviation of 2.2 x 10^{-3} md^{-1}.
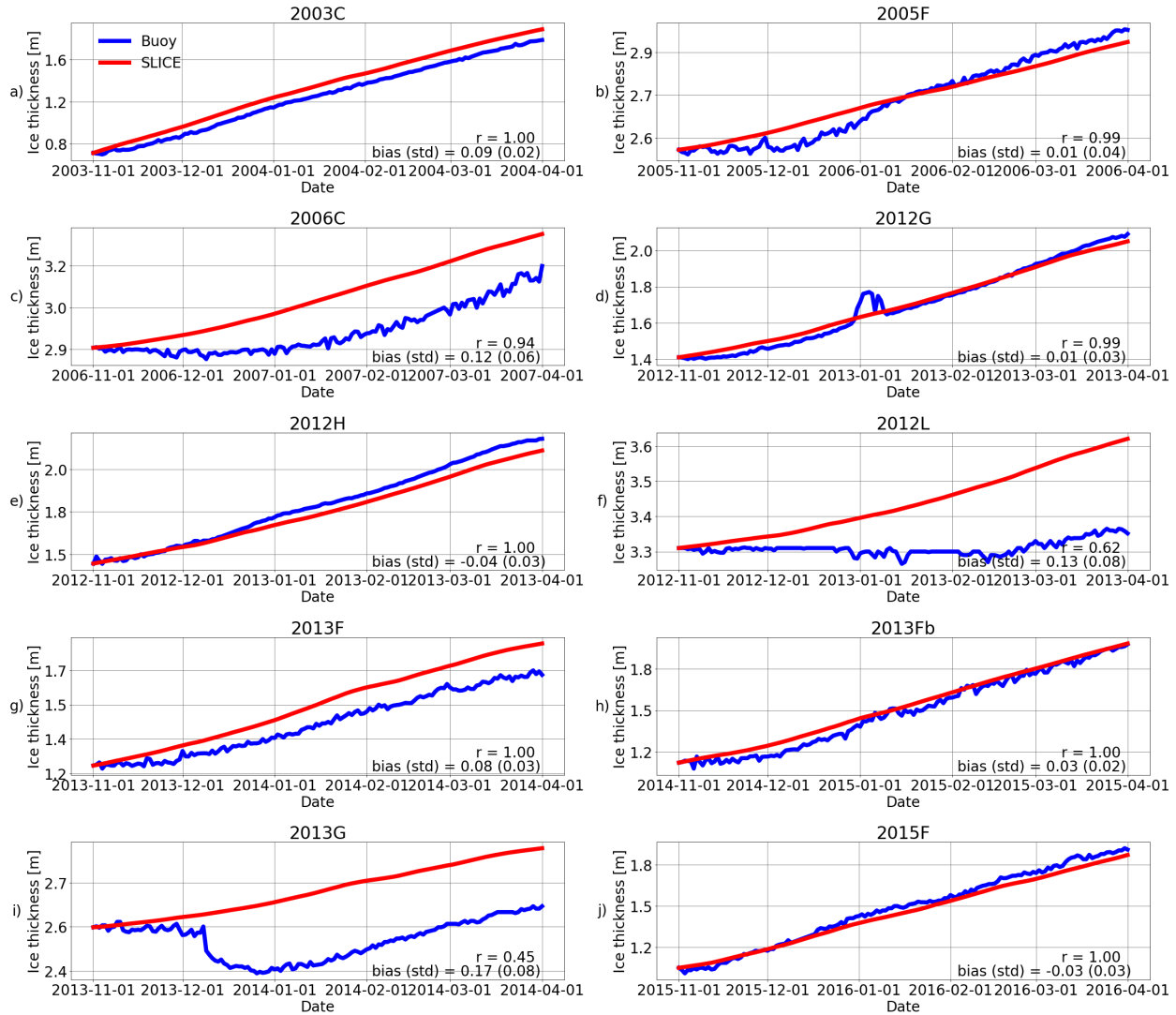
FIGURE 3.3: Ice thickness observations from ice mass balance buoys (blue) and SLICE (red) for buoys (a) 2003C, (b) 2005F, (c) 2006C, (d) 2012G, (e) 2012H, (f) 2012L, (g) 2013F, (h) 2013Fb, (i) 2013G and (j) 2015F. Linear correlation (r) and bias values are listed. Across all buoys, the r values have a mean of 0.89 and the biases have a mean of 0.06 m.

Next, SLICE was compared one-dimensionally to buoy data from a seasonal perspective. The retrieval method was initialized with the buoy observed sea ice thickness on 1 November and integrated through 1 April using Eq. 3.9. The results here are dependent only on the satellite based snow–ice interface temperature. The snow–ice interface temperature used on

a given day is taken from the nearest AMSR-E or AMSR2 grid cell to the buoy location. The resultant sea ice thickness time series are plotted with buoy sea ice thickness in Fig. 3.3. It is clear from Fig. 3.3 that the SLICE profiles agree well with the buoy sea ice thickness when initialized with an accurate initial ice thickness. The correlation coefficients ranges from 0.45 to 0.999 with a mean of 0.89 and standard deviation of 0.21 across all buoys. The bias, calculated by taking the mean over the entire profile length of the retrieval method result minus the buoy thickness, ranges from -0.04 m to 0.17 m with a mean of 0.06 m and standard deviation of 0.07 m across the buoys.

3.3.2   Arctic basin-wide comparisons
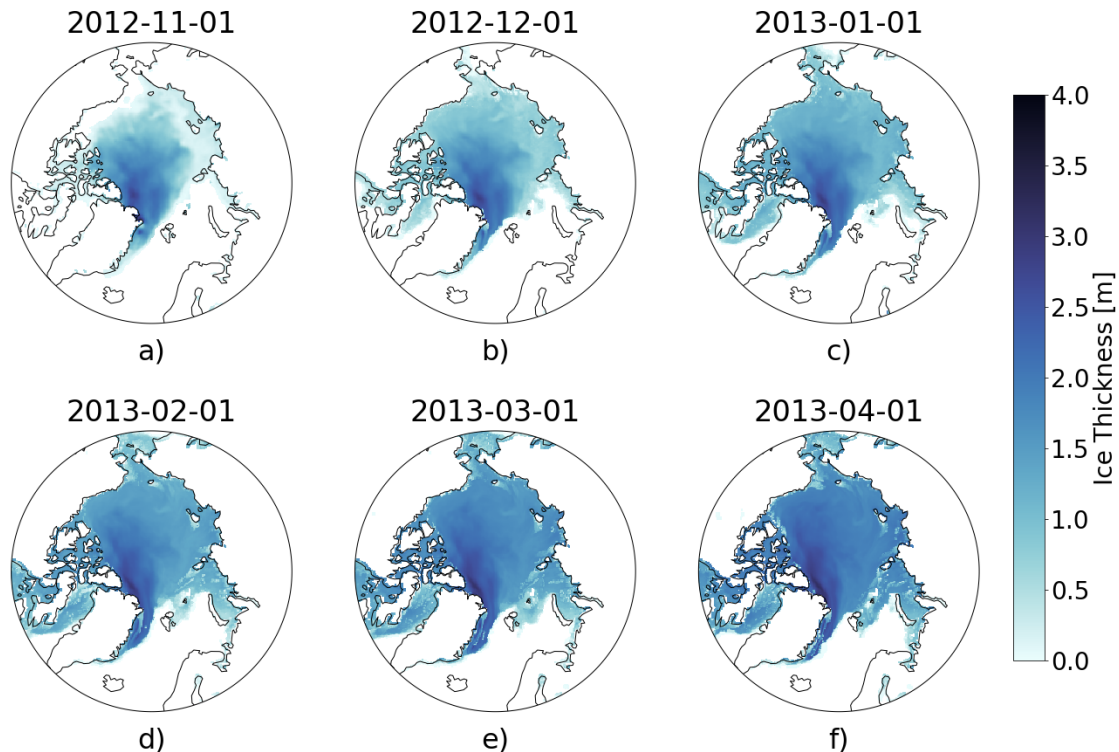
FIGURE 3.4: Sea ice thickness on a) 2 November 2012, b) 1 December 2012, c) 1 January 2013, d) 1 February 2012, d) 1 March 2013, e) 1 April 2013, f) 30 April 2013 created using SLICE with the 1 November 2012 AWI CS2SMOS as an initial state. The changes from month to month represent thermodynamic growth and advection.

Next, the SLICE retrieval method was utilized to model sea ice thickness on an Arctic basin-wide scale. Using the AWI CS2SMOS data for the first week of November as the initial state, the retrieval method was applied daily to the entire Arctic basin from 1 November to 1 April for the growth seasons beginning in 2012 through 2019. November 1 was chosen to ensure most ice was below the freezing point and there were limited melt ponds to interfere with the snow ice interface temperature observation. At each time step, the parcel tracking methodology described in Sect. 3.2.3 is applied. The 1 April results are regridded to the 25 km EASE-Grid 2.0 using the procedure also described in Sect. 3.2.3. Monthly basin-wide sea ice thickness plots for the sea ice growth season beginning in fall 2012 using AWI CS2SMOS as the initial state are shown in Fig. 3.4. The sea ice thickness data from SLICE is available daily but only the first of every month is plotted. The sea ice thickness is increasing and advection is relocating the volume horizontally throughout the Arctic basin.

To assess SLICE skill relative to PIOMAS and K21 data, all three datasets were compared with OIB sea ice thickness observations. OIB data from the month of March for the years 2013 through 2018 (including NSIDC OIB Quick Look data) was first binned by 25 km EASE-Grid 2.0 cell and averaged across each bin to create an OIB dataset collocated with SLICE. Both PIOMAS and the K21 data were also interpolated to the 25 km EASE 2.0 grid. A comparison between SLICE, PIOMAS and K21 is shown in Fig. 3.5. Linear correlation and bias statistics were calculated from this data. All three datasets show very similar linear correlations of 0.64, 0.67 and 0.68 for SLICE, PIOMAS and K21, respectively. The best mean bias is PIOMAS at 0.10 m, followed closely by SLICE at -0.12 and K21 at -0.24

m. The standard deviation of the bias is 0.70 for SLICE, 0.68 for PIOMAS and 0.69 for K21.
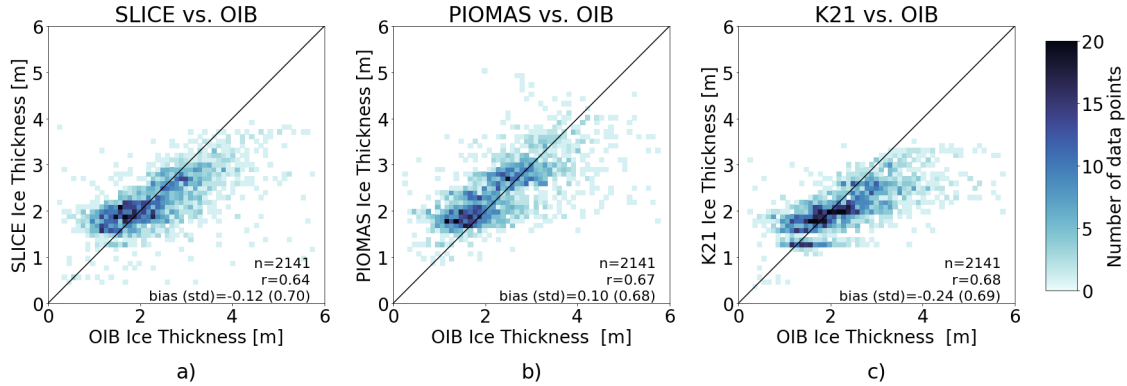
FIGURE 3.5: OIB thickness versus a) SLICE, b) PIOMAS and c) Kang et al., 2021 data including number of data points, linear correlations and bias (standard deviation). All three have similar linear correlations.

SLICE was also compared to PIOMAS using AWI CS2SMOS as the reference dataset. Figure 3.6 shows the differences in sea ice thickness between SLICE and AWI CS2SMOS and the differences between PIOMAS and AWI CS2SMOS on 1 April for the years 2013 through 2020. Figure A.2 in the Appendix shows plots of sea ice thickness used in this comparison from all three datasets. The differences are almost all between -1.5 m and 1.5 m and in most cases are near zero. The difference plots for SLICE and PIOMAS show similar patterns, though PIOMAS overestimates thickness in more areas than SLICE, which underestimates sea ice thickness in the central Arctic in almost all cases. The differences between SLICE and CS2SMOS are likely to be due to a lack of deformation effects. Figure 3.7 shows a scatter plot of AWI CS2SMOS sea ice thickness to sea ice thickness from SLICE and from PIOMAS. Both AWI CS2SMOS and SLICE are on a 25 km EASE-Grid 2.0 but in order to compare the AWI CS2SMOS data to PIOMAS, it is interpolated to each PIOMAS grid point. Linear

correlation and bias statistics were calculated from this data. SLICE and PIOMAS have similar linear correlations with AWI CS2SMOS of 0.76 and 0.77, respectively. SLICE shows a lower mean bias at 0.09 m compared to PIOMAS at 0.10 m. SLICE standard deviation of the difference is 0.63 m compared to 0.67 m for PIOMAS. Figure 3.8 shows total daily Arctic sea ice volume from SLICE, PIOMAS and AWI CS2SMOS during the winters from late 2012 to early 2020. The AWI CS2SMOS is taken from the the weekly data centered on each day. Both SLICE and PIOMAS follow the AWI CS2SMOS volume profile well. PIOMAS overestimates end of season volume in all years and underestimates initial volume in all cases except 2012-2013 and 2016-2017 leading to an overestimation of sea ice volume growth in all years. SLICE begins each season at the same volume as AWI CS2SMOS and ends all seasons closer than PIOMAS to the AWI CS2SMOS volume except 2014-2015 and 2015-2016. While there are not enough data points for a strong statistical comparison, SLICE is certainly a viable indicator of sea ice volume growth.

3.4   Discussion

SLICE uses a retrieval of snow–ice interface temperature (Kilic et al., 2019) to drive a very simple one-dimensional model of sea ice thermodynamics in order to retrieve thermodynamic sea ice thickness growth. By applying SLICE to individual parcels whose location throughout the Arctic basin is determined using a sea ice motion product (Tschudi et al., 2020), SLICE captures sea ice advection and produce basin-wide results. In doing so, SLICE functions similarly to much more intricate sea ice models such as PIOMAS (Zhang and Rothrock, 2003) and a sea ice model that is nudged with retrieved snow–ice interface temperature
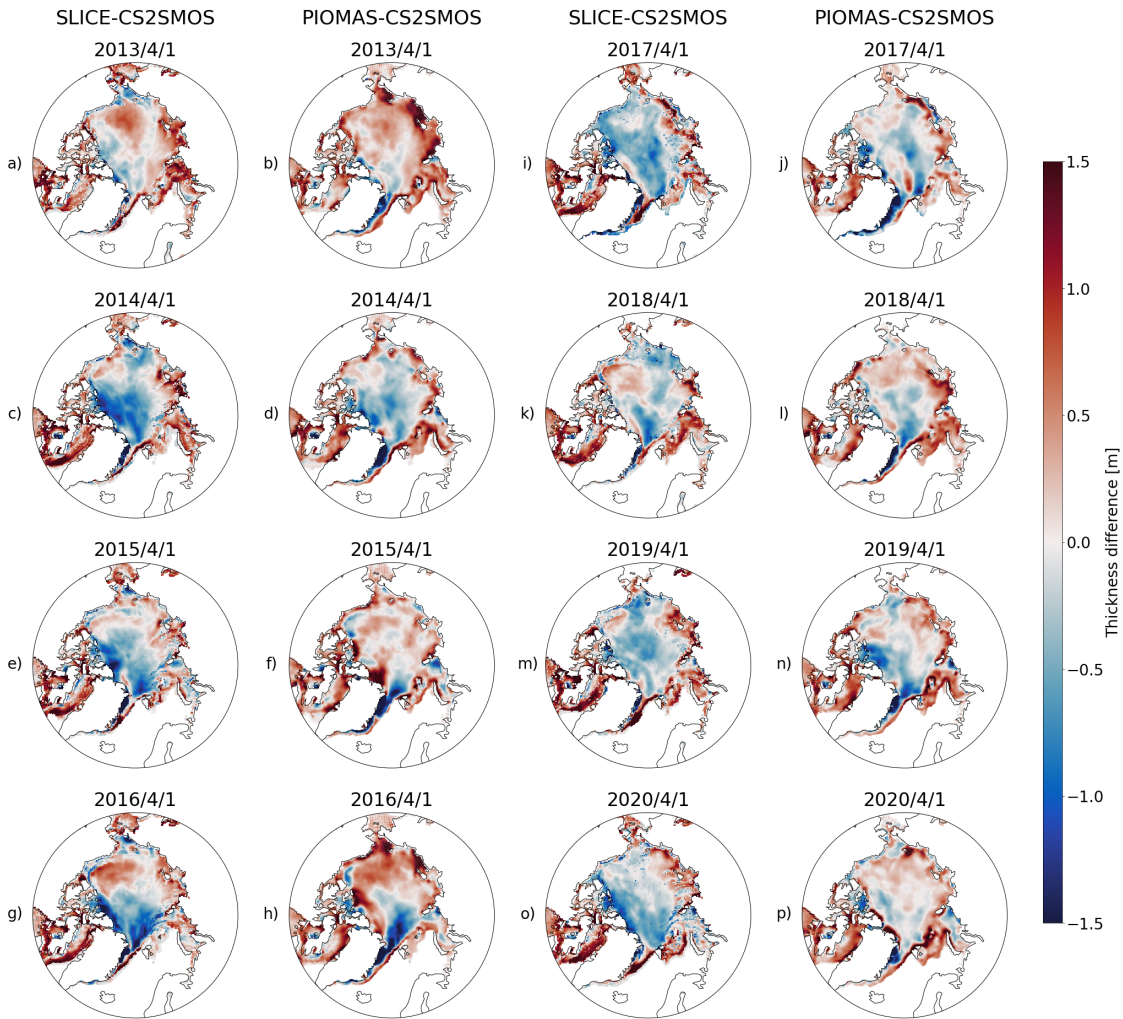
FIGURE 3.6: For the sea ice growth seasons ending in a–b) 2013, c–d) 2014, e–f) 2015, g–h) 2016, i–j) 2017, k–l) 2018, m–n) 2019 and o–p) 2020, a, c, e, g, i, k, m, o) SLICE sea ice thickness - AWI CS2SMOS sea ice thickness from 1 April and b, d, f, h, j, l, n, p) PIOMAS sea ice thickness - AWI CS2SMOS sea ice thickness from 1 April. The SLICE and PIOMAS differences show similarities in their overall pattern.

(Kang et al., 2021). While SLICE is capable of capturing thermodynamic sea ice growth and advection, it is unable to detect deformation effects—i.e., thickness changes due ridging or lead formation.

Figure 3.2 demonstrates SLICE's utility as a thermodynamic growth retrieval. The comparison between the input snow–ice interface retrieval and buoy snow–ice interface temperature
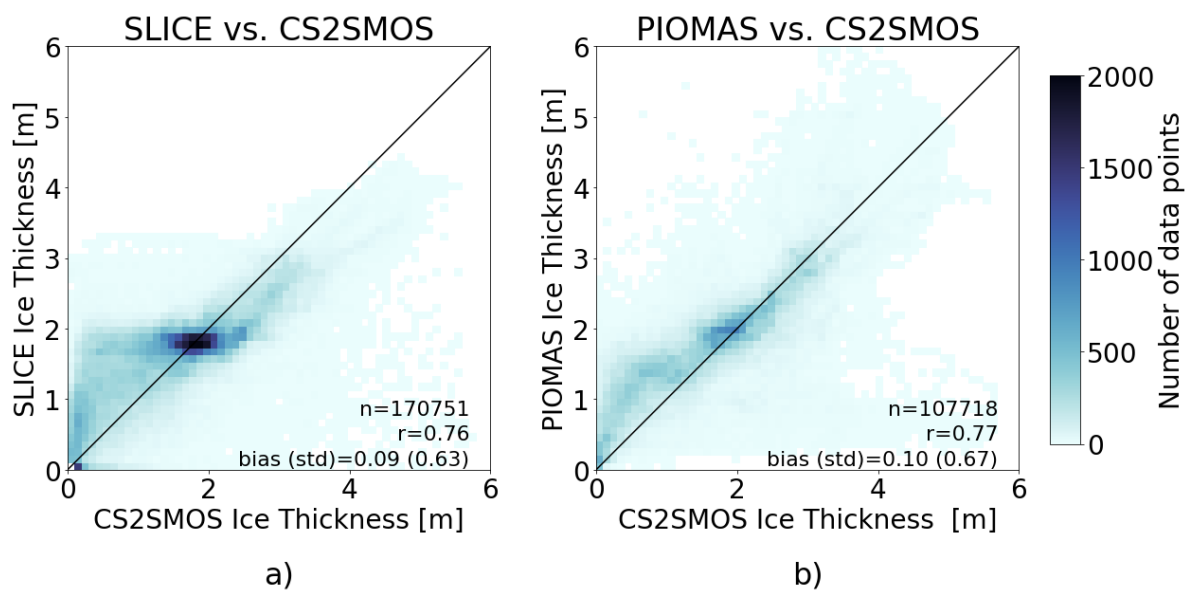
FIGURE 3.7: AWI CS2SMOS sea ice thickness versus a) SLICE sea ice thickness and b) PIOMAS sea ice thickness including number of data points, linear correlations and bias (standard deviation). SLICE and PIOMAS have nearly equal mean bias and linear correlation values.

shows that the retrieval is effective. The instantaneous SLICE thermodynamic growth rate calculated using buoy thickness shows a linear correlation of 0.71. The mean bias is 4 x 10^{-4} md^{-1} which is roughly 10% of the mean growth during the period. This bias is likely influenced by portions of the time series from buoys 2006C, 2012L and 2013G during which SLICE overestimates growth.

Figure 3.3 shows a comparison between ice mass balance buoy sea ice thickness measurements and the retrieval method initialized with the buoy data and integrated along an entire season for 10 buoys within the years 2003–2016. The mean correlation coefficient of 0.89 between the buoy measurements and the method is high. The bias values are also very encouraging with a mean of 0.06 m. Buoys 2006C, 2012L and 2013G show a SLICE profile that produces greater sea ice thickness than the buoys. There are likely two mechanisms causing this error.
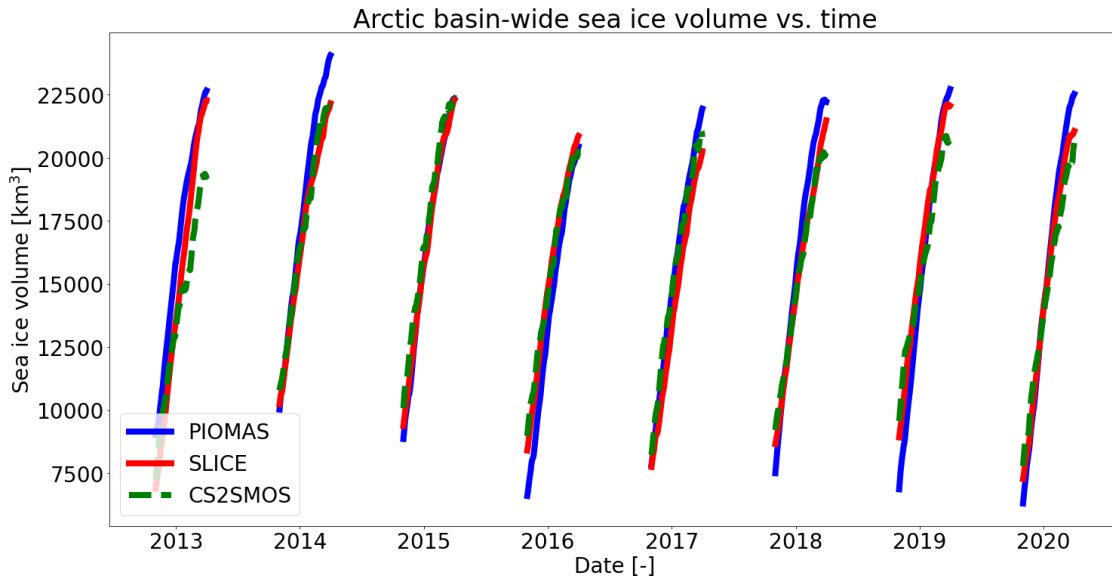
FIGURE 3.8: Wintertime sea ice volume versus time for SLICE, PIOMAS and AWI CS2SMOS.

For buoys 2006C and 2012L, the initial thicknesses are the two highest of the set and are near 3 m. In these cases, the cold atmospheric temperatures of the growth season have not yet reached the base of the ice, which must be below the freezing point in order for thickness to increase. In other words, the heat stored in the ice from summer has not yet escaped due to the higher thickness and greater heat storing capacity. This means the ice does not yet have a linear temperature profile with the sea ice base at the freezing point, a condition that SLICE assumes but is not met in reality by buoys 2006C and 2012L until after 1 November. In the case of 2013G, a melt event, which SLICE is unable to capture, occurs in December. Both of these phenomena cause SLICE to overestimate sea ice thickness. When sea ice is indeed increasing via thermodynamics, SLICE captures the growth well. Additionally, SLICE has a self-correcting quality by nature of Eq. (3.8) whereby sea ice thicknesses that are biased in either direction approach the unbiased SLICE sea ice thickness over time. These points

suggest the retrieval method is viable as a basis for modelling sea ice thickness but is highly dependent on an initial condition, as it calculates thermodynamic sea ice thickness increase rather than absolute thickness.

There are a number of assumptions inherent to Stefan's Law (Lepparanta, 1993) that must be considered in relation to SLICE as introduced in Sect. 3.2.2. In order to characterize conduction through the ice layer with only the snow–ice interface temperature and an assumed freezing point temperature at the bottom of the ice layer, it must be assumed that heat conduction in the horizontal is negligible and that the local vertical derivative of temperature throughout the ice layer is constant. These assumptions are reasonable. The remaining two assumptions are more salient. The first is that there is no internal heat source. This is untrue when there is significant short wave radiation absorbed within the sea ice. The final assumption is that heat exchange between the sea ice and the ocean is constant in space and time, which is likely to be invalid in some regions. Impacts of this assumption on the sea ice growth are investigated in Sect. 3.2.2.2.

Another source of uncertainty in SLICE ice thickness is the constraint that it is limited to areas with sea ice concentration greater than 95%. There is significant growth in areas where the sea ice concentration is low, such as the marginal ice zone (MIZ). This constraint would likely cause underestimated sea ice growth over those areas. Further validation of SLICE, particularly in regions other than the Beaufort Sea and Central Arctic, where all buoys and OIB flights used here were located and where the snow–ice interface temperature

retrieval multi-linear regression was performed, as well as investigation of the impacts of these assumptions and full characterization of uncertainties is warranted.

The Stefan's Law energy balance relationship and attendant assumptions amount to a simplification of the multi-layer thermodynamic model based on Maykut and Untersteiner (1971) that makes up the foundations of PIOMAS and K21. These assumptions remove the need for multiple layers. Additionally, whereas the thermodynamics in PIOMAS and K21 are driven by an atmospheric reanalysis product and nudged by snow–ice interface temperature in the case of K21, SLICE is driven by satellite observed snow–ice interface temperature and not reliant on an atmospheric reanalysis product. These factors allow for the retrieval of instantaneous thermodynamic thickness growth rate. Whereas PIOMAS models sea ice motion again using atmospheric reanalysis, SLICE uses a sea ice motion satellite product when used to model basin-wide sea ice thickness. This sea ice motion product and the snow–ice interface temperature product mean SLICE is heavily observationally constrained. The comparison between SLICE, PIOMAS and K21 shows that these assumptions and simplifications do not significantly degrade resultant sea ice thickness values when SLICE thermodynamic growth rate is used to model absolute thickness on a basin-wide scale. Indeed, thermodynamic growth rate calculated using average thickness over a 25 km x 25 km grid cell likely does not completely accurately describe thermodynamic growth rate over the entirety of that grid cell. Additionally, SLICE does not include the effects of deformation processes, which recently were shown to have contributed roughly 30% of total thickness growth during the Multidisciplinary drifting Observatory for the Study of Arctic Climate (MOSAiC; Nicolaus

et al., 2022) field campaign (von Albedyll et al., 2022; Koo et al., 2021).

Figure 3.8 is encouraging for the capability of SLICE to capture volumetric sea ice changes on a basin-wide scale. Per the model described by Eq. (3.1), sea ice volume is only added through thermodynamic processes—dynamic processes only serve to rearrange the volume already present. Though this statement does invoke the false assumption that dynamic processes do not change the density of the ice, it seems to be a factor in explaining the volumetric results. Though dynamic processes do not directly change sea ice volume within a given time step, their changing of the thickness of ice at a given location does impact thermodynamic processes at later time steps by virtue of f being a function of thickness, H, in Eq. (3.1). Inspection of Eq. (3.7) indeed shows that H impacts $\frac{\partial H}{\partial t}$. In regions where deformation increases sea ice thickness, SLICE will overestimate sea ice thickness increase and in regions where deformation decreases sea ice thickness, it will underestimate sea ice thickness increase. These phenomena, along with any phenomena inherent to either reference dataset, may explain volumetric differences between SLICE and the reference datasets. The 95% or greater criteria for SLICE may also contribute to differences, as the other datasets are not limited by this threshold.

3.5   Summary

New methods for observing snow–ice interface temperature (Kilic et al., 2019) have made possible a new strategy for observing thermodynamic sea ice thickness growth from space during the winter growth season: Stefan's Law Integrated Conducted Energy (SLICE). The

new strategy involves linking observed satellite retrieved snow–ice interface temperature with Stefan's Law (Stefan, 1891; Lepparanta, 1993). In the Stefan's Law relationship, latent heat of fusion is conducted from the bottom of the ice layer where new ice forms to the snow–ice interface and this rate of conduction and accretion is calculated using the snow–ice interface temperature and a parameterized freezing point temperature at the bottom of the ice layer. The snow–ice interface temperature retrieval algorithm used to drive the sea ice thickness growth equation uses passive microwave brightness temperatures from the AMSR-E and AMSR2 instruments (Kilic et al., 2019). Gridded brightness temperature data from these instruments are available at daily temporal resolution in the polar regions (Cavalieri et al., 2014; Markus et al., 2018), meaning modelled daily sea ice thickness growth is available basin-wide. Lee et al. (2018) provides a method for retrieving snow–ice interface temperatures using passive microwave brightness temperatures from the SSM/I and SSMIS instruments, allowing for the application of SLICE to sea ice growth seasons beginning in 1987. SLICE requires an initial sea ice thickness value is required and does not capture melting.

When compared from an instantaneous perspective, SLICE is an effective retrieval of thermodynamic growth rate with a bias of 4×10^{-4} m d^{-1} relative to an ice mass balance buoy dataset when buoy thickness is used a priori at each time step. When SLICE is initialized with the ice mass balance buoy thickness on 1 November and integrated for an entire growth season, the retrieval method compares well with the buoy observed sea ice thickness growth. Using ten buoys from 2003 to 2016, the mean linear correlation value is 0.89

and the mean bias is 0.06 m. SLICE can model basin-wide sea ice thickness by applying the thermodynamic growth retrieval to individual sea ice parcels and advecting the parcels across the basin using a sea ice motion product. This basin-wide methodology was applied to the winters between late 2012 and early 2020 using AWI CS2SMOS basin-wide sea ice thickness as the initial state. Results show that SLICE performs comparably to PIOMAS and K21, despite the assumptions and simplification that allow for the direct retrieval of instantaneous thermodynamic growth rate.

Current state of the art sea ice thickness observations from space, though capable of observing sea ice growth whether from thermodynamic or dynamic effects, are not capable of this spatial and temporal coverage. They also do not discriminate between dynamic and thermodynamic effects. For these reasons, a sea ice thickness dataset based on SLICE will be especially useful for investigating thermodynamic and dynamic sea ice phenomena that are small scale in space and time. SLICE need not be initialized at the beginning of the growth season and applied for an entire growth season but can be initialized at any time during the growth season and applied to any interval of time, allowing for use with case studies or other small time and space scale events. Additionally, the high temporal resolution retrieval of thermodynamic effects will allow for creation of useful datasets of surface energy flux from latent heat of fusion.

3.6 Code and data availability

Data used in creation of all figures within this chapter is available at `https://doi.org/10.5281/zenodo.6985505`. Code for creation of data and figures wihtin this chapter is available at `https://doi.org/10.5281/zenodo.7143799` and `https://github.com/janheuser/SLICE/releases/tag/3.0.0`. The following auxilliary datasets were used and are available at these locations: AMSR-E and AMSR2 brightness temperatures, `https://doi.org/10.5067/AMSR-E/AE_SI25.003` and `https://doi.org/10.5067/TRUIAL3WPAUP`; AMSR-E and AMSR2 SIC, `https://doi.org/10.5067/AMSR-E/AE_SI25.003` and `https://doi.org/10.5067/TRUIAL3WPAUP`; AWI CS2SMOS, `https://www.meereisportal.de`; sea ice motion vectors, `https://doi.org/10.5067/INAWUWO7QH7B`; OIB, `https://doi.org/10.5067/G519SHCKWQV6` and `https://doi.org/10.5067/GRIXZ91DE0L9`; CRREL IMB, `http://imb-crrel-dartmouth.org`; PIOMAS, `http://psc.apl.uw.edu/research/projects/arctic-sea-ice-volume-anomaly`; Kang et al., 2021, `https://doi.org/10.1029/2020MS002448`.

Chapter 4

A climatology of thermodynamic vs. dynamic Arctic wintertime sea ice thickness effects during the CryoSat-2 era

4.1   Background

Per Eqs. 1.1 and 3.1, total sea ice thickness changes are the sum of thermodynamic and dynamic changes. Large temporal and spatial scale observations of these processes, independent from one another, are lacking, however recent in-situ sea ice studies and satellite

scale observations of related processes like sea ice motion do offer a glimpse into the sign and magnitudes of these processes.

The Multidisciplinary drifting Observatory for the Study of Arctic Climate (MOSAiC; Nicolaus et al., 2022) presented an opportunity for partitioning thermodynamic and dynamic growth from a Lagrangian perspective along the Transpolar Drift over a full year from October 2019 to September 2020. von Albedyll et al. (2022) analyzed data from airborne electromagnetic (AEM) surveys and an ice mass balance buoy network to characterize the annual cycle of both dynamic and thermodynamic sea ice thickness contributions experienced by the ice pack surrounding the MOSAiC drift station. Thermodynamic growth was modeled using ice mass balance buoy temperature profiles and subtracted from overall ice growth captured by the airborne electromagnetic survey data in order to calculate dynamic sea ice effects as a residual. Overall, the dynamics contribution of 0.1 m out of the 1.1 m growth amounts to 10%. Offering a potential window into basin–wide partitioning of thermodynamics versus dynamics, Koo et al. (2021) NASA ICESat-2 data collected over the MOSAiC drift station to ice mass balance buoy thicknesses collected during the field experiment. They found that the mode of ICESat-2 derived sea ice thickness over this region represented level ice under the effects of thermodynamics only while mean and median sea ice thickness included sporadic deformation events which increased sea ice thickness under the effects of sea ice dynamics. Comparing the mean and median observations against the mode observations, the authors conclude that dynamics accounted for 35.6% of the mean sea ice thickness increase and 42.6% of the median sea ice thickness increase over a region

enclosed by a 50 km radius around the research vessel.

Other studies used estimates of sea ice drift vectors to relate dynamics to sea ice thickness growth, again from a Lagrangian perspective. Kwok and Cunningham (2016) calculated shear and divergence terms averaged over a region north of the Canadian Arctic Archipelago using estimated ice motion vectors during winter from 2011 through 2015. These terms and a constant thermodynamic growth term were linearly regressed to overall sea ice thickness change from ESA CryoSat-2. This analysis showed that divergence and shear led to 42% to 56% of overall thickness change averaged across the region in question during those winters, with the remaining change due to thermodynamic effects. The sea ice deformation effects of a 2015 winter storm in the Transpolar Drift north of Svalbard were examined by Itkin et al. (2018), who analyzed AEM measurements of freeboard before and after the storm during the Norwegian Young Sea ICE (N-ICE2015) expedition. By tracking individual features in the measured sea ice distribution, they were able to relate divergence and shear to changes in sea ice deformation. In multiplying the effects of this single storm by the climatological average of ten to twenty storms per winter, the authors predict 5% to 10% volume increases due to deformation in the region. von Albedyll et al. (2021) also took advantage of AEM freeboard measurements and satellite synthetic aperture radar observations of an unusually large polynya north of Greenland in 2018 to determine a relationship between deformation and thickness changes. Over the 65,000 km^2 polynya and over the 1 month of analysis, deformation of ice was found to account for an average of 50% of the thickness increase and in some cases as much as 90% of the thickness increase.

Kwok (2006) analyzed RADARSAT Geophysical Processor System (RGPS) sea ice motion vector derived Eulerian estimates of deformation from 1996 to 2000 over a much larger area than the aforementioned studies, though independent of any sea ice thickness measurements. They report that seasonal ice experiences more deformation than multi-year ice, possibly due to its decreased thickness and strength. They also report a decrease in sea ice divergence as the winter growth season progresses, potentially via the same mechanism of increasing thickness and strength. Even without a link to sea ice thickness, the findings of this study allow for the extrapolation of more localized, short term thickness effect results to a larger spatial scale.

While a number of localized and short term studies have yielded a partitioning of thermo-dynamic and dynamic growth, a large scale and longer term dataset is lacking—especially from a Eulerian perspective for easier comparison to model outputs. In this study, this knowledge gap is filled by presenting the first long-term, sub-seasonal temporal resolution, basin-wide and Eulerian estimation of dynamic effects on sea ice thickness, thermodynamic sea ice thickness growth, advection effect on sea ice thickness and deformation effect on sea ice thickness. A difficulty inherent to large scale partitioning of thermodynamic and dynamic effects has been large scale characterization of basal thermodynamic growth. The Stefan's Law Integrated Conducted Energy (SLICE) retrieval methodology, described in Chapter 3, allows for daily and basin–wide retrieval of wintertime thermodynamic sea ice growth rate using passive microwave brightness temperatures. Here, the retrieved thermodynamic growth rate is used in conjunction with overall sea ice thickness changes from the radar

altimeter aboard the ESA CryoSat-2 satellite (Laxon et al., 2013) to estimate dynamic sea

ice effects during the CryoSat-2 era beginning in 2010. With overall sea ice thickness growth

provided by a CryoSat-2 thickness product and thermodynamic growth provided by SLICE,

Arctic basin-wide sea ice thickness changes due to dynamics are calculated as the residual

difference between the two. The effects of advection are also estimated using a sea ice motion

vector dataset allowing for the calculation of deformation thickness as a residual of overall

dynamic thickness effects and advection thickness effects.

4.2   Methods

Sea ice thickness is affected by thermodynamic processes and dynamic processes. Thermo-

dynamic processes serve to change sea ice thickness through molecular phase change and

dynamic processes serve to change sea ice thickness through the mechanical processes of

advection and deformation (ridging or lead formation). An Eulerian governing equation for

sea ice thickness sums thermodynamic and dynamic processes:

$$\frac{\partial H}{\partial t} = f(t, H, \mathbf{x}) - \nabla \cdot (\mathbf{u}H) \,, \tag{4.1}$$

where H is plane slab sea ice thickness; t is time; f is a function of time, thickness and

position vector $\mathbf{x}$ describing thermodynamic sea ice thickness increase; and $\mathbf{u}$ is the ice

motion vector. The second term on the right hand side represents dynamic sea ice thickness

processes.

The aim is to partition basin-wide observations of overall changes to the sea ice thickness field, $\frac{\partial H}{\partial t}$, into component parts of thermodynamic growth, $f(t, H, \mathbf{x})$, and dynamic effects, $-\nabla \cdot (\mathbf{u}H)$. The result is basin-wide observations of thermodynamic and dynamic process effects on sea ice thickness. At each weekly time step, $\frac{\partial H}{\partial t}$ was calculated as the difference between the CS2SMOS sea ice thickness field from the current time step and that from the following time step. Dynamic effect, $-\nabla \cdot (\mathbf{u}H)$, was estimated as the difference between total growth, $\frac{\partial H}{\partial t}$, and expected thermodynamic growth, $f(t, H, \mathbf{x})$, retrieved using the SLICE methodology using the CS2SMOS sea ice thickness as the initial thickness.

The dynamics term within Eq. 4.1 can be further decomposed to form:

$$\nabla \cdot (\mathbf{u}H) = (\nabla H) \cdot \mathbf{u} + H(\nabla \cdot \mathbf{u}), \tag{4.2}$$

where the first term on the right now represents changes to local sea ice thickness due to advection, i.e., the movement of ice transporting ice of a new thickness into a grid cell, and the second term on the right represents sea ice thickness changes due to deformation processes caused by the divergence or convergence of the ice motion. Deformation effect does not include advection and therefore can be considered Lagrangian dynamics—i.e., the dynamic effect as observed by a Lagrangian drifter. Estimates of dynamic effects were further partitioned into advection effects and deformation effects using the sea ice motion vector product. At every time step, the first term on the right hand side of Eq. 4.2 is calculated using the spatial derivatives of the CS2SMOS ice thickness field calculated with central finite differencing and sea ice motion vectors and is taken to be advection effect. The

deformation effect is in turn taken to be the residual difference of the dynamic effect and this

advection effect. This approach was taken over calculating the deformation effect using the

motion vectors and advection effect as a residual because the motion vectors themselves were

found to be more reliable than the divergence of these motion vectors. As motion vectors

are not available within the Canadian Arctic Archipelago, advection effects and deformation

effect estimates are not available in this region either.

In summary, the governing equation expressed in Eq. 4.1 is conceptually reconstructed as

follows:

$$\frac{\partial(CS2SMOS)}{\partial t} = SLICE + dynamic\ effect\,, \tag{4.3}$$

and the dynamic effect is further decomposed into advection and deformation effects with

Eq. 4.2 conceptually reconstructed as follows:

$$dynamic\ effect = (\nabla CS2SMOS_i) \cdot ice\ motion\ vector\ + deformation\ effect. \tag{4.4}$$

The results shown here are weekly integrations of the terms within Eqs. 4.3 and 4.4. The

dataset covers 1 November through 1 April, due to SLICE assumptions described in Section

3 and availability of CS2SMOS data, spanning the ten winters beginning in the years 2010

and 2012-2020. The 2010 data begins on 15 November rather than 1 November along with

the availability of CryoSat-2 data and the winter beginning in 2011 is not included due to a

gap between availability of passive microwave data from the earlier AMSR-E and the latter

AMSR2. At each weekly time step, i, the following steps were completed at each point on

the 25 km EASE-Grid 2.0:

1. $\frac{\partial(CS2SMOS)}{\partial t}_i = CS2SMOS_{i+1} - CS2SMOS_i$

2. $thermodynamic\ growth = SLICE$

3. $dynamic\ effect = \frac{\partial(CS2SMOS)}{\partial t} - SLICE$

4. $advection\ effect = (\nabla CS2SMOS_i) \cdot ice\ motion\ vector$

5. $deformation\ effect = dynamic\ effect\ - advection\ effect$

4.3   Results

Figure 4.1 shows the wintertime mean dynamic effect, thermodynamic effect, advection effect and deformation effect on sea ice thickness across the entire 10 year analysis period. The magnitude and sign of these terms varies across the Northern Hemisphere sea ice. As expected, thermodynamic thickness growth is highest in the seasonal ice zones, often greater than 0.08 m d^{-1}, and inversely proportional to the climatological sea ice thickness, leading to less than 0.04 m wk^{-1} of thermodynamic growth in much of the Central Arctic. Dynamic effects increase sea ice thickness over 29% of the area exhibiting ice during the study period and decrease sea ice thickness over the remaining area. An increase in sea ice thickness due to dynamics occurs off the Siberian Coast in the Chukchi Sea where the Beaufort Gyre tends to deposit advected ice and similarly north of the Canadian Arctic Archipelago where both the Beaufort Gyre and Transpolar Drift tend to deposit advected ice. The highest

positive dynamic effect of greater than 0.04 m wk^{-1} are located just north of the central Canadian Arctic Archipelago. A decrease in sea ice thickness due to dynamics, often with magnitude greater than 0.08 m wk^{-1}, occurs in the coastal regions of the Kara and Laptev Seas from where the transpolar drift tends to remove ice, and similarly in the coastal regions of the Beaufort Sea due to a similar effect of the Beaufort Gyre. The negative advection effect dominates the Arctic sea ice, covering 66% of the study area. The exception primarily occurs where the Beaufort Gyre advects thick ice from north of the Canadian Arctic Archipelago to the Beaufort Sea. Here, advection effects greater than 0.04 m wk^{-1} are found. The most significant negative advection effects, less than 0.04 m wk^{-1}, occur in coastal Laptev Sea. Similar to advection effects, deformation effects are negative over most of the Arctic, covering 62% of the study area. The largest deformation effects of greater than 0.04 m wk^{-1} occur where the ice motion tends to deposit and form ice ridges, north of the central Canadian Arctic Archipelago, in the Chukchi Sea and north of Greenland. The Barents and Kara Seas are dominated by strong negative deformation effects, often times with magnitudes greater than 0.08 m wk^{-1}. Coupled with the positive advection effects in the Beaufort Sea are negative deformation effects in this region.

In the Fram Strait and Baffin Bay, dynamics serve to deposit ice on the east coast of Baffin Island and Greenland. Thermodynamic growth is high in Baffin Bay as ice is produced and exported by the prevailing ice drift. Advection in Baffin Bay clearly reduces thickness in the northern portions of the region as the current transports ice from the northern to the southern portion, where advection increases ice thickness. Deformation shows that some

ice is deposited and ridged on the east coast of Baffin Island. A very high advection effect is shown in the East Greenland Sea where ice export is substantial. Deformation effects are strongly negative here as the ice likely experiences lead formation throughout its export through the Fram Strait.
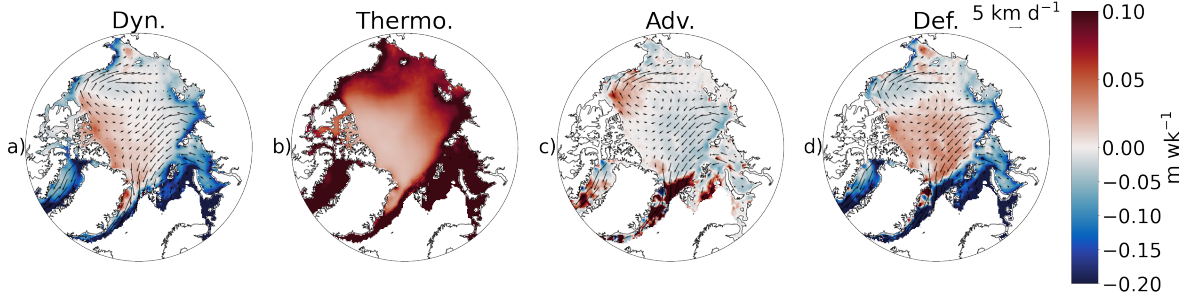
FIGURE 4.1: Wintertime mean from late 2010 through early 2021 (except the winter of 2011-2012) sea ice thickness changes due to a) dynamic effects, b) thermodynamic effects, c) advection effects and d) deformation effects. Mean sea ice motion vectors from the same period are also plotted with a), c) and d). The dynamic effect, advection and deformation follow spatial patterns evident in the ice motion vectors.

Uncertainty in the climatological mean is characterized using standard error of the mean and shown in Fig. 4.2. Standard error is calculated as the standard deviation of all dynamic effect measurements at a given grid cell divided by the square root of the number of data points at that grid cell:

$$\sigma_{\bar{E}} = \frac{\sigma_E}{\sqrt{N}} \, , \tag{4.5}$$

where σ_E is the standard deviation of the effect in question and N is the number of data points. Generally, standard error increases with a decrease in latitude for all four thickness effects. With regard to the dynamics and deformation plots, this is likely due to a decrease in CryoSat-2 satellite overpasses and increase in thickness variability and coastal interference in the lower latitudes leading to higher uncertainties in the CS2SMOS sea ice thickness product.

Thermodynamic effect standard error is lowest in the central Arctic where thermodynamic growth rates themselves are also quite low. Advection effects standard error is highest in the East Greenland, Barents and Kara Seas, where motion vectors are largest and most variable. In general, uncertainty is significant in the Kara, Barents and East Greenland Seas as well as most coastal regions.
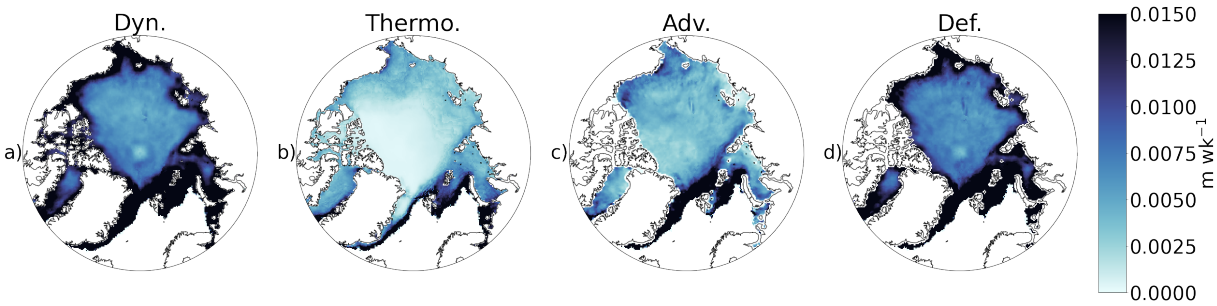
FIGURE 4.2: Uncertainty calculated as standard error for each grid cell during wintertime from late 2010 through early 2021 (except the winter of 2011-2012) sea ice thickness changes due to a) dynamic effects, b) thermodynamic effect, c) advection effect and d) deformation effect. Uncertainty increases with a decrease in latitude as the number of weeks with ice cover decreases.

Regional mean values across the analysis period for each effect are summarized in Table 4.1. Regional extent and location are shown in Fig. 4.3 and are defined per Meier et al. (2007). Thermodynamic growth is highest in regions with the lowest mean thickness, as expected by Eq. 3.8. The regional mean values of the dynamics, advection and deformation effects are all skewed downward by small, coastal sub-regions that exhibit very large negative thickness effects. In order to remove these effects, regional mean values excluding all grid cells within 200 km of a coast are shown in parenthesis. The strongest dynamic effect is exhibited in the Barents Sea, where the mean dynamic effect is -0.269 m wk^{-1} and -0.222 m wk^{-1} with coastal regions excluded, the bulk of which is made up of the deformation effect at -0.289 m wk^{-1} and -0.263 m wk^{-1} with coastal regions excluded. This region

also has the thinnest ice at 0.259 m and greatest thermodynamic growth of 0.257 m wk^{-1}. Mean dynamic effects are negative for every region except the central Arctic, where mean dynamic effects across the region are negligible. Notably, removal of coastal areas from the Laptev Sea decreases the magnitude of negative dynamic effect from 0.060 m wk^{-1} to 0.029 m wk^{-1} and in the Chukchi Sea, where both strong negative and strong positive dynamic effects are present, from 0.024 m wk^{-1} to 0.008 m wk^{-1}. Advection effects are small in all regions, all less than 0.021 m wk^{-1} in magnitude except in the East Greenland Sea where advection via ice export through the Fram Strait increases mean thickness by 0.113 m wk^{-1}. The advection effect is negative in all other regions except Baffin Bay and the Barents and Beaufort Seas which exhibit mean advection effects of 0.010 m wk^{-1}, 0.013 m wk^{-1} and 0.014 m wk^{-1}, respectively. The deformation effect magnitude is largest in Baffin Bay and the East Greenland and Barents Seas by a significant margin, at -0.251 m wk^{-1}, -0.247 m wk^{-1} and -0.289 m wk^{-1}, respectively. The remaining regions experience mean deformation effects that are at most 0.090 m wk^{-1} in magnitude and all negative, with the notable exception of the Central Arctic with a mean deformation effect of 0.008 m wk^{-1}. As with total dynamic effect, removal of coastal areas reduced the magnitude of negative deformation effect in the Laptev Sea, from 0.038 m wk^{-1} to 0.007 m wk^{-1}.

The mean advection and deformation fields show interesting patterns relative to the Beaufort Gyre and Transpolar Drift. North of the western portion of the Canadian Arctic Archipelago, the Beaufort Gyre advects thicker ice into the Beaufort Sea, leading to an increase in sea ice thickness in the region. As this ice is advected further west by the gyre in the Beaufort Sea, it
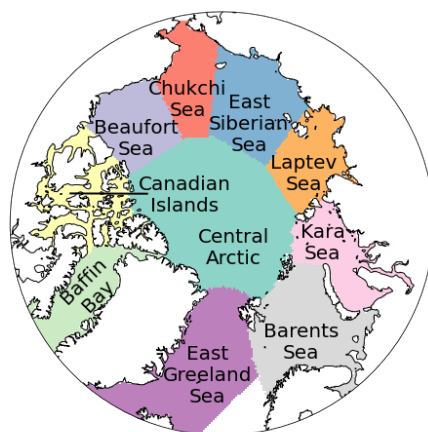
FIGURE 4.3: Location, extent and corresponding name of regions used in Table 1.

experiences a decrease in thickness due to deformation via lead formation by divergence in the flow. This ice continues to be advected through the Chukchi Sea and into the East Siberian Sea. The positive advection effect decreases in these regions however, as deformation has reduced the mean thickness of this ice, resulting in advection of thinner ice. The deformation effect in these regions is, however, positive, as the flow pattern deposits ice and leads to ridging, increasing the over sea ice thickness. The poleward leg of the Beaufort Gyre and Transpolar Drift are characterized by negative advection effects and positive deformation. In contrast to the westward leg of the Beaufort Gyre, the flow pattern in these regions is from thin ice towards thicker ice. This leads to a negative advection effect accompanied by a positive deformation effect due to ridging. The advection and deformation effects sum to a slightly positive dynamic effect here. The coastal regions of the Kara and Laptev Seas experience negative effects from both advection and deformation. These broad patterns are reinforced by the yearly data show in Fig. B.1 illustrating the effects that the location and strength of the Beaufort Gyre have on the advection and deformation fields on a yearly basis.

TABLE 4.1: Regional mean thickness, dynamic effect, thermodynamic effect, advection effect and deformation effect on thickness. Regional mean with 200 km from coastlines removed is shown in parenthesis. The Canadian Islands do not have advection effect or deformation effect results because ice motion vectors are not available in this region and do not have results for coastal regions removed because almost the entire region is coastal.

Region	Thickness [m]	Dynamics [m wk^{-1}]	Thermo. [m wk^{-1}]	Advection [m wk^{-1}]	Def. [m wk^{-1}]
Baffin Bay	0.383 (0.308)	-0.237 (-0.263)	0.240 (0.264)	0.010 (0.025)	-0.251 (-0.290)
East Greenland Sea	0.905 (0.863)	-0.121 (-0.145)	0.140 (0.145)	0.113 (0.145)	-0.247 (-0.316)
Barents Sea	0.259 (0.292)	-0.269 (-0.222)	0.257 (0.234)	0.013 (0.027)	-0.289 (-0.263)
Kara Sea	0.664 (0.698)	-0.104 (-0.090)	0.130 (0.122)	-0.013 (-0.014)	-0.090 (-0.077)
Laptev Sea	0.992 (1.123)	-0.060 (-0.029)	0.095 (0.074)	-0.021 (-0.022)	-0.038 (-0.007)
East Siberian Sea	1.192 (1.244)	-0.018 (-0.011)	0.070 (0.064)	-0.008 (-0.008)	-0.010 (-0.003)
Chukchi Sea	1.051 (1.132)	-0.024 (-0.008)	0.086 (0.074)	-0.007 (-0.003)	-0.015 (-0.005)
Beaufort Sea	1.424 (1.468)	-0.009 (0.000)	0.061 (0.051)	0.014 (0.019)	-0.022 (-0.019)
Canadian Islands	1.452	-0.027	0.075		
Central Arctic	2.105 (2.063)	-0.000 (0.001)	0.034 (0.031)	-0.009 (-0.012)	0.008 (0.012)
Entire Arctic	1.356 (1.380)	-0.032 (-0.040)	0.072 (0.076)	-0.003 (0.003)	-0.028 (-0.045)

Fig. 4.4 shows mean dynamics and mean deformation in relative terms as ratios to thermodynamic growth. These plots look similar to those in in Fig. 4.1 as the scaling quantity, thermodynamic growth, is fairly uniform across most of the Arctic. Nevertheless, the relative importance of dynamics to thermodynamic growth is an important result. Much of the Arctic shows a slightly negative impact of total dynamics relative to thermodynamic growth. The areas north of the Canadian Arctic Archipelago and Greenland show the highest relative
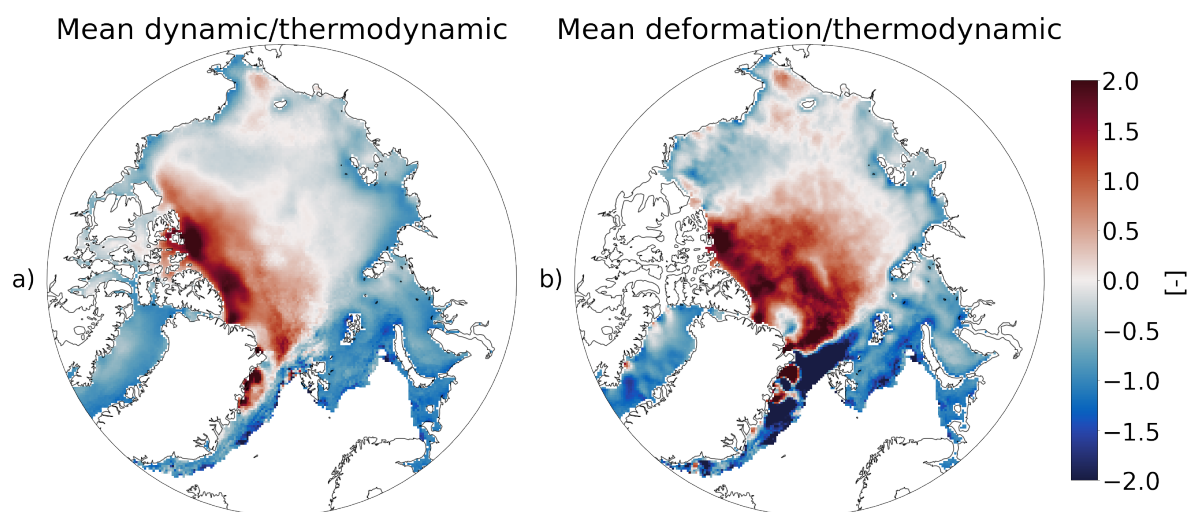
FIGURE 4.4: Wintertime mean from late 2010 through early 2021 (except the winter of 2011-2012) relative impact of a) dynamic effects over thermodynamic sea ice thickness growth and b) deformation (excluding advection) over thermodynamic sea ice thickness growth. Alternatively, the figure can be viewed as a) Eulerian dynamics and b) Lagrangian dynamics.

impact of dynamics, with some regions showing dynamics with twice the impact relative to thermodynamics. The coastal regions of the Kara and Laptev Seas show significant negative impacts of dynamics, with magnitudes nearly equal to thermodynamics. The greatest relative importance of deformation is also found in the regions north of the Canadian Arctic Archipelago and Greenland, though skewing more towards the central Arctic. In these regions deformation effects can be twice that of thermodynamics. The largest positive relative impact of deformation is found between Svalbard and Greenland where the Transpolar Drift causes ridging in thick ice that isn't experiencing large thermodynamic growth.

Fig. 4.5 shows the monthly mean overall dynamic effect, thermodynamic growth, deformation effect and advection effect across the ten winters of data. The monthly deformation fields depict a negative deformation effect in the westward leg of the Beaufort Gyre that peaks
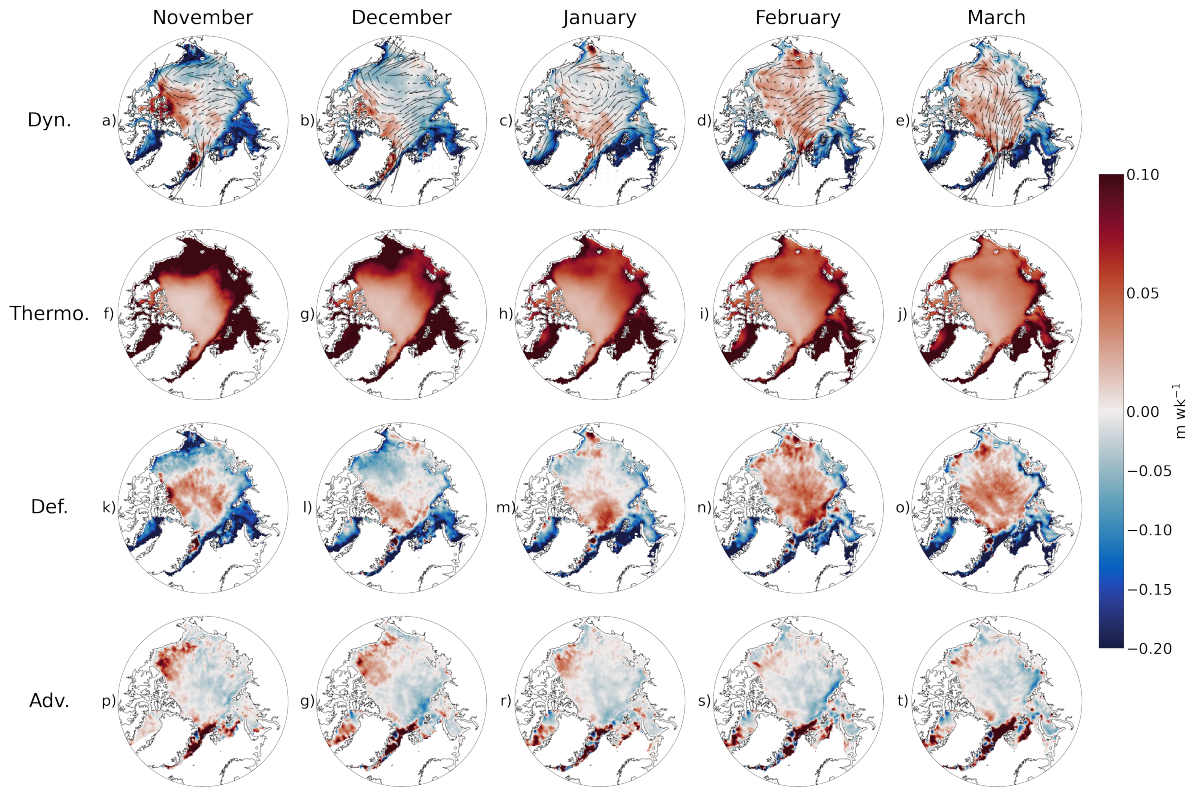
FIGURE 4.5: Monthly mean a-e) dynamic effect, f-j) thermodynamic effect, k-o) deformation effect, and p-t) advection effect over the analysis period. Dynamic and deformation effects increase through the growth season.

in December, decreases in January and is nearly absent in February and March. February and March do, however, depict deformation maxima north of Svalbard and Eastern Siberia. Positive advection of ice thickness by the Beaufort Gyre similarly peaks in the early winter, though the broad pattern of the advection field remains consistent throughout the winter. The deformation and advection fields sum to an overall dynamic effect that increases with time in winter, dominated by the deformation effect. The thermodynamic growth field, inversely proportional to sea ice thickness, remains consistently low across the Central Arctic through most of the winter and higher in the perennial ice zones, though growth decreases as thickness increases with time in these areas.
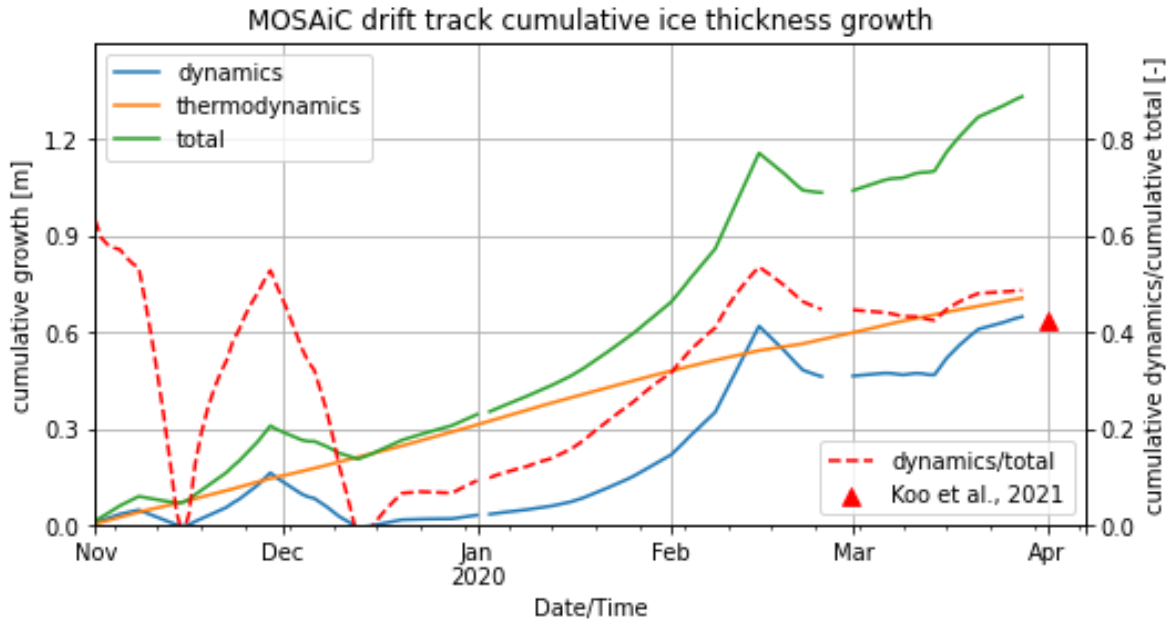
FIGURE 4.6: Cumulative dynamic effects (blue), thermodynamic (orange) and total (green) sea ice thickness growth (primary vertical axis) and cumulative dynamic effects over cumulative total sea ice thickness growth (secondary vertical axis) along the MOSAiC drift track. The red triangle represents cumulative dynamics over cumulative total growth over a similar area reported by Koo et al. (2021) who used ICESat-2 to determine dynamics vs. thermodynamics along the MOSAiC drift track. Dynamics accounts for nearly half of all thickness growth by 1 April 2020.

Fig. 4.6 the cumulative effects of deformation, i.e., Lagrangian dynamics, thermodynamics and their sum and relative magnitudes as experienced by the grid cell nearest to the MOSAiC drift station at each time step in order to compare these results with those reported by von Albedyll et al. (2022) and Koo et al. (2021). The analysis period is 1 November 2019 through 1 April 2020. Thermodynamic growth during the period is steady and consistent, ranging between 3.0×10^{-3} m d^{-1} and 6.0×10^{-3} m d^{-1}. Cumulative thermodynamic growth at the end of the period is 0.71 m. As expected, dynamic effects were much more variable, ranging from -2.1×10^{-2} m d^{-1} to 3.9×10^{-2} m d^{-1}. Dynamic effect maxima occurred in November and February and has a cumulative total of 0.63 m at the end of the period. Total growth

steadily rises due to the thermodynamic component and follows the shape of the dynamics component, with local peaks in November and February. The highest cumulative growth of 1.34 m is found at the end of the period. As a percentage of total growth, dynamics ends the season at 47.2% of the total growth. Over a similar study area, Koo et al. (2021) found dynamics to account for 42.6% of mean total growth.

4.4 Discussion

The climatology of ice motion during the CryoSat-2 era as plotted in Fig. 4.1 suggests the patterns of dynamic effect demonstrated here are sound. The Beaufort Gyre and Transpolar Drift both transport ice towards the Canadian Arctic Archipelago, where ridging causes both high positive dynamic effect and high positive deformation effect. Where the Transpolar Drift originates, in the coastal region of the Laptev Sea, strong negative dynamic and deformation effects dominate. Between these regions and the Canadian Arctic Archipelago, a couplet of negative advection effect and positive deformation effect characterizes a region where the Transpolar Drift tends to move thinner ice towards thicker ice, all the while experiencing ridging and other effects that increase thickness. Where the motion vectors show the Beaufort Gyre transporting ice westward from north of the Canadian Arctic Archipelago, a similar but reversed couplet of high positive advection effect and strong negative deformation effect is found. The ice is transported from a region of climatologically thicker ice north of the Canadian Arctic Archipelago to a region of climatologically thinner ice in the Beaufort Sea, leading to a positive advection effect. In this same region, the Beaufort Gyre flow pattern is diverging and accelerating westward. This divergence leads to lead formation

and a reduction in mean overall thickness, as reflected by negative deformation effects in this region. This matches previous work suggesting high divergence and lead formation in this region (Kwok, 2006; Willmes and Heinemann, 2016; Hoffman et al., 2019). As this ice is further advected westward around the Beaufort Gyre, the advection and deformation effects return to near zero and some ice is deposited north of Eastern Siberia where ridging leads to positive dynamic and deformation effects. The location and magnitude of these patterns varies year to year with sea ice flow patterns and likely atmospheric conditions as demonstrated in Fig. B.1.

Kwok (2006) reported on the spatial and seasonal characteristics of Arctic sea ice deformation in the ice motion vector fields using high resolution RGPS data from 1997-2000. Though the years in question do not overlap with the analysis period shown here, their results offer context for understanding dynamic sea ice effects. Their analysis showed divergence in the Beaufort Sea and convergence north of eastern Siberia, a pattern reflected here by negative deformation effects and positive deformation effects in those same regions, respectively. They show that the fraction of deformed ice in these regions decreases over the course of the growth season, a phenomenon also shown by a lessening of the negative deformation effects from November through March in Fig. 4.5. The ice motion vectors used here are not suited for vector calculus calculations of deformation terms as results from attempts at such calculation were unstable. A future comparison between concurrent observations of vector deformation fields and dynamics would be fruitful for model improvement.

The mean relative dynamic effect over total growth shown in Fig. 4.4 is useful for understanding the relative importance of dynamics and deformation and is useful for eventual comparison across time periods. The highest relative impact of dynamics is found north of the Canadian Arctic Archipelago where the Beaufort Gyre and Transpolar Drift both deposit ice and thermodynamic growth is limited due to the high thickness of the ice. The relative deformation plot tells a different story. With advection removed, this plot shows that a drifting observer would experience strong negative deformation effects due to fracturing relative to thermodynamic growth in the Beaufort Sea and increasingly strong positive deformation effects relative to thermodynamics in the Transpolar Drift and eastward leg of the Beaufort Gyre. Whereas many regions experience less than 25% relative impact of overall dynamics, few areas experience such a low impact of deformation. In the areas of low relative dynamic impact, advection nearly cancels this deformation. In the areas north of the Canadian Arctic Archipelago, both dynamics and deformation make up between 25% and 75% of total growth, consistent with Kwok and Cunningham (2016) who report 42%-56% of mean thickness change is due to deformation.

Within the methodology used here, the dynamic effects term represents Eulerian dynamics–i.e., a spatially stationary observer of sea ice thickness would observe changes due to thermodynamics and changes captured by the dynamics term, which includes advection. A Lagrangian observer, whom is advecting along a sea ice motion vector, would not experience changes due to this advection. The Lagrangian observer would only experience changes due to the deformation in the framework here. In this way, the Eulerian deformation term can

be considered Lagrangian dynamics. Two Lagrangian studies of dynamics observed along the MOSAiC drift track offer useful context for validating the Eulerian results (von Albedyll et al., 2022; Koo et al., 2021). The comparison is necessarily between the weekly Eulerian deformation term—i.e., Lagrangian dynamics—from closest in space and time to the MOSAiC drift track and dynamics as described within those studies.

von Albedyll et al. (2022) reported 10% dynamic sea ice thickness growth relative to total growth along the MOSAiC drift, lower than the lower than the 48.7% reported here and the 42.6% reported by Koo et al. (2021). A likely primary cause of this discrepancy is related to temporal resolution. von Albedyll et al. (2022) analyzed AEM sea ice thickness distributions across the 50 km buoy network at the beginning of the growth season and at the end of the growth season, estimating a cumulative thermodynamic growth during the season using buoy thicknesses. Through a phenomenon acknowledged by the authors, this does not account for dynamics affecting thermodynamic growth throughout the growth season. If dynamics were to increase thickness, as these results and those reported by Koo et al. (2021) show did indeed occur along the MOSAiC drift track, thermodynamic growth rate would decrease as shown in Eq. 3.8. Without accounting for this effect, thermodynamic growth is overestimated and dynamically driven growth is underestimated, due to the latter being calculated as a residual. The higher temporal resolutions in this work and Koo et al. (2021) greatly improve—though do not eliminate—this issue. Indeed, von Albedyll et al. (2022) report a cumulative thermodynamic growth of 1 m, whereas here thermodynamic growth of 0.7 m is reported. This is significant, especially given von Albedyll et al. (2022)

measured growth between 14 October and 17 April, whereas the analysis period here is from 1 November to 1 April (this time discrepancy alone may cause differences as well).

Another potential reason for discrepancy between the results reported here and those of von Albedyll et al. (2022) is the higher overall thickness growth measured by CryoSat-2 relative to the AEM measurements. A total mean growth along the MOSAiC drift track of 1.3 m is reported here relative to 1.1 m from the AEM survey. Indeed, CS2SMOS shows a mean sea ice thickness of 2.52 m on 1 April 2020 at the MOSAiC location relative to 2.2 m from the AEM surveys. This would manifest as an increase in dynamic effect in the analysis shown here, as dynamics is calculated as a residual when thermodynamics are subtracted from total growth. That there are differences here is not surprising. The satellite measurements are gridded and taken from the nearest grid cell to MOSAiC, while the AEM surveys are centered on the MOSAiC buoy array. On the other hand, though the AEM has higher spatial resolution, the coverage over the 50 km buoy network is not complete. The satellite samples a larger area, although not centered exactly on the MOSAiC buoy array. That the results reported here agree better with Koo et al. (2021) is not surprising, given both studies have used satellite sea ice thickness as the primary dataset. Given that this study aims at a temporally and spatially larger scale while these studies are more focused on singular drift track, differences in results are expected while using these more localized studies to provide context for this larger scale study.

The calculations and analyses carried out here are all performed using satellite data on a 25 km EASE-Grid 2.0. Whereas sea ice processes can occur on much smaller scales, the results

on satellite scale are useful for deciphering patterns and trends on an Arctic basin-wide basis. The CS2SMOS sea ice thickness dataset represents mean sea ice thickness within each grid cell. In actuality, thickness over the grid cell is defined by a distribution rather than a single value. However, without having observed local thickness distributions available at each time step, thickness distributions were omitted and the SLICE retrieval applied using the mean thickness provided by CS2SMOS. It is likely that implementing thickness distributions would augment these results. Given the non-linear and inverse relationship between thickness and thermodynamic growth rate present in Eq. 3.8, a distribution favoring ice thinner than the mean thickness over that thicker than the mean within a grid cell would increase thermodynamic growth and decrease dynamic effects (and vice versa). Though snow–ice interface temperature is not expected to vary as greatly as sea ice thickness across a 25 km grid cell, passive microwave snow–ice interface temperature retrieval also represents the mean across each grid cell. The dynamic, thermodynamic, advection and deformation effects then necessarily represent mean effects over the grid cell area. While few areas within a grid cell will have experienced exactly the effects described by these results, the cell will have experienced these effects on the mean.

The largest source of uncertainty is that from the AWI CS2SMOS sea ice thickness product. The AWI CS2SMOS product merges sea ice thickness retrievals from CryoSat-2 and SMOS into a product that contains reduced uncertainties relative to each instrument's products independently (Ricker et al., 2017b). CryoSat-2 uncertainties are highest over thin ice while

SMOS uncertainties are highest over thick ice, creating the opportunity for synergy. CryoSat-2 uncertainties are made up of observational uncertainties or noise and systemic uncertainties or bias (Ricker et al., 2014). Observational uncertainties are reduced through spatial averaging on the grid and optimal estimation methodology used to create the CS2SMOS product. While systemic uncertainties effect estimates of absolute thickness, differencing of thickness between time steps removes them from the estimations of various thickness effects calculated in this work. SMOS uncertainties are caused by uncertainties in the input parameters to the energy budget used to estimate sea ice thickness and are especially high over MYI, results from which are removed from the optimal interpolation. The AWI CS2SMOS product provides an uncertainty value including these effects for each individual estimate at each time step and grid cell. Figure 4.7 shows a standard error and relative standard error calculated using a mean of these uncertainties and mean ice thickness across the study time period and area. The magnitudes of this mean uncertainty range from 0.005 m to 0.01 m and increases with a decrease in latitude, with some regions experiencing a mean uncertainty of 0.015 m and greater. Relative uncertainty is below 5% across most of the study area. The overall CS2SMOS sea ice thickness observational uncertainty effects uncertainty in all four calculated effects. The thermodynamic effect is affected via the presence of sea ice thickness, H, in Eq. 3.8. Relative uncertainty due to this term is equal to the relative uncertainty of this term itself and mostly less than 5%, as shown in Fig. 4.7b. The thermodynamic component is also affected by any systemic bias present in the CS2SMOS product. The dynamic effect is calculated as a residual of thermodynamics and overall thickness change. The mean uncertainty shown in Fig. 4.7a is very similar to the uncertainty of the dynamic effect as shown

in Fig. 4.2, lending credibility to these uncertainty estimates. The ratio of mean dynamic effect over thermodynamic growth, shown in Fig. 4.4, is particularly sensitive to uncertainty or bias in the CS2SMOS product. An underestimation of sea ice thickness would lead to overestimation of thermodynamic growth and underestimation of dynamic effect, altering both the numerator and denominator of the ratio of the two. The advection term is also affected by the CS2SMOS thickness uncertainty as it is calculated using a spatial gradient of the thickness field. The deformation term is affected by the CS2SMOS uncertainty as it is calculated as the difference between overall dynamics and advection.
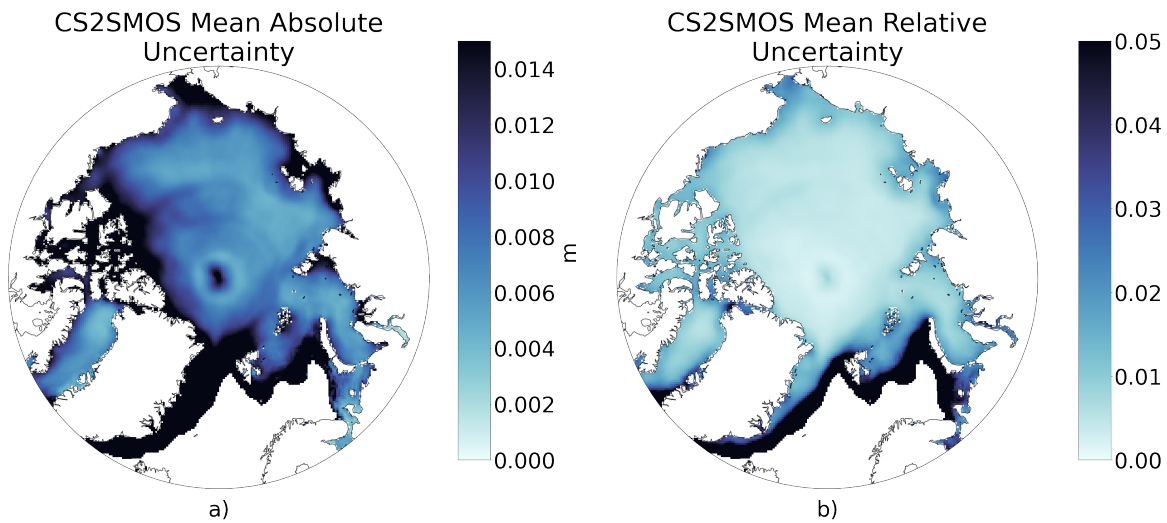
FIGURE 4.7: Mean AWI CS2SMOS (a) absolute uncertainty and (b) relative uncertainty during wintertime from late 2010 through early 2021 (except the winter of 2011-2012) as provided by the data product. This uncertainty is very similar in magnitude and pattern to uncertainty in dynamic effect and is mostly far below 5%.

Chapter 3 reports SLICE to have a thermodynamic growth mean bias of 4×10^{-4} m d^{-1} and standard deviation bias of 2.2×10^{-3} m d^{-1} when compared against buoy data. Calculating a standard error from this standard deviation using a total number of samples of 227 leads to an uncertainty contribution of 0.001 m wk^{-1}. The assumption of 2 Wm^{-2} of basal flux

from liquid water to solid sea ice leads to additional uncertainty from SLICE. Assuming a density of 917 kg m^{-2} and a latent heat of fusion of 3.32 x 10^5 J kg^{-1}, each 1 W m^{-2} of basal sensible heat flux from the liquid sea water to solid sea ice is equivalent to a sea ice thermodynamic growth rate of 2.84×10^{-4} m d^{-1}. If the assumed 2 W m^{-2} basal sensible heat flux were removed, sea ice growth would increase by 5.67×10^{-4} m d^{-1} and an increase from 2 W m^{-2} to 10 W m^{-2} would decrease thermodynamic sea ice thickness growth by 2.27×10^{-3} m d^{-1}. The SLICE thermodynamic growth retrieval also does not account for lateral melt and freeze processes.

A potential mechanism for error occurs in the relationship between lead frequency and the snow–ice interface retrieval results. Leads and areas of lower sea ice concentrations necessarily contain open sea water exposed at the surface. Sea water has significantly lower emissivity in the microwave band than sea ice, therefore reducing passive microwave brightness temperatures in these regions. To the extent that leads of open water covers a grid cell, these lower brightness temperature would then artificially reduce the retrieved snow–ice interface temperature and cause erroneously large thermodynamic growth rates. Via Eq. 4.3, erroneously high thermodynamic growth without a change to the CS2SMOS estimates leads to erroneously lower dynamic effects. This phenomenon is difficult to spot because negative dynamic effects are indeed expected in regions with high lead frequency. This analysis is restricted to sea ice concentrations of greater than 95% as retrieved by established passive microwave methods. As such, the highest possible open water fraction within a grid cell is 5%. Assuming emissivity of a satellite field of view is a linear sum of scene type emissivities

weighted by area fraction, the effect of 5% open water by area on satellite retrieved snow–ice interface temperature can be approximated. Using an approximate open water emmissivity at 6.9 GHz of 0.56 and sea ice emmissivity of 0.98, the emissivity of a 95% sea ice concentration is 0.959. This reduction in emissivity from 0.98 for a 100% sea ice concentration scene equates to a 5.25 K reduction in brightness temperatures for a 250 K snow–ice interface temperature. Propagating this difference through the retrieval algorithm per Kilic et al. (2019) leads to a reduction of retrieved snow–ice interface temperature of 6 K. In a scenario with thin ice and a small temperature gradient across the ice, this difference could be significant.

Motion vector uncertainty adds to the uncertainty in advection effect and the deformation effect calculated as a residual between dynamic effect and advection effect. Tschudi et al. (2020) lists a maximum ice motion error of 0.7 cm s^{-1} which corresponds to 605 m d^{-1}. The contribution of this error to advection effect and deformation effect error is reduced by spatial gradients in the sea ice thickness fields being small. The highest uncertainties in advection effect are found in the Greenland and Barents Seas where motion vectors and thickness gradients are largest.

4.5   Summary

Sea ice models, including those contained within global climate models, account for sea ice thickness and volume through separate thermodynamic and dynamic processes. These processes are affected by different mechanisms in a changing climate, meaning independent observations of each are essential for comparison with model results to ensure each process

is correct independently, regardless of whether overall thickness is correct. In this study, I present the first basin-wide, Eulerian, sub-seasonal temporal resolution, and long-term estimation of dynamics effect on sea ice thickness, thermodynamic sea ice thickness growth, advection effect on sea ice thickness and deformation effect on sea ice thickness. By retrieving thermodynamic sea ice thickness growth by driving a simple model with passive microwave based snow–ice interface temperature observations and differencing this growth on a weekly basis from overall sea ice thickness growth calculated from a satellite altimeter and passive microwave combination sea ice thickness product (Ricker et al., 2017b), wintertime, basin-wide sea ice dynamic effects on a spatial and temporal scale beyond the localized and seasonal studies available to date are presented. Using a sea ice motion product (Tschudi et al., 2020), the overall dynamic effect was separated into its Eulerian, independent component effects of advection and deformation.

Thermodynamic growth is lowest in the central Arctic, lower than 0.04 m wk^{-1}, and highest in the seasonal ice zones, often greater than 0.08 m wk^{-1}. The highest positive dynamic effects of greater than 0.04 m wk^{-1} are found north of the Canadian Arctic Archipelago, where the Transpolar Drift and Beaufort Gyre deposit ice. Strong negative dynamic effects of greater than 0.08 m wk^{-1} are found where the Transpolar Drift originates. The deformation and advection effect fields are dominated by couplets with opposite sign between the two. The Beaufort Sea is characterized by positive advection effects of 0.04 m wk^{-1} and negative deformation effects of similar magnitude, while most other regions are characterized by negative advection effects, sometimes as low as -0.04 m wk^{-1} and positive deformation

effects, often times greater than 0.04 m wk^{-1}. The highest dynamic effect relative to thermo-dynamic effect is found north of the Canadian Arctic Archipelago, where dynamics account for twice the sea ice thickness growth as thermodynamics. Similarly, deformation is highest relative to thermodynamics in these regions as well, with deformation more than doubling thermodynamics here and slightly farther north, near the North Pole. A seasonal cycle is also shown for all thickness effects effects, the most prominent feature of which is an increasing positive deformation thickness effect and overall dynamic thickness effect as the winter season progresses. A potential mechanism for this is increasing ice thickness resisting lead formation and making more ice volume available for ridging.

Yearly results compare well with a recent study of the Lagrangian dynamic and thermodynamic effects on sea ice thickness along the Multidisciplinary drifting Observatory for the Study of Arctic Climate (MOSAiC) drift track during the winter of 2019-2020. Where these data shows Lagrangian dynamics accounting for 48.7 % of growth in the grid cells nearest the drifting study area during this time period, Koo et al. (2021) found similar results of 42.6 % over a similar spatial scale. This lends confidence in these larger spatial and temporal scale results.

The most significant source of uncertainty in all four effects, thermodynamics, dynamics, advection, and deformation, is the uncertainty in the AWI CS2SMOS sea ice thickness product. The mean uncertainty in this product over the study period is similar to the standard error in the dynamics and deformation fields. Both AWI CS2SMOS sea ice thickness and

the standard error in the results reported here have similar magnitudes and are potentially significant in the Kara, Barents and East Greenland Seas as well as most coastal regions.

Next steps for this data include further interrogation of trends and patterns. There may be a relation to atmospheric conditions or patterns like the Arctic Oscillation or trends related to the changing climate. An additional step will be comparison of these results to those given by sea ice and global climate models.

4.6 Code and data availability

Data used in creation of all figures within this chapter is available at `https://doi.org/10.5281/zenodo.7278280`. Code for creation of data and figures within this chapter is available at `https://doi.org/10.5281/zenodo.7292123` and `https://github.com/janheuser/thmdyn`. The following auxiliary datasets were used and are available at these locations: AMSR-E and AMSR2 brightness temperatures, `https://doi.org/10.5067/AMSR-E/AE_SI25.003` and `https://doi.org/10.5067/TRUIAL3WPAUP`; AMSR-E and AMSR2 SIC, `https://doi.org/10.5067/AMSR-E/AE_SI25.003` and `https://doi.org/10.5067/TRUIAL3WPAUP`; AWI CS2SMOS, `https://www.meereisportal.de`; sea ice motion vectors, `https://doi.org/10.5067/INAWUWO7QH7B`; MOSAiC drift track, `https://doi.pangaea.de/10.1594/PANGAEA.937193`;

Chapter 5

Sea ice dynamic and thermodynamic thickness effects in climate models

5.1 Background

Global climate model simulation results are often used to project future Arctic sea ice conditions (Flato and Participating CMIP Modelling Groups, 2004; Arzel et al., 2006; Smith and Stephenson, 2013; Wang and Overland, 2015; Lebrun et al., 2019; Notz et al., 2020; Arthun et al., 2021). Comparison between observations and models of historical and present conditions is essential to building confidence in these projections. Processes that contribute to key outputs must also be compared against observations, lest the model be "right for

the wrong reasons". This is especially important given that the individual processes contributing to a key variable may be affected by differing mechanisms in a changing climate, an understanding of which is necessary for improved future projections.

Sea ice conditions as modelled by global climate models and PIOMAS have been extensively compared against available observations (e.g., Stroeve et al., 2007; Boe et al., 2009; Massonnet et al., 2012; Shu et al., 2015; Shu et al., 2020). While the mass budget of sea ice categorized by process has been explored (Holland et al., 2010; Keen et al., 2021), absent from this body of literature is any comparison of models' representation of thermodynamic sea ice thickness growth and dynamic sea ice thickness effects against observations of these independent processes. The primary reason for this is the lack of such observations. In Chapter 4, I presented the first basin-wide, Eulerian, sub-seasonal temporal resolution, and long-term observational estimation of these effects, making such a comparison possible for the first time. Here overall ice thickness, overall ice thickness growth, thermodynamic sea ice thickness time tendency and dynamics sea ice thickness time tendency from the CESM1-LE, the CESM2-LE, CESM2 OMIP2 and PIOMAS are compared to the observations presented in Chapter 4.

5.2   Methods

Each of the three climate models, CESM1-LE, CESM2-LE, and CESM2 OMIP2 and PIOMAS output a thermodynamic sea ice time tendency term and a dynamic sea ice time

tendency term that mirror the first and second terms in Eq. 4.1 and 3.1 and likewise the observational estimates shown in Chapter 5.

In order to compare each of these model datasets to one another and to the observational estimates from Chapter 4, the thickness datasets were converted to m and tendency datasets to m d^{-1}. Of note is the conversion from the sea ice mass tendencies output by the CESM2 OMIP2 to the sea ice thickness tendencies in m d^{-1}. While the output in mass units is useful for energy calculations and perhaps a more consistent metric through not requiring an assumed density (which varies across observations and models), results are reported in thickness tendencies here in keeping with literature and previous results. In keeping with Section 3.2.2.3 and Alexandrov et al. (2010), a density of 917 kg m^{-3} was used for this conversion in order to maintain consistency. The datasets were also interpolated from their native Greenland Pole grids to the 25km EASE-Grid 2.0. All datasets span November through March from the years 2010 through 2021 (except November 2011 through March 2012) except the CESM2 OMIP2 simulation which only covers through 2018. For comparisons with CESM2 OMIP2, the observation time steps after 2018 have been removed. Mean fields shown for both large ensembles are both time mean and ensemble mean.

5.3   Results

Figure 5.1 shows a summary of mean sea ice thickness, sea ice thickness change, dynamic sea ice effect and thermodynamic sea ice growth from the observations described in Chapter

4. These results are described in depth in Chapter 4 and provided here for reference along with the remaining figures.
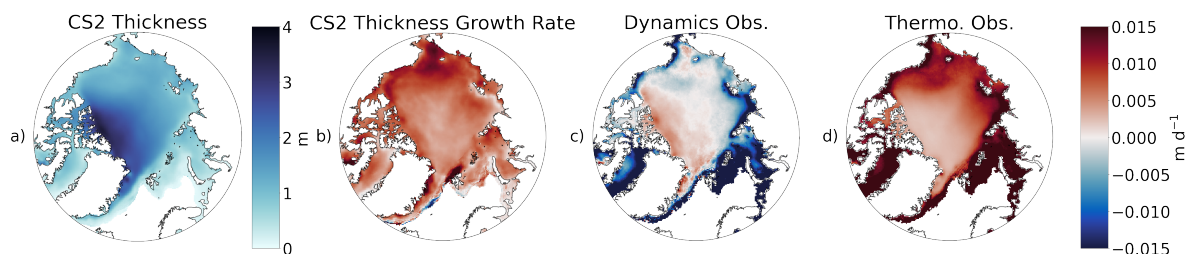
FIGURE 5.1: Mean a) sea ice thickness, b) daily sea ice thickness growth rate, c) daily dynamic sea ice thickness effect, and d) daily thermodynamic sea ice thickness growth rate observational estimates in the Northern Hemisphere during winters from 2010 to 2021 (excluding 2011-2012).

Mean dynamic sea ice changes and their differences with observations are shown in Fig. 5.2. Mean dynamic effects from all four models are very similar, with dynamics leading to sea ice thickness increases in the Beaufort, Chukchi and East Siberian Sea and decreases in much of the remainder of the Arctic sea ice pack. The exception is PIOMAS which exhibits a region of dynamic sea ice thickness increases north of the Canadian Arctic Archipelago. Sea ice thickness is also increased due to dynamics for all models in the East Greenland Sea, where sea ice drift advects ice. Baffin Bay has areas of both thickness increase due to dynamics and thickness decrease due to dynamics in each model dataset, with slightly different orientations.

The dynamics fields look similar for each model, as do the differences between the dynamics and the observations. The central Arctic does not have enough sea ice thickness increase due to dynamics in all four models. On the other hand, the models overestimate sea ice

thickness increase due to dynamics in the coastal regions of Arctic other than the Canadian Arctic Archipelago where the Transpolar Drift and Beaufort Gyre deposit ice. A large prominent region of overestimated sea ice thickness increase due to dynamics is also shown in the Chukchi Sea. The CESM1-LE and CESM2-LE model ranges encompass the observations of dynamic effect in only some regions, typically where regions of overestimated and underestimated dynamic effect meet.

FIGURE 5.2: Mean (a-d) model dynamic sea ice thickness effect in the Northern Hemisphere during the winters from 2010 to 2021 (excluding (2011-12) and (e-h) differences between model and observational estimates of mean dynamics during the same time period. Black dots signify areas where the observational estimate lies within the model large ensemble range. Dynamic sea ice thickness effects are underestimated in the central Arctic and overestimated in most other regions.

The thermodynamic growth fields from all for models, shown in Fig. 5.3, also look similar, with fairly consistent growth rates across the Arctic. The two large ensemble means are especially similar to one another as are the CESM OMIP2 and PIOMAS results. The latter two model simulations contain slightly more variation of growth rate across the Arctic with more growth exhibited in coastal regions and regions where climatology would expect thinner ice.

The differences between the models and observations suggest the models are far too consistent in growth rate across the Arctic, with two much thermodynamic growth exhibited in the Central Arctic and north of the Canadian Arctic Archipelago and two little thermodynamic growth exhibited in the Chukchi, Kara and Barents Seas. Again, the large ensemble range includes the observations in very few areas and typically in areas where regions of overestimated and underestimated thermodynamic sea ice growth meet.

FIGURE 5.3: Mean (a-d) model thermodynamic sea ice thickness growth rate in the Northern Hemisphere during the winters from 2010 to 2021 (excluding (2011-12) and (e-h) differences between model and observational estimates of mean thermodynamic growth rate during the same time period. Black dots signify areas where the observational estimate lies within the model large ensemble range. Thermodynamic growth is overestimated in the central Arctic and underestimated in most other regions.

Mean total sea ice changes including both thermodynamic and dynamic sea ice thickness changes are shown in Fig. 5.4. The models are less consistent with one another here. CESM2-LE shows very consistent sea ice thickness growth across the entire Arctic, while the other three model datasets show significantly more variation. These other three model datasets show higher mean total sea ice thickness growth in the seasonal ice zones where the ice is typically thinner.

In contrast to the comparisons of dynamic and thermodynamic effects individually that are shown in Figs. 5.2 and 5.3, the total growth comparison depicted in Fig. 5.4 shows that models produce a total growth that is more consistent with observations. In particular, the CESM1-LE encompasses the observations over a much larger portion of the Arctic, nearly all, than it does for each growth component independently. The CESM2-LE range encompasses the observations over less Arctic area than the CESM1-LE, though more than it does for thermodynamic and dynamic effects individually. All four model differences with observations are less than the individual growth components. PIOMAS overestimates growth over nearly the entire Arctic, while the other three models underestimate growth in the Chukchi Sea.
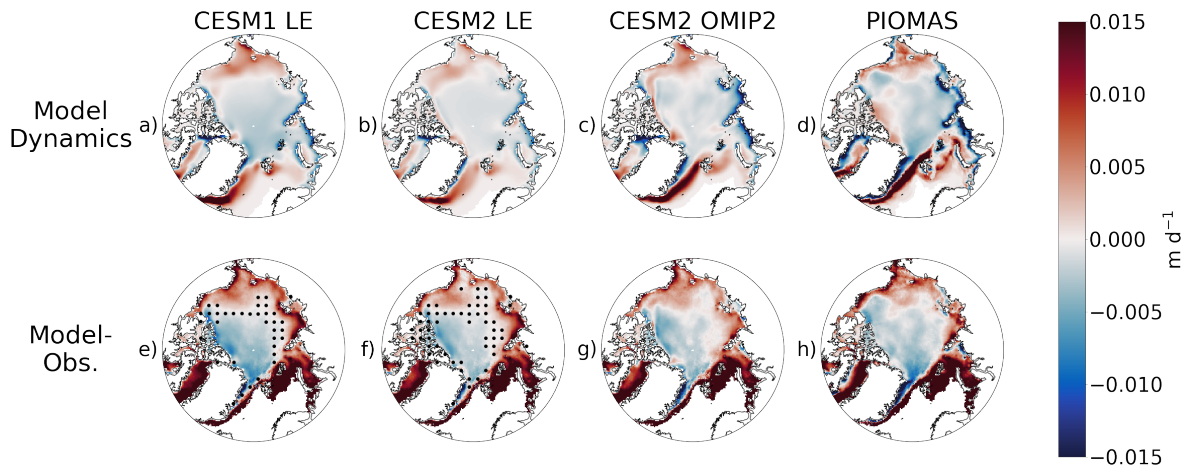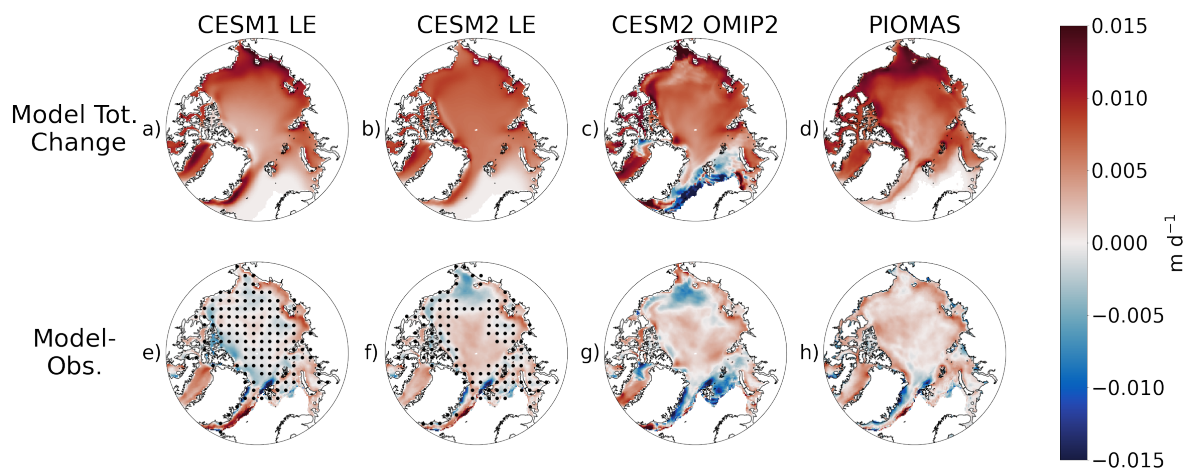

FIGURE 5.4: Mean (a-d) total sea ice thickness growth rate in the Northern Hemisphere during the winters from 2010 to 2021 (excluding 2011-12) and (e-h) differences between model and observational estimates of mean total growth rate during the same time period. Black dots signify areas where the observational estimate lies within the model large ensemble range. Models perform better modeling total growth than they do modelling thermodynamic or dynamic effects independently.

Adding context is the mean overall thickness plotted in Fig. 5.5. CESM2-LE has noticeably lower sea ice thickness than the other three model simulations. All models show the thickest

ice north of the Canadian Arctic Archipelago, with the CESM model simulations showing localized thick ice in a linear shape in this region and PIOMAS showing a larger pattern of thicker ice extending towards the North Pole and Central Arctic.

Again, the CESM1-LE performs better than the CESM2-LE, with much of the CESM1-LE Arctic sea ice thickness ensemble range range encompassing the observations. The CESM2-LE significantly underestimates sea ice thickness over much of the Arctic, especially the central Arctic, and encompasses the observations in fewer locations than CESM1-LE. The CESM2 OMIP2 also significantly underestimates sea ice thickness in the Central Arctic while CESM1-LE and PIOMAS underestimate ice thickness here as well, though to a lesser degree. Sea ice thickness is overestimated by CESM1-LE, CESM2 OMIP and PIOMAS over a broad general region encompassed by the Beaufort, Chukchi, Kara, and Barents Seas.
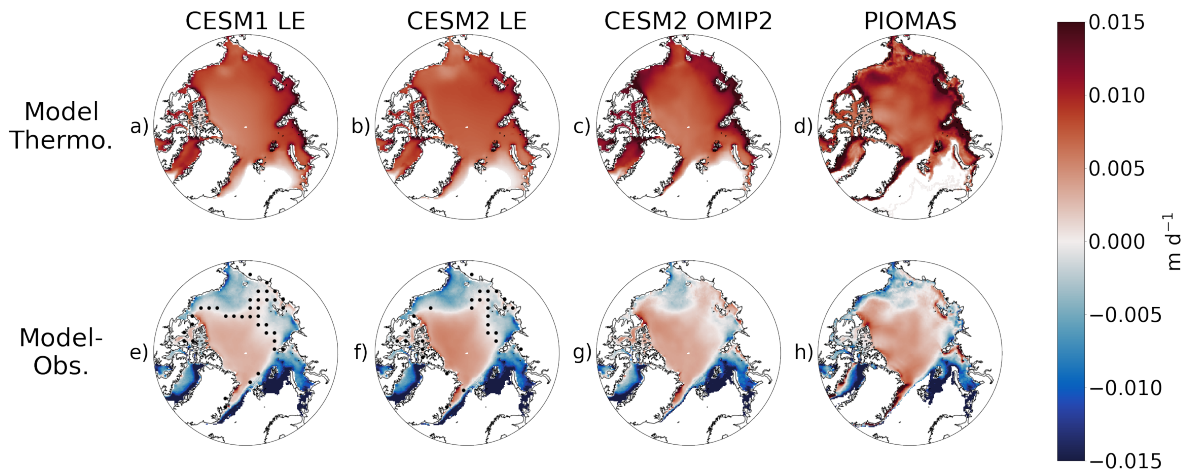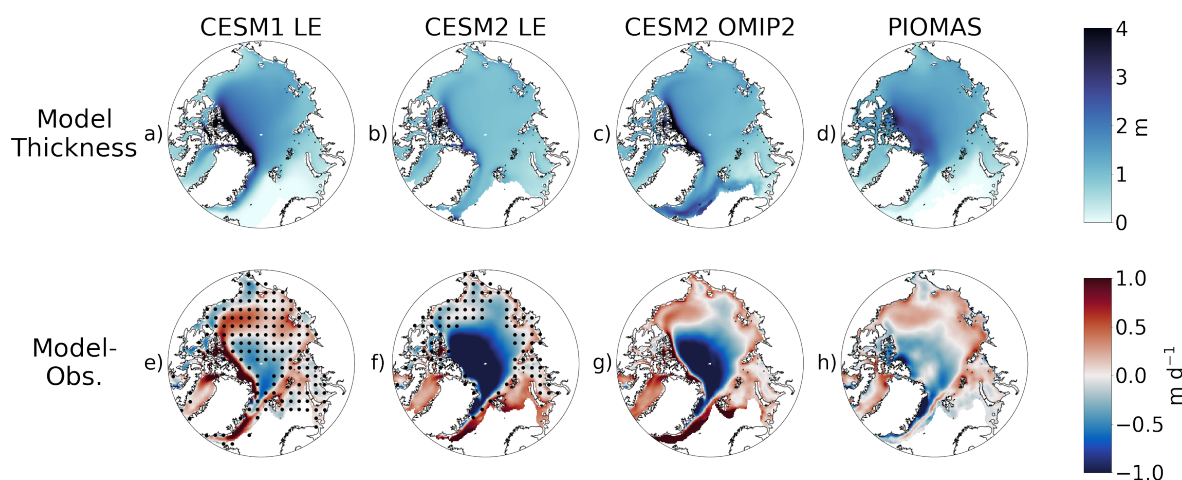

FIGURE 5.5: Mean (a-d) model sea ice thickness in the Northern Hemisphere during the winters from 2010 to 2021 (excluding 2011-12) and (e-h) differences between model and observational estimates of mean sea ice thickness during the same time period. Black dots signify areas where the observational estimate lies within the model large ensemble range. The pattern of difference between models and observational estimates may contribute to the difference in thermodynamic growth between models and observational estimates.

5.4   Discussion

All four model datasets show significantly more accurate total sea ice thickness growth during the 2010-2021 study period than the constituent processes of thermodynamic and dynamic growth. This is shown by smaller differences between the models and observations of total growth than that for each individual process. Crucially, the CESM1 and CESM2 model ensembles also encompass observations of total growth and overall thickness over much more area than for each individual process. This result is also supported by the compensating differences between observations and thermodynamic effects having a similar pattern but opposite sign to the differences with dynamic effects. When summed, these resultant total growth difference patterns are closer to zero and more consistent. Given that observational estimates of thermodynamics and dynamics separately have not yet been available until this work, these results are not unexpected. The only thickness metric available to date, albeit with some uncertainty, has been overall thickness and its time differences.

That all four models show very similar results is also not unexpected. All four of these models rely upon the same canonical literature and model strategies and utilize the same POP ocean model, though differing versions between PIOMAS (version 1) and the CESM datasets (version 2). CESM2 OMIP2 and PIOMAS include reanalysis forcings and as such should more closely match observations. That they do not suggests the model deficiencies are of greater scale in the model results than the forcing. All four model datasets, and likewise even the observational estimates in Chapter 4, use a governing sea ice thickness equation as described by Thorndike et al. (1975). This governing equation accounts for sub-grid scale

thicknesses by discretizing thickness across each grid cell into thickness bins and accounting for the changes in area coverage of each thickness bin and accounting for bin-to-bin transport via sea ice thermodynamic growth and melt. A ridging term in the equation accounts for bin-to-bin transport through dynamics. Thermodynamics is accounted for via one-dimensional numerical modelling as first described by Maykut and Untersteiner (1971), progress beyond which amounts mostly to refinements of and additions to their fundamental concepts. A momentum balance accounts for the various forces acting on sea ice and determines the ice motion field. Essential to this component of the models is a rheology relationship of stress to strain within the ice pack. Various rheological relationships have been employed, including viscous-plastic (Hibler, 1979) in PIOMAS and elastic-viscous-plastic (Hunke and Dukowicz, 2002) in CESM/CICE. The rheology and ridging relationships are what determine what results when a local stress is applied to a parcel of ice. Does the ice move? Does the ice ridge upon nearby ice? Does the ice break free of surrounding ice and form a lead? Does the ice remain in place and compress? It is likely in these relationships that adjustments must be made in order for the models to more accurately reflect observational estimates of thermodynamic effects and dynamic effects. The models do not exhibit enough dynamic increase in western hemisphere and too much in eastern hemisphere. They need to account for more redistribution of thickness by the Transpolar Drift and Beaufort Gyres both. It is also possible that the underlying ocean circulation needs to be adjusted to achieve these dynamic effects as well, especially given that the CESM models and PIOMAS all use versions of the POP ocean model. A detailed study of what adjustments are necessary to achieve this result is beyond this scope of this work.

In a changing climate, the thermodynamic growth of sea ice is affected by changes to ice, ocean and atmosphere temperatures while dynamic effects are affected by changes to ocean and atmospheric circulations as well as ice strength. Though these two mechanisms are certainly related, they are distinctly unique from one another to first order. Additionally, their interactions are not well understood. Without correctly partitioning thermodynamics and dynamics in today's climate, models may not accurately predict sea ice conditions in a future climate. Additionally, incorrect patterns of thermodynamic growth within a model will thermally feed back upon the surface energy balance atmospheric conditions. Per Section 3.2.2.3, latent heat of fusion for sea ice at 33 ppt salinity is 332156 J kg^{-1}. At a density of 917 kg m^{-3}, a typical thermodynamic sea ice growth rate of 0.005 m d^{-1} conducts 18 W m^{-2} through the ice layer to the snow and atmosphere. This heat flux is equal to the Arctic mean surface energy exchange between the atmosphere and snow–ice column in September and April during seasonal changes and one third of the surface energy exchange during winter months (Serreze et al., 2007). This is particularly important given that the seasonal cycle of the Arctic energy budget is largely modulated by net surface flux (Serreze et al., 2007).

Interestingly, CESM1 seems to exhibit sea ice thickness processes more accurately than CESM2 when compared against the results of Chapter 4. The CESM1-LE contains the observations in more regions for sea ice thickness shown in Fig. 5.5. This figure also shows the CESM2-LE significantly underestimates sea ice thickness over large portions of the Arctic, particularly in the Central Arctic where differences with observations are as high as or greater than 1 m. CESM2 OMIP2 also underestimates sea ice thickness in that region and

to the same degree, indicating that the atmospheric forcing is not the source of the model deficiency. The underestimation of sea ice thickness in CESM2 is a documented phenomenon (DuVivier et al., 2020). Figures 5.4 and Figures 5.3 show that the CESM1-LE encompasses total growth and thermodynamic growth observations in more regions than the CESM2-LE. CESM1-LE and CESM2-LE perform similarly regarding dynamically driven sea ice thickness changes (Fig. 5.2). DeRepentigny et al. (2020) notes that CESM2 sea ice biases are driven primarily by low-biased summer sea ice thicknesses. This may be why these results show that even though CESM2 underestimates overall mean state sea ice thickness in the Central Arctic, it still overestimates total growth in this region as it begins the growth season with significantly underestimated sea ice thickness that is not remedied by the overestimated growth.

This study is a first step towards understanding how climate models represent the processes that influence sea ice thickness and how these processes compare with current real world conditions in observational estimates. A next step is understanding how these processes change over time. It is not yet clear how sea ice dynamic effects have changed over time as global temperatures increase and Arctic sea ice extent and concentrations decline. As such, there is not yet a way to determine if trends in these processes exhibited by climate models reflect reality. With an eventual extended dataset of sea ice dynamics observations in hand, a comparison with climate model trends will be investigated in the future.

5.5   Summary

Observations of thermodynamic sea ice thickness growth and dynamic sea ice thickness effects presented in Chapter 4 made possible the first examination of these processes as represented by global climate models and a sea ice model reanalysis product. All four models, CESM1-LE, CESM2-LE, CESM2 OMIP2 and PIOMAS, exhibit a similar pattern of underestimated dynamic sea ice thickness increase and overestimated thermodynamic sea ice thickness growth in the central Arctic, and vice versa in the regions where the Transpolar Drift originates and the Chukchi, Barents and Kara Seas. These patterns of thermodynamic growth and dynamic effect sum to and overall sea ice thickness change and overall sea ice thickness patterns that more closely match observations than the individual processes themselves.

That all four model datasets show similar results is not surprising, given that the sea ice model components within each are built upon the same fundamental studies and ocean model. PIOMAS and CESM2 OMIP2 don't perform significantly better than CESM1-LE or CESM2-LE, though both include reanalysis data as forcing. This suggests the process level deficiencies are inherent to the model itself rather than forcings. CESM2 performs worse than CESM1 in these comparisons. The CESM2-LE model ensemble range encompasses the observations over less area than the CESM1-LE for all four model outputs of overall sea ice thickness, overall sea ice thickness change, thermodynamic sea ice thickness growth and dynamic sea ice thickness effects.

It is unclear how the process level deficiencies affect future sea ice conditions projected by the three climate model datasets, but it is likely that adjustments to the parameterization of the dynamic component of the sea ice models is required. Further work investigating the causes of these deficiencies and investigation of the trends in thermodynamic sea ice thickness growth and dynamic sea ice thickness effects is warranted.

Chapter 6

Conclusion

Sea ice thickness is changed through two primary mechanisms. Sea ice can change in thickness due to phase change, either from liquid to solid via freezing or solid to liquid via melting, in what are considered thermodynamic processes. Likewise, sea ice thickness can change when parcels move or their relative motion converges or divergences, altering the thickness at a given location. A governing equation that includes both of these processes is:

$$\frac{\partial H}{\partial t} = f(t, H, \mathbf{x}) - \nabla \cdot (\mathbf{u}H), \tag{6.1}$$

where H is plane slab sea ice thickness, t is time, f is a function of time, thickness and position vector $\mathbf{x}$ describing thermodynamic sea ice thickness increase, and $\mathbf{u}$ is the ice motion vector. The second term on the right hand side of Eq. 6.1 captures dynamic thickness changes, including both advection and deformation of sea ice. In other words, sea ice thickness

change at a given time is the sum of thermodynamic sea ice thickness change and dynamic sea ice thickness effects. A similar equation, applied to a sea ice thickness distribution rather than slab thickness, is found in Thorndike et al. (1975) and forms the basis for contemporary sea ice modelling. These two terms and affects are affected by differing mechanisms in a changing climate so independent observations of the two terms are required for accurate validation of models. Datasets of these observations and likewise any comparison between them and models are lacking. In this work, I present the first set of large scale observational estimates of these terms utilizing a novel retrieval of thermodynamic sea ice thickness growth and a comparison between these observations and models.

The novel sea ice thermodynamic thickness growth retrieval is called Stefan's Law Integrated Conducted Energy (SLICE) and it is made possible by new methods for observing snow–ice interface temperature using passive microwave brightness temperatures from the AMSR-E and AMSR2 instruments (Kilic et al., 2019). SLICE links observed satellite retrieved snow–ice interface temperatures to a simple model for sea ice thermodynamics called Stefan's Law (Stefan, 1891; Lepparanta, 1993). Stefan's Law relates latent heat of fusion conducted through the ice, calculated using the retrieved snow–ice interface temperature and a parameterized sea water freezing temperature, to a rate of sea ice accretion. SLICE is an effective retrieval of thermodynamic growth rate with a bias of 4 x 10^{-4} md^{-1} when compared with an ice mass balance buoy dataset.

The SLICE thermodynamic sea ice growth retrieval methodology was then utilized to present the first basin-wide, Eulerian, sub-seasonal temporal resolution, and long-term estimation

of dynamics effect on sea ice thickness, thermodynamic sea ice thickness growth, advection effect on sea ice thickness and deformation effect on sea ice thickness. Per Eq. 6.1, the difference between thermodynamic growth and overall sea ice thickness growth calculated from a satellite altimeter and passive microwave combination sea ice thickness product (Ricker et al., 2017b) was determined in order to estimate wintertime, basin-wide weekly sea ice dynamic effects as their residual difference on a spatial and temporal scale beyond the localized and seasonal studies available to date. We also separated the overall dynamic effect into its Eulerian, independent component effects of advection and deformation using a sea ice motion product (Tschudi et al., 2020).

Following the expected pattern of growth rate inversely related to sea ice thickness per Eq. 3.8, thermodynamic growth is lowest in the central Arctic where the thickest ice is found and highest in the seasonal ice zones where the thinnest ice is found. The highest positive dynamic effects are found where the Transpolar Drift and Beaufort Gyre deposit ice, north of the Canadian Arctic Archipelago. Where the Transpolar Drift originates, dynamic effects on sea ice thickness are negative. Couplets of opposite sign deformation and advection effect fields are common across the Arctic: positive advection effects and negative deformation effects of similar magnitude are found in the Beaufort Sea, while most other regions exhibit negative advection effects and positive deformation effects. The seasonal cycle of the various sea ice thickness processes shows an increasing positive deformation thickness effect and overall dynamic thickness effect as the winter season progresses, likely due to increasing ice thickness resisting lead formation and making more ice volume available for ridging. Results

from the winter of 2019-2020 compare well with Lagrangian dynamic and thermodynamic effects on sea ice thickness along the Multidisciplinary drifting Observatory for the Study of Arctic Climate (MOSAiC) drift track. The results show Lagrangian dynamics accounting for 47.2 % of growth in the grid cells nearest the drifting study area during this time period, while (Koo et al., 2021) found results of 42.6 % over a similar spatial scale.

These observational estimates of thermodynamic sea ice thickness growth and dynamic sea ice thickness effects were then compared to global climate models and a sea ice model reanalysis product. The model datasets, CESM1-LE, CESM2-LE, CESM2 OMIP2 and PIOMAS, all show a similar pattern of differences to the observations, characterized by underestimated dynamic sea ice thickness increase and overestimated thermodynamic sea ice thickness growth in the central Arctic, and vice versa in the regions where the Transpolar Drift originates and the Chukchi, Barents and Kara Seas. As these patterns are opposite phase, mirror images of one another, they sum to an overall sea ice thickness change and overall sea ice thickness that more closely match observations than the thermodynamic and dynamic processes themselves. All four model simulations are built upon the same fundamental principals and Eq. 6.1, so the similarity in results across them is not surprising. It is likely that the dynamic components and parameterizations within these models will need adjustments to account for these differences we have shown. Adjustment of these models to more closely match observations will improve accuracy of future projections of sea ice conditions.

There are many potential next steps to take in order to continue this line of inquiry. With

the observational datasets, further interrogation of the patterns for any connections to atmospheric and oceanic conditions comes to mind. In particular, it is reasonable to consider whether the dynamic patterns show any relation to the Arctic Oscillation or other climate modes. Additionally, identification of any trends over time in the observed dynamic effects would be worthwhile for projecting future climate. A longer dataset, perhaps utilizing a longer term overall sea ice thickness dataset constructed using passive microwave observed brightness temperatures, would be instrumental for this investigation and is in consideration. The model comparison work begun herein has myriad potential science leads. From an observational perspective, the sea ice motion with the models could be compared to that observed in the ice motion vector dataset utilized here in order to determine what role ice motion plays in the model differences from observations. From a modelling perspective, there are likely a number of parameterizations within the dynamic and thermodynamic components of the sea ice models and within the underlying ocean models that could be adjusted and the resultant changes to the observational comparisons reported. If a longer term dataset of thermodynamic and dynamic effects were to be successfully created, comparison of trends within this dataset to those found in the model would also be a very valuable exercise. All of these next steps are towards to goal of improving the sea ice components of global climate models and therefore the projections from global climate models at large.

Appendix A

Chapter 3 supplemental material
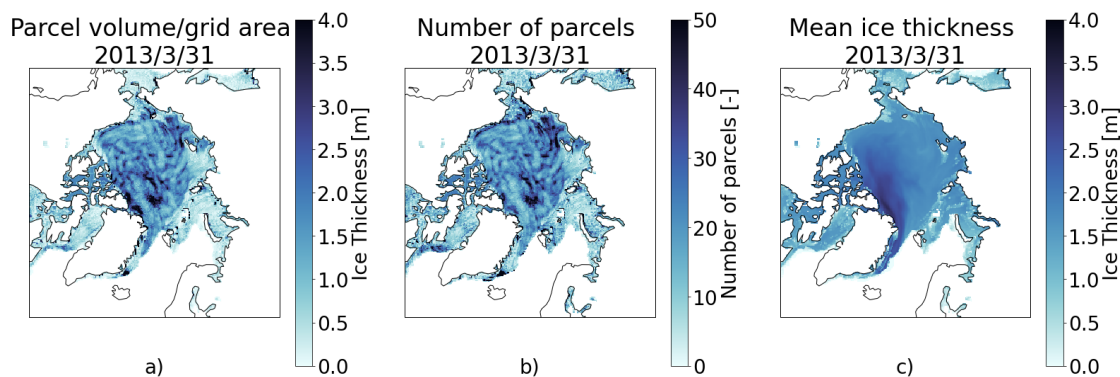
FIGURE A.1: SLICE parcels on March 31, 2013 (a) regridded using total parcel volume per grid cell divided by grid area, (b) counts within grid cell and (c) regridded mean parcel thickness within each grid cell. The volume per grid cell approach is unrealistic and dominated by erroneous convergence and divergence of parcels within grid cells.
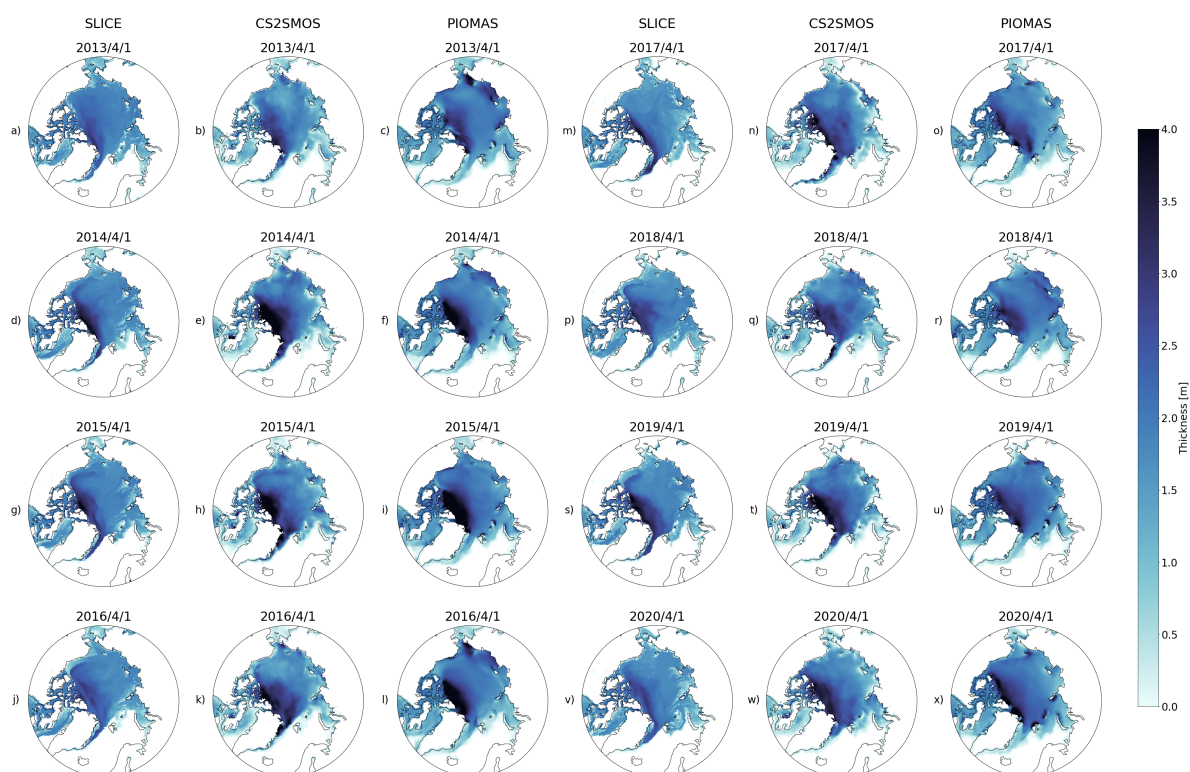
FIGURE A.2: For the sea ice growth seasons ending in a–c) 2013, d–f) 2014, g–i) 2015, j–l) 2016, m–o) 2017, p–r) 2018, s–u) 2019 and v–x) 2020, a, d, g, j, m, p, s, v) SLICE sea ice thickness for 1 April, c, f, i, l, o, r, u, x) AWI CS2SMOS sea ice thickness from 1 April and b, e, h, k, n, q, t, w) PIOMAS sea ice thickness from 1 April.

Appendix B

Chapter 4 supplemental material
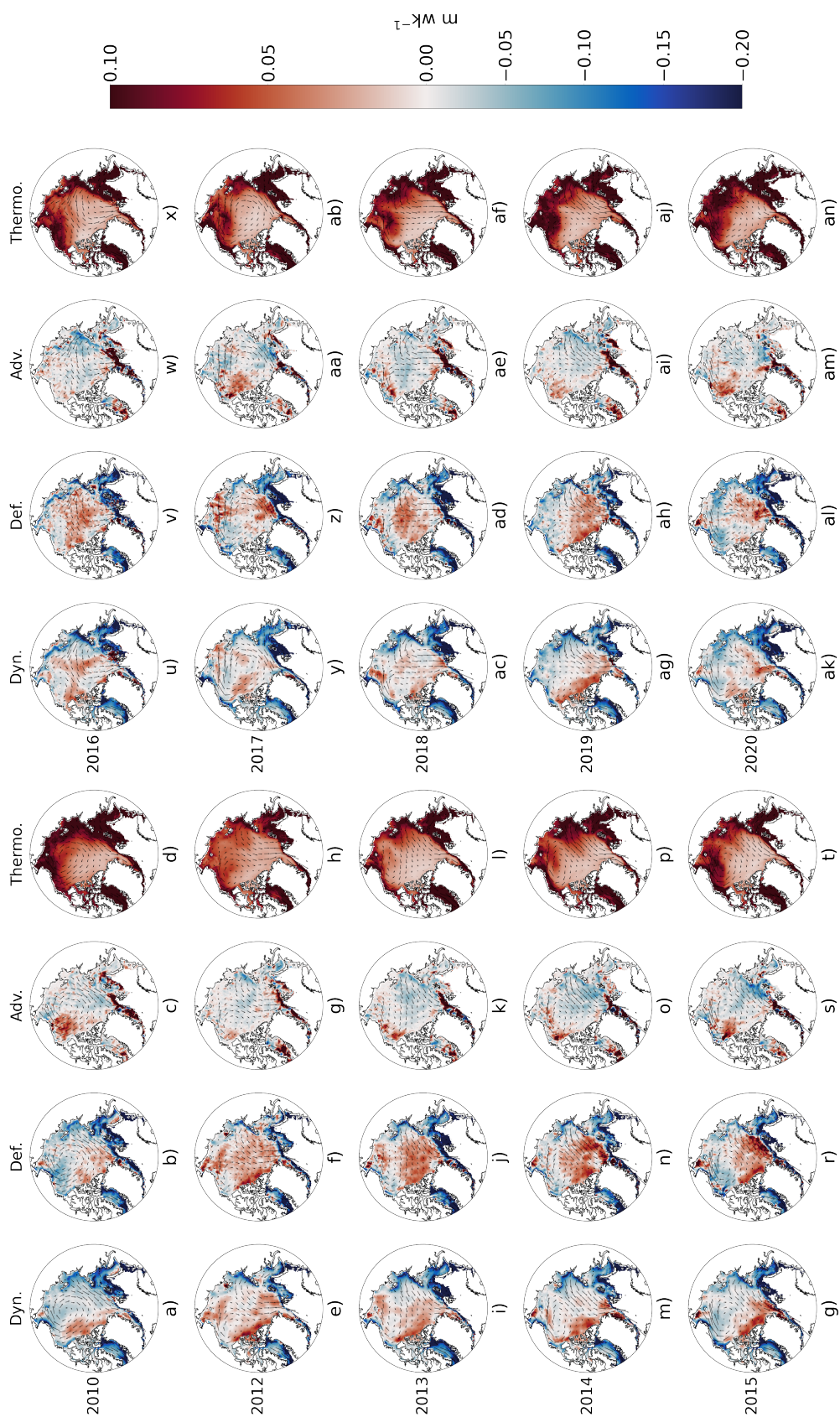
FIGURE B.1: Mean dynamic, deformation, advection and thermodynamic effects for the winters beginning in 2010-2020 except 2011 with yearly mean ice motion vectors plotted. The patterns of dynamic, advective and deformation effects broadly follow the ice motion vectors.

Bibliography

Alexander, M. A., J. D. Scott, K. D. Friedland, K. E. Mills, J. A. Nye, A. J. Pershing, and A. C. Thomas, 2018: Projected sea surface temperatures over the 21st century: Changes in the mean, variability and extremes for large marine ecosystem regions of Northern Oceans. *Elementa-Science of the Anthropocene*, **6**, doi:10.1525/elementa.191.

Alexandrov, V., S. Sandven, J. Wahlin, , and O. M. Johannessen, 2010: The relation between sea ice thickness and freeboard in the Arctic. *Cryosphere*, **4**, 373–380, doi:10.5194/tc-4-373-2010.

Arthun, M., I. H. Onarheim, J. Dorr, and T. Eldevik, 2021: The seasonal and regional transition to an ice-free Arctic. *Geophysical Research Letters*, **48**, doi:10.1029/2020gl090825.

Arzel, O., T. Fichefet, and H. Goosse, 2006: Sea ice evolution over the 20th and 21st centuries as simulated by current AOGCMs. *Ocean Modelling*, **12**, 401–415, doi:10.1016/j.ocemod.2005.08.002.

Bailey, E., D. L. Feltham, and P. R. Sammonds, 2010: A model for the consolidation of rafted sea ice. *J. Geophys. Res.-Oceans*, **115**, C04015, doi:10.1029/2008jc005103.

Batrak, Y., E. Kourzeneva, and M. Homleid, 2018: Implementation of a simple thermo-dynamic sea ice scheme, SICE version 1.0-38h1, within the ALADIN-HIRLAM numerical weather prediction system version 38h1. *Geoscientific Model Development*, **11**, 3347–3368, doi:10.5194/gmd-11-3347-2018.

Bekryaev, R. V., I. V. Polyakov, and V. A. Alexeev, 2010: Role of polar amplification in long-term surface air temperature variations and modern Arctic warming. *Journal of Climate*, **23**, 3888–3906, doi:10.1175/2010jcli3297.1.

Bitz, C. M. and W. H. Lipscomb, 1999: An energy-conserving thermodynamic model of sea ice. *Journal of Geophysical Research-Oceans*, **104**, 15669–15677, doi:10.1029/1999jc900100.

Bitz, C. M. and G. H. Roe, 2004: A mechanism for the high rate of sea ice thinning in the Arctic Ocean. *J. Climate*, **17**, 3623–3632, doi:10.1175/1520-0442(2004)017<3623:amfthr>2.0.co;2.

Bjork, G. and J. Soderkvist, 2002: Dependence of the Arctic Ocean ice thickness distribution on the poleward energy flux in the atmosphere. *Journal of Geophysical Research-Oceans*, **107**, doi:10.1029/2000jc000723.

Boe, J. L., A. Hall, and X. Qu, 2009: September sea-ice cover in the Arctic Ocean projected to vanish by 2100. *Nature Geoscience*, **2**, 341–343, doi:10.1038/ngeo467.

Box, J. E., W. T. Colgan, T. R. Christensen, N. M. Schmidt, M. Lund, F. J. W. Parmentier, R. Brown, U. S. Bhatt, E. S. Euskirchen, V. E. Romanovsky, J. E. Walsh, J. E. Overland,

M. Y. Wang, R. W. Corell, W. N. Meier, B. Wouters, S. Mernild, J. Mard, J. Pawlak, and M. S. Olsen, 2019: Key indicators of Arctic climate change: 1971-2017. *Environmental Research Letters*, **14**, doi:10.1088/1748-9326/aafc1b.

Cavalieri, D. J., P. Gloersen, and W. J. Campbell, 1984: Determination of sea ice parameters with the Nimbus-7 SMMR. *J. Geophys. Res.-Atmos.*, **89**, 5355–5369, doi:10.1029/JD089iD04p05355.

Cavalieri, D. J., T. Markus, and J. C. Comiso, 2014: AMSR-E/Aqua daily L3 25 km brightness temperature & sea ice concentration polar grids, version 3. *Boulder, Colorado USA. NASA National Snow and Ice Data Center Distributed Active Archive Center [data set]*, doi:10.5067/AMSR-E/AE_SI25.003.

Comiso, J. C., 2009: Enhanced sea ice concentrations and ice extents from AMSR-E data. *Journal of The Remote Sensing Society of Japan*, **29**, 199–215, doi:10.11440/rssj.29.199.

Connor, L. N., S. W. Laxon, A. L. Ridout, W. B. Krabill, and D. C. McAdoo, 2009: Comparison of Envisat radar and airborne laser altimeter measurements over Arctic sea ice. *Remote Sens. Environ.*, **113**, 563–570, doi:10.1016/j.rse.2008.10.015.

Coon, M. D., G. A. Maykut, R. S. Pritchard, D. A. Rothrock, and A. S. Thorndike, 1974: Modeling the pack ice as an elastic-plastic material. *AIDJEX Bulletin*, **24**, 1–105.

Cox, G. F. N. and W. F. Weeks, 1988: Numerical simulations of the profile properties of undeformed 1st-year sea ice during the growth season. *Journal of Geophysical Research-Oceans*, **93**, 12449–12460, doi:10.1029/JC093iC10p12449.

Dalaiden, Q., H. Goosse, J. T. M. Lenaerts, M. G. P. Cavitte, and N. Henderson, 2020: Future Antarctic snow accumulation trend is dominated by atmospheric synoptic-scale events. *Communications Earth & Environment*, **1**, doi:10.1038/s43247-020-00062-x.

Danabasoglu, G., S. C. Bates, B. P. Briegleb, S. R. Jayne, M. Jochum, W. G. Large, S. Peacock, and S. G. Yeager, 2012: The CCSM4 ocean component. *Journal of Climate*, **25**, 1361–1389, doi:10.1175/jcli-d-11-00091.1.

Danabasoglu, G., J. F. Lamarque, J. Bacmeister, D. A. Bailey, A. K. DuVivier, J. Edwards, L. K. Emmons, J. Fasullo, R. Garcia, A. Gettelman, C. Hannay, M. M. Holland, W. G. Large, P. H. Lauritzen, D. M. Lawrence, J. T. M. Lenaerts, K. Lindsay, W. H. Lipscomb, M. J. Mills, R. Neale, K. W. Oleson, B. Otto-Bliesner, A. S. Phillips, W. Sacks, S. Tilmes, L. van Kampenhout, M. Vertenstein, A. Bertini, J. Dennis, C. Deser, C. Fischer, B. Fox-Kemper, J. E. Kay, D. Kinnison, P. J. Kushner, V. E. Larson, M. C. Long, S. Mickelson, J. K. Moore, E. Nienhouse, L. Polvani, P. J. Rasch, and W. G. Strand, 2020: The Community Earth System Model version 2 (CESM2). *Journal of Advances in Modeling Earth Systems*, **12**, doi:10.1029/2019ms001916.

DeRepentigny, P., A. Jahn, M. M. Holland, and A. Smith, 2020: Arctic sea ice in two configurations of the CESM2 during the 20th and 21st centuries. *Journal of Geophysical Research-Oceans*, **125**, doi:10.1029/2020jc016133.

DeRepentigny, P., L. B. Tremblay, R. Newton, and S. Pfirman, 2016: Patterns of sea ice retreat in the transition to a seasonally ice-free Arctic. *J. Climate*, **29**, 6993 – 7008, doi:10.1175/JCLI-D-15-0733.1.

Docquier, D. and T. Koenigk, 2021: Observation-based selection of climate models projects Arctic ice-free summers around 2035. *Nature Communications Earth & Environment*, **2**, 144, doi:10.1038/s43247-021-00214-7.

Dukowicz, J. K. and J. R. Baumgardner, 2000: Incremental remapping as a transport/advection algorithm. *Journal of Computational Physics*, **160**, 318–335, doi:10.1006/jcph.2000.6465.

DuVivier, A. K., M. M. Holland, J. E. Kay, S. Tilmes, A. Gettelman, and D. A. Bailey, 2020: Arctic and Antarctic sea ice mean state in the Community Earth System Model version 2 and the influence of atmospheric chemistry. *Journal of Geophysical Research-Oceans*, **125**, doi:10.1029/2019jc015934.

Eisenman, I., 2012: Factors controlling the bifurcation structure of sea ice retreat. *Journal of Geophysical Research-Atmospheres*, **117**, doi:10.1029/2011jd016164.

Eisenman, I. and J. S. Wettlaufer, 2009: Nonlinear threshold behavior during the loss of Arctic sea ice. *Proceedings of the National Academy of Sciences of the United States of America*, **106**, 28–32, doi:10.1073/pnas.0806887106.

Eyring, V., S. Bony, G. A. Meehl, C. A. Senior, B. Stevens, R. J. Stouffer, and K. E. Taylor, 2016: Overview of the coupled model intercomparison project phase 6 (CMIP6) experimental design and organization. *Geoscientific Model Development*, **9**, 1937–1958, doi:10.5194/gmd-9-1937-2016.

Feltham, D. L., N. Untersteiner, J. S. Wettlaufer, and M. G. Worster, 2006: Sea ice is a mushy layer. *Geophysical Research Letters*, **33**, L14501, doi:10.1029/2006gl026290.

Flato, G. and Participating CMIP Modelling Groups, 2004: Sea-ice and its response to CO2 forcing as simulated by global climate models. *Climate Dynamics*, **23**, 229–241, doi:10.1007/s00382-004-0436-7.

Ford, B., M. V. Martin, S. E. Zelasky, E. V. Fischer, S. C. Anenberg, C. L. Heald, and J. R. Pierce, 2018: Future fire impacts on smoke concentrations, visibility, and health in the contiguous United States. *Geohealth*, **2**, 229–247, doi:10.1029/2018gh000144.

Gloersen, P. and D. J. Cavalieri, 1986: Reduction of weather effects in the calculation of sea ice concentration from microwave radiances. *J. Geophys. Res.-Oceans*, **91**, 3913–3919, doi:10.1029/JC091iC03p03913.

Guerreiro, K., S. Fleury, E. Zakharova, A. Kouraev, F. Remy, and P. Maisongrande, 2017: Comparison of CryoSat-2 and Envisat radar freeboard over Arctic sea ice: Toward an improved Envisat freeboard retrieval. *Cryosphere*, **11**, 2059–2073, doi:10.5194/tc-11-2059-2017.

Hendricks, S., S. Paul, and E. Rinne, 2018: ESA Sea Ice Climate Change Initiative (Sea_Ice_cci): Northern Hemisphere sea ice thickness from the CryoSat-2 satellite on a monthly grid (L3C), v2.0. Centre for Environmental Data Analysis. doi:10.5285/ff79d140824f42dd92b204b4f1e9e7c2.

Hendricks, S. and R. Ricker, 2020: Product user guide & algorithm specification: AWI CryoSat-2 sea ice thickness (version 2.3). doi:10013/epic.ecd56b5d-3e7d-4a65-9019-588b1c3b0d26.

Hibler, W. D., 1979: Dynamic thermodynamic sea ice model. *J Phys. Oceanogr.*, **9**, 815–846, doi:10.1175/1520-0485(1979)009<0815:adtsim>2.0.co;2.

— 1980: Modeling a variable thickness sea ice cover. *Monthly Weather Review*, **108**, 1943–1973, doi:10.1175/1520-0493(1980)108<1943:mavtsi>2.0.co;2.

Hoffman, J. P., S. A. Ackerman, Y. H. Liu, and J. R. Key, 2019: The detection and characterization of Arctic sea ice leads with satellite imagers. *Remote Sensing*, **11**, doi:10.3390/rs11050521.

Holland, M. M., M. C. Serreze, and J. Stroeve, 2010: The sea ice mass budget of the Arctic and its future change as simulated by coupled climate models. *Climate Dynamics*, **34**, 185–200, doi:10.1007/s00382-008-0493-4.

Hunke, E. and H. Lipscomb, 2010: CICE: the Los Alamos sea ice model documentation and software user's manual, version 4.1, LA-CC-06-012. `https://csdms.colorado.edu/w/images/CICE_documentation_and_software_user%27s_manual.pdf` (last access: 19 oct 2022).

Hunke, E. C. and J. K. Dukowicz, 1997: An elastic-viscous-plastic model for sea ice dynamics. *Journal of Physical Oceanography*, **27**, 1849–1867, doi:10.1175/1520-0485(1997)027<1849:aevpmf>2.0.co;2.

— 2002: The elastic-viscous-plastic sea ice dynamics model in general orthogonal curvilinear coordinates on a sphere-incorporation of metric terms. *Monthly Weather Review*, **130**, 1848–1865, doi:10.1175/1520-0493(2002)130<1848:tevpsi>2.0.co;2.

Hunke, E. C., D. A. Hebert, and O. Lecomte, 2013: Level-ice melt ponds in the Los Alamos sea ice model, CICE. *Ocean Modelling*, **71**, 26–42, doi:10.1016/j.ocemod.2012.11.008.

Hunke, E. C., W. H. Lipscomb, A. K. Turner, N. Jeffery, and S. Elliott, 2015: CICE: the Los Alamos sea ice model documentation and software user's manual version 5.1, LA-CC-06-012. `http://www.ccpo.odu.edu/~klinck/Reprints/PDF/cicedoc2015.pdf` (last access: 19 oct 2022).

Hurrell, J. W., M. M. Holland, P. R. Gent, S. Ghan, J. E. Kay, P. J. Kushner, J. F. Lamarque, W. G. Large, D. Lawrence, K. Lindsay, W. H. Lipscomb, M. C. Long, N. Mahowald, D. R. Marsh, R. B. Neale, P. Rasch, S. Vavrus, M. Vertenstein, D. Bader, W. D. Collins, J. J. Hack, J. Kiehl, and S. Marshall, 2013: The Community Earth System Model a framework for collaborative research. *Bulletin of the American Meteorological Society*, **94**, 1339–1360, doi:10.1175/bams-d-12-00121.1.

Itkin, P., G. Spreen, S. M. Hvidegaard, H. Skourup, J. Wilkinson, S. Gerland, and M. A. Granskog, 2018: Contribution of deformation to sea ice mass balance: A case study from an N-ICE2015 storm. *Geophysical Research Letters*, **45**, 789–796, doi:10.1002/2017gl076056.

Jenkins, M. and A. G. Dai, 2021: The impact of sea-ice loss on Arctic climate feedbacks and their role for Arctic amplification. *Geophysical Research Letters*, **48**, doi:10.1029/2021gl094599.

Kang, E. J., B. J. Sohn, R. T. Tonboe, G. Dybkjaer, K. Holmlund, J. M. Kim, and C. Liu, 2021: Implementation of a 1-d thermodynamic model for simulating the winter-time evolvement of physical properties of snow and ice over the Arctic Ocean. *J. Adv. Model. Earth Sy.*, **13**, 3, doi:10.1029/2020ms002448.

Kay, J. E., C. Deser, A. Phillips, A. Mai, C. Hannay, G. Strand, J. M. Arblaster, S. C. Bates, G. Danabasoglu, J. Edwards, M. Holland, P. Kushner, J. F. Lamarque, D. Lawrence, K. Lindsay, A. Middleton, E. Munoz, R. Neale, K. Oleson, L. Polvani, and M. Vertenstein, 2015: The Community Earth System Model (CESM) Large Ensemble project: A community resource for studying climate change in the presence of internal climate variability. *Bulletin of the American Meteorological Society*, **96**, 1333–1349, doi:10.1175/bams-d-13-00255.1.

Keen, A., E. Blockley, D. A. Bailey, J. B. Debernard, M. Bushuk, S. Delhaye, D. Docquier, D. Feltham, F. Massonnet, S. O'Farrell, L. Ponsoni, J. M. Rodriguez, D. Schroeder, N. Swart, T. Toyoda, H. Tsujino, M. Vancoppenolle, and K. Wyser, 2021: An intercomparison of the mass budget of the Arctic sea ice in CMIP6 models. *Cryosphere*, **15**, 951–982, doi:10.5194/tc-15-951-2021.

Key, J., X. J. Wang, Y. H. Liu, R. Dworak, and A. Letterly, 2016: The AVHRR Polar Pathfinder climate data records. *Remote Sensing*, **8**, 3, doi:10.3390/rs8030167.

Kilic, L., R. T. Tonboe, C. Prigent, and G. Heygster, 2019: Estimating the snow depth, the snow–ice interface temperature, and the effective temperature of Arctic sea ice using Advanced Microwave Scanning Radiometer 2 and ice mass balance buoy data. *Cryosphere*, **13**, 1283–1296, doi:10.5194/tc-13-1283-2019.

Knutti, R., D. Masson, and A. Gettelman, 2013: Climate model genealogy: Generation CMIP5 and how we got there. *Geophysical Research Letters*, **40**, 1194–1199, doi:10.1002/grl.50256.

Kobayashi, S., Y. Ota, Y. Harada, A. Ebita, M. Moriya, H. Onoda, K. Onogi, H. Kamahori, C. Kobayashi, H. Endo, K. Miyaoka, and K. Takahashi, 2015: The JRA-55 reanalysis: General specifications and basic characteristics. *Journal of the Meteorological Society of Japan*, **93**, 5–48, doi:10.2151/jmsj.2015-001.

Koo, Y., R. B. Lei, Y. B. Cheng, B. Cheng, H. J. Xie, M. Hoppmann, N. T. Kurtz, S. F. Ackley, and A. M. Mestas-Nunez, 2021: Estimation of thermodynamic and dynamic contributions to sea ice growth in the Central Arctic using ICESat-2 and MOSAiC SIMBA buoy data. *Remote Sensing of Environment*, **267**, doi:10.1016/j.rse.2021.112730.

Krabill, W. B., R. H. Thomas, C. F. Martin, R. N. Swift, and E. B. Frederick, 1995: Accuracy of airborne laser altimetry over the Greenland ice-sheet. *International Journal of Remote Sensing*, **16**, 1211–1222, doi:10.1080/01431169508954472.

Kurtz, N., M. Studinger, J. Harbeck, V. Onana, and D. Yi., 2015: IceBridge L4 sea ice freeboard, snow depth, and thickness, version 1. *Boulder, Colorado USA. NASA*

National Snow and Ice Data Center Distributed Active Archive Center [data set], doi:10.5067/G519SHCKWQV6.

— 2016: IceBridge sea ice freeboard, snow depth, and thickness quick look, version 1. *Boulder, Colorado USA. NASA National Snow and Ice Data Center Distributed Active Archive Center [data set]*, doi:10.5067/GRIXZ91DE0L9.

Kurtz, N. T., S. L. Farrell, M. Studinger, N. Galin, J. P. Harbeck, R. Lindsay, V. D. Onana, B. Panzer, and J. G. Sonntag, 2013: Sea ice thickness, freeboard, and snow depth products from Operation IceBridge airborne data. *Cryosphere*, **7**, 1035–1056, doi:10.5194/tc-7-1035-2013.

Kurtz, N. T., N. Galin, and M. Studinger, 2014a: An improved CryoSat-2 sea ice freeboard retrieval algorithm through the use of waveform fitting. *Cryosphere*, **8**, 1217–1237, doi:10.5194/tc-8-1217-2014.

— 2014b: An improved CryoSat-2 sea ice freeboard retrieval algorithm through the use of waveform fitting. *Cryosphere*, **8**, 1217–1237, doi:10.5194/tc-8-1217-2014.

Kwok, R., 2006: Contrasts in sea ice deformation and production in the Arctic seasonal and perennial ice zones. *Journal of Geophysical Research-Oceans*, **111**, doi:10.1029/2005jc003246.

Kwok, R. and G. F. Cunningham, 2008: ICESat over Arctic sea ice: Estimation of snow depth and ice thickness. *J. Geophys. Res.-Oceans*, **113**, C08010, doi:10.1029/2008jc004753.

— 2015: Variability of Arctic sea ice thickness and volume from CryoSat-2. *Philos. T. Roy. Soc. A*, **373**, 2045, doi:10.1098/rsta.2014.0157.

— 2016: Contributions of growth and deformation to monthly variability in sea ice thickness north of the coasts of Greenland and the Canadian Arctic Archipelago. *Geophysical Research Letters*, **43**, 8097–8105, doi:10.1002/2016gl069333.

Kwok, R., S. Kacimi, M. A. Webster, N. T. Kurtz, and A. A. Petty, 2020: Arctic snow depth and sea ice thickness from ICESat-2 and CryoSat-2 freeboards: A first examination. *J Geophys Res-Oceans*, **125**, doi:10.1029/2019jc016008.

Kwok, R., N. T. Kurtz, L. Brucker, A. Ivanoff, T. Newman, S. L. Farrell, J. King, S. Howell, M. A. Webster, J. Paden, C. Leuschen, J. A. MacGregor, J. Richter-Menge, J. Harbeck, and M. Tschudi, 2017: Intercomparison of snow depth retrievals over Arctic sea ice from radar data acquired by Operation IceBridge. *Cryosphere*, **11**, 2571–2593, doi:10.5194/tc-11-2571-2017.

Kwok, R. and D. A. Rothrock, 2009: Decline in Arctic sea ice thickness from submarine and ICESat records: 1958–2008. *Geophys. Res. Lett.*, **36**, doi:10.1029/2009GL039035.

Lamarque, J. F., T. C. Bond, V. Eyring, C. Granier, A. Heil, Z. Klimont, D. Lee, C. Liousse, A. Mieville, B. Owen, M. G. Schultz, D. Shindell, S. J. Smith, E. Stehfest, J. Van Aardenne, O. R. Cooper, M. Kainuma, N. Mahowald, J. R. McConnell, V. Naik, K. Riahi, and D. P. van Vuuren, 2010: Historical (1850-2000) gridded anthropogenic and biomass burning emissions of reactive gases and aerosols: methodology and application. *Atmospheric Chemistry and Physics*, **10**, 7017–7039, doi:10.5194/acp-10-7017-2010.

Lavergne, T., A. M. Surensen, S. Kern, R. Tonboe, D. Notz, S. Aaboe, L. Bell, G. Dybkjaer, S. Eastwood, C. Gabarro, G. Heygster, M. A. Killie, M. B. Kreiner, J. Lavelle, R. Saldo, S. Sandven, and L. T. Pedersen, 2019: Version 2 of the EUMETSAT OSI SAF and ESA CCI sea-ice concentration climate data records. *Cryosphere*, **13**, 49–78, doi:10.5194/tc-13-49-2019.

Laxon, S. W., K. A. Giles, A. L. Ridout, D. J. Wingham, R. Willatt, R. Cullen, R. Kwok, A. Schweiger, J. L. Zhang, C. Haas, S. Hendricks, R. Krishfield, N. Kurtz, S. Farrell, and M. Davidson, 2013: Cryosat-2 estimates of Arctic sea ice thickness and volume. *Geophys. Res. Lett.*, **40**, 732–737, doi:10.1002/grl.50193.

Lebrun, M., M. Vancoppenolle, G. Madec, and F. Massonnet, 2019: Arctic sea-ice-free season projected to extend into autumn. *Cryosphere*, **13**, 79–96, doi:10.5194/tc-13-79-2019.

Lee, S. M. and B. J. Sohn, 2015: Retrieving the refractive index, emissivity, and surface temperature of polar sea ice from 6.9GHz microwave measurements: A theoretical development. *J. Geophys. Res.-Atmos.*, **120**, 2293–2305, doi:10.1002/2014jd022481.

Lee, S. M., B. J. Sohn, and C. D. Kummerow, 2018: Long-term Arctic snow/ice interface temperature from special sensor for microwave imager measurements. *Remote Sensing*, **10**, 11, doi:10.3390/rs10111795.

Lehner, F., S. Coats, T. F. Stocker, A. G. Pendergrass, B. M. Sanderson, C. C. Raible, and J. E. Smerdon, 2017: Projected drought risk in 1.5 degrees C and 2 degrees C warmer climates. *Geophysical Research Letters*, **44**, 7419–7428, doi:10.1002/2017gl074117.

Lei, R. B., N. Li, P. Heil, B. Cheng, Z. H. Zhang, and B. Sun, 2014: Multiyear sea ice thermal regimes and oceanic heat flux derived from an ice mass balance buoy in the Arctic Ocean. *Journal of Geophysical Research-Oceans*, **119**, 537–547, doi:10.1002/2012jc008731.

Lepparanta, M., 1993: A review of analytical models of sea–ice growth. *Atmos. Ocean*, **31**, 123–138, doi:10.1080/07055900.1993.9649465.

Lipscomb, W. H., 2001: Remapping the thickness distribution in sea ice models. *Journal of Geophysical Research-Oceans*, **106**, 13989–14000, doi:10.1029/2000jc000518.

Liu, Y. H., J. Key, and R. Mahoney, 2016: Sea and freshwater ice concentration from VIIRS on Suomi NPP and the future JPSS satellites. *Remote Sensing*, **8**, 6, doi:10.3390/rs8060523.

Liu, Y. H., J. R. Key, and X. J. Wang, 2009: Influence of changes in sea ice concentration and cloud cover on recent Arctic surface temperature trends. *Geophys. Res. Lett.*, **36**, L20710, doi:10.1029/2009gl040708.

Liu, Y. H., J. R. Key, X. J. Wang, and M. Tschudi, 2020: Multidecadal Arctic sea ice thickness and volume derived from ice age. *Cryosphere*, **14**, 1325–1345, doi:10.5194/tc-14-1325-2020.

Lorenz, E. N., 1963: Deterministic nonperiodic flow. *Journal of the Atmospheric Sciences*, **20**, 130–141, doi:10.1175/1520-0469(1963)020<0130:dnf>2.0.co;2.

Manabe, S., R. J. Stouffer, M. J. Spelman, and K. Bryan, 1991: Transient responses of a coupled ocean atmosphere model to gradual changes of atmospheric

CO2 .1. annual mean response. *Journal of Climate*, **4**, 785–818, doi:10.1175/1520-0442(1991)004<0785:troaco>2.0.co;2.

Markus, T. and D. J. Cavalieri, 2000: An enhancement of the NASA Team sea ice algorithm. *IEEE T. Geosci. Remote.*, **38**, 1387–1398, doi:10.1109/36.843033.

— 2009: The AMSR-E NT2 sea ice concentration algorithm: its basis and implementation. *Journal of The Remote Sensing Society of Japan*, **29**, 216–225, doi:10.11440/rssj.29.216.

Markus, T., J. C. Comiso, and W. N. Meier, 2018: AMSR-E/AMSR2 unified L3 daily 25 km brightness temperatures & sea ice concentration polar grids, version 1. *Boulder, Colorado USA. NASA National Snow and Ice Data Center Distributed Active Archive Center [data set]*, doi:10.5067/TRUIAL3WPAUP.

Markus, T., T. Neumann, A. Martino, W. Abdalati, K. Brunt, B. Csatho, S. Farrell, H. Fricker, A. Gardner, D. Harding, M. Jasinski, R. Kwok, L. Magruder, D. Lubin, S. Luthcke, J. Morison, R. Nelson, A. Neuenschwander, S. Palm, S. Popescu, C. K. Shum, B. E. Schutz, B. Smith, Y. K. Yang, and J. Zwally, 2017: The Ice, Cloud, and land Elevation Satellite-2 (ICESat-2): science requirements, concept, and implementation. *Remote Sens. Environ.*, **190**, 260–273, doi:10.1016/j.rse.2016.12.029.

Massonnet, F., T. Fichefet, H. Goosse, C. M. Bitz, G. Philippon-Berthier, M. M. Holland, and P. Y. Barriat, 2012: Constraining projections of summer Arctic sea ice. *Cryosphere*, **6**, 1383–1394, doi:10.5194/tc-6-1383-2012.

Massonnet, F., M. Vancoppenolle, H. Goosse, D. Docquier, T. Fichefet, and E. Blanchard-Wrigglesworth, 2018: Arctic sea–ice change tied to its mean state through thermodynamic processes. *Nat. Clim. Change*, **8**, 599–603, doi:10.1038/s41558-018-0204-z.

Mayer, M., S. Tietsche, L. Haimberger, T. Tsubouchi, J. Mayer, and H. Zuo, 2019: An improved estimate of the coupled Arctic energy budget. *J. Climate*, **32**, 7915–7934, doi:10.1175/jcli-d-19-0233.1.

Maykut, G. A. and N. Untersteiner, 1971: Some results from a time-dependent thermodynamic model of sea ice. *Journal of Geophysical Research*, **76**, 1550–1575, doi:10.1029/JC076i006p01550.

McPhee, M. G. and N. Untersteiner, 1982: Using sea ice to measure vertical heat-flux in the ocean. *Journal of Geophysical Research-Oceans*, **87**, 2071–2074, doi:10.1029/JC087iC03p02071.

Mecklenburg, S., M. Drusch, Y. H. Kerr, J. Font, M. Martin-Neira, S. Delwart, G. Buenadicha, N. Reul, E. Daganzo-Eusebio, R. Oliva, and R. Crapolicchio, 2012: ESA's Soil Moisture and Ocean Salinity Mission: Mission performance and operations. *IEEE T. Geosci. Remote.*, **50**, 1354–1366, doi:10.1109/tgrs.2012.2187666.

Meier, W. N., J. S. Stewart, Y. H. Liu, J. Key, and J. A. Miller, 2017: Operational implementation of sea ice concentration estimates from the AMSR2 sensor. *IEEE J. Sel. Top. Appl.*, **10**, 3904–3911, doi:10.1109/jstars.2017.2693120.

Meier, W. N., J. Stroeve, and F. Fetterer, 2007: Whither Arctic sea ice? A clear signal of decline regionally, seasonally and extending beyond the satellite record. *Annals of Glaciology, Vol 46, 2007*, **46**, 428–434, doi:10.3189/172756407782871170.

Meinshausen, M., S. J. Smith, K. Calvin, J. S. Daniel, M. L. T. Kainuma, J. F. Lamarque, K. Matsumoto, S. A. Montzka, S. C. B. Raper, K. Riahi, A. Thomson, G. J. M. Velders, and D. P. P. van Vuuren, 2011: The RCP greenhouse gas concentrations and their extensions from 1765 to 2300. *Climatic Change*, **109**, 213–241, doi:10.1007/s10584-011-0156-z.

Moore, J. K., K. Lindsay, S. C. Doney, M. C. Long, and K. Misumi, 2013: Marine ecosystem dynamics and biogeochemical cycling in the Community Earth System Model CESM1(BGC): Comparison of the 1990s with the 2090s under the RCP4.5 and RCP8.5 scenarios. *Journal of Climate*, **26**, 9291–9312, doi:10.1175/jcli-d-12-00566.1.

Muntjewerf, L., M. Petrini, M. Vizcaino, C. E. da Silva, R. Sellevold, M. D. W. Scherrenberg, K. Thayer-Calder, S. L. Bradley, J. T. M. Lenaerts, W. H. Lipscomb, and M. Lofverstrom, 2020: Greenland ice sheet contribution to 21st century sea level rise as simulated by the coupled CESM2.1-CISM2.1. *Geophysical Research Letters*, **47**, doi:10.1029/2019gl086836.

Nicolaus, M., D. K. Perovich, G. Spreen, M. A. Granskog, L. von Albedyll, M. Angelopoulos, P. Anhaus, S. Arndt, H. J. Belter, V. Bessonov, G. Birnbaum, J. Brauchle, R. Calmer, E. Cardellach, B. Cheng, D. Clemens-Sewall, R. Dadic, E. Damm, G. de Boer, O. Demir, K. Dethloff, D. V. Divine, A. A. Fong, S. Fons, M. M. Frey, N. Fuchs, C. Gabarró, S. Gerland, H. F. Goessling, R. Gradinger, J. Haapala, C. Haas, J. Hamilton, H.-R. Hannula, S. Hendricks, A. Herber, C. Heuzé, M. Hoppmann, K. V. Høyland, M. Huntemann,

J. K. Hutchings, B. Hwang, P. Itkin, H.-W. Jacobi, M. Jaggi, A. Jutila, L. Kaleschke, C. Katlein, N. Kolabutin, D. Krampe, S. S. Kristensen, T. Krumpen, N. Kurtz, A. Lampert, B. A. Lange, R. Lei, B. Light, F. Linhardt, G. E. Liston, B. Loose, A. R. Macfarlane, M. Mahmud, I. O. Matero, S. Maus, A. Morgenstern, R. Naderpour, V. Nandan, A. Niubom, M. Oggier, N. Oppelt, F. Pätzold, C. Perron, T. Petrovsky, R. Pirazzini, C. Polashenski, B. Rabe, I. A. Raphael, J. Regnery, M. Rex, R. Ricker, K. Riemann-Campe, A. Rinke, J. Rohde, E. Salganik, R. K. Scharien, M. Schiller, M. Schneebeli, M. Semmling, E. Shimanchuk, M. D. Shupe, M. M. Smith, V. Smolyanitsky, V. Sokolov, T. Stanton, J. Stroeve, L. Thielke, A. Timofeeva, R. T. Tonboe, A. Tavri, M. Tsamados, D. N. Wagner, D. Watkins, M. Webster, and M. Wendisch, 2022: Overview of the MOSAiC expedition: Snow and sea ice. *Elementa: Science of the Anthropocene*, **10**, doi:10.1525/elementa.2021.000046.

Notz, D., 2005: Thermodynamic and fluid-dynamical processes in sea ice. *Ph.D. thesis, Cambridge University*.

Notz, D., J. Dorr, D. A. Bailey, E. Blockley, M. Bushuk, J. B. Debernard, E. Dekker, P. DeRepentigny, D. Docquier, N. S. Fuckar, J. C. Fyfe, A. Jahn, M. Holland, E. Hunke, D. Iovino, N. Khosravi, G. Madec, F. Massonnet, S. O'Farrell, A. Petty, A. Rana, L. Roach, E. Rosenblum, C. Rousset, T. Semmler, J. Stroeve, T. Toyoda, B. Tremblay, H. Tsujino, M. Vancoppenolle, and S. Community, 2020: Arctic sea ice in CMIP6. *Geophysical Research Letters*, **47**, 11, doi:10.1029/2019gl086749.

Panzer, B., D. Gomez-Garcia, C. Leuschen, J. Paden, F. Rodriguez-Morales, A. Patel, T. Markus, B. Holt, and P. Gogineni, 2013: An ultra-wideband, microwave radar for measuring snow thickness on sea ice and mapping near-surface internal layers in polar firn. *Journal of Glaciology*, **59**, 244–254, doi:10.3189/2013JoG12J128.

Parmenter, R. R. and M. D. Coon, 1972: Model of pressure ridge formation in sea ice. *Journal of Geophysical Research*, **77**, 6565–6575, doi:10.1029/JC077i033p06565.

Perovich, D., J. Richter-Menge, and C. Polashenski, 2021: Observing and understanding climate change: Monitoring the mass balance, motion, and thickness of Arctic sea ice. `http://imb-crrel-dartmouth.org`.

Perovich, D. K. and B. Elder, 2002: Estimates of ocean heat flux at SHEBA. *Geophysical Research Letters*, **29**, doi:10.1029/2001gl014171.

Petty, A. A., N. T. Kurtz, R. Kwok, T. Markus, and T. A. Neumann, 2020: Winter Arctic sea ice thickness from ICESat-2 freeboards. *Journal of Geophysical Research-Oceans*, **125**, doi:10.1029/2019JC015764.

Pithan, F. and T. Mauritsen, 2014: Arctic amplification dominated by temperature feedbacks in contemporary climate models. *Nature Geoscience*, **7**, 181–184, doi:10.1038/ngeo2071.

Polashenski, C., D. Perovich, J. Richter-Menge, and B. Elder, 2011: Seasonal ice mass-balance buoys: Adapting tools to the changing Arctic. *Ann. Glaciol.*, **52**, 18–26, doi:10.3189/172756411795931516.

Richter-Menge, J. A., D. K. Perovich, B. C. Elder, K. Claffey, I. Rigor, and M. Ortmeyer, 2006: Ice mass–balance buoys: A tool for measuring and attributing changes in the thickness of the Arctic sea–ice cover. *Ann. Glaciol.*, **44**, 205–210, doi:10.3189/172756406781811727.

Ricker, R., S. Hendricks, V. Helm, H. Skourup, and M. Davidson, 2014: Sensitivity of CryoSat-2 Arctic sea–ice freeboard and thickness on radar-waveform interpretation. *Cryosphere*, **8**, 1607–1622, doi:10.5194/tc-8-1607-2014.

Ricker, R., S. Hendricks, L. Kaleschke, and X. Tian-Kunze, 2017a: CS2SMOS user guide v3.0. doi:10013/epic.51136.

Ricker, R., S. Hendricks, L. Kaleschke, X. Tian-Kunze, J. King, and C. Haas, 2017b: A weekly Arctic sea-ice thickness data record from merged CryoSat-2 and SMOS satellite data. *Cryosphere*, **11**, 1607–1623, doi:10.5194/tc-11-1607-2017.

Rodgers, K. B., S. S. Lee, N. Rosenbloom, A. Timmermann, G. Danabasoglu, C. Deser, J. Edwards, J. E. Kim, I. R. Simpson, K. Stein, M. F. Stuecker, R. Yamaguchi, T. Bodai, E. S. Chung, L. Huang, W. M. Kim, J. F. Lamarque, D. L. Lombardozzi, W. R. Wieder, and S. G. Yeager, 2021: Ubiquity of human-induced changes in climate variability. *Earth System Dynamics*, **12**, 1393–1411, doi:10.5194/esd-12-1393-2021.

Sallila, H., S. L. Farrell, J. McCurry, and E. Rinne, 2019: Assessment of contemporary satellite sea ice thickness products for Arctic sea ice. *Cryosphere*, **13**, 1187–1213, doi:10.5194/tc-13-1187-2019.

Schweiger, A., R. Lindsay, J. L. Zhang, M. Steele, H. Stern, and R. Kwok, 2011: Uncertainty in modeled Arctic sea ice volume. *J. Geophys. Res.-Oceans*, **116**, C00D06, doi:10.1029/2011jc007084.

Schwerdtfeger, P., 1963: The thermal properties of sea ice. *Journal of Glaciology*, **4**, 789–807, doi:10.3189/S0022143000028379.

Screen, J. A. and I. Simmonds, 2010: The central role of diminishing sea ice in recent Arctic temperature amplification. *Nature*, **464**, 1334–1337, doi:10.1038/nature09051.

Semtner, A. J., 1976: Model for thermodynamic growth of sea ice in numerical investigations of climate. *Journal of Physical Oceanography*, **6**, 379–389, doi:10.1175/1520-0485(1976)006<0379:amfttg>2.0.co;2.

Serreze, M. C., A. P. Barrett, A. G. Slater, M. Steele, J. L. Zhang, and K. E. Trenberth, 2007: The large-scale energy budget of the Arctic. *Journal of Geophysical Research-Atmospheres*, **112**, doi:10.1029/2006jd008230.

Shi, H., B. J. Sohn, G. Dybkjaer, R. T. Tonboe, and S. M. Lee, 2020: Simultaneous estimation of wintertime sea ice thickness and snow depth from space-borne freeboard measurements. *Cryosphere*, **14**, 3761–3783, doi:10.5194/tc-14-3761-2020.

Shu, Q., Z. Song, and F. Qiao, 2015: Assessment of sea ice simulations in the CMIP5 models. *Cryosphere*, **9**, 399–409, doi:10.5194/tc-9-399-2015.

Shu, Q., Q. Wang, Z. Y. Song, F. L. Qiao, J. C. Zhao, M. Chu, and X. F. Li, 2020: Assessment of sea ice extent in CMIP6 with comparison to observations and CMIP5. *Geophysical Research Letters*, **47**, doi:10.1029/2020gl087965.

Smith, L. C. and S. R. Stephenson, 2013: New trans-Arctic shipping routes navigable by mid-century. *Proceedings of the National Academy of Sciences of the United States of America*, **110**, E1191–E1195, doi:10.1073/pnas.1214212110.

Smith, R., P. Jones, B. Briegleb, F. Bryan, G. Danabasoglu, J. Dennis, J. Dukowicz, C. Eden, B. Fox-Kemper, P. Gent, M. Hecht, S. Jayne, M. Jochum, W. Large, K. Lindsay, M. Maltrud, N. Norton, S. Peacock, M. Vertenstein, and S. Yeager, 2010: The parallel ocean program (POP) reference manual: Ocean component of the community climate system model (CCSM) and Community Earth System Model (CESM), LAUR-10-01853. `https://www2.cesm.ucar.edu/models/cesm1.2/pop2/doc/sci/POPRefManual.pdf` (last access: 16 december 2022).

Stefan, J., 1891: Ueber die theorie der eisbildung, insbesondere über die eisbildung im polarmeere. *Ann. der Phy.-Berlin*, **278**, 269–286, doi:https://doi.org/10.1002/andp.18912780206.

Stroeve, J., M. M. Holland, W. Meier, T. Scambos, and M. Serreze, 2007: Arctic sea ice decline: Faster than forecast. *Geophysical Research Letters*, **34**, doi:10.1029/2007gl029703.

Stroeve, J. and D. Notz, 2018: Changing state of Arctic sea ice across all seasons. *Environmental Research Letters*, **13**, doi:10.1088/1748-9326/aade56.

Stroeve, J. C., M. C. Serreze, M. M. Holland, J. E. Kay, J. Malanik, and A. P. Barrett, 2012: The Arctic's rapidly shrinking sea ice cover: a research synthesis. *Climatic Change*, **110**, 1005–1027, doi:10.1007/s10584-011-0101-1.

Taylor, K. E., R. J. Stouffer, and G. A. Meehl, 2012: An overview of CMIP5 and the experiment design. *Bulletin of the American Meteorological Society*, **93**, 485–498, doi:10.1175/bams-d-11-00094.1.

Taylor, P. C., R. C. Boeke, L. N. Boisvert, N. Feldl, M. Henry, Y. Y. Huang, P. L. Langen, W. Liu, F. Pithan, S. A. Sejas, and I. V. Y. Tan, 2022: Process drivers, inter-model spread, and the path forward: A review of amplified Arctic warming. *Frontiers in Earth Science*, **9**, doi:10.3389/feart.2021.758361.

Thorndike, A. S., 1992: a toy model linking atmospheric thermal-radiation and sea ice growth. *Journal of Geophysical Research-Oceans*, **97**, 9401–9410, doi:10.1029/92jc00695.

Thorndike, A. S., D. A. Rothrock, G. A. Maykut, and R. Colony, 1975: Thickness distribution of sea ice. *J. Geophys. Res.-Oc. Atm.*, **80**, 4501–4513, doi:10.1029/JC080i033p04501.

Tian-Kunze, X., L. Kaleschke, N. Maass, M. Makynen, N. Serra, M. Drusch, and T. Krumpen, 2014: SMOS-derived thin sea ice thickness: algorithm baseline, product specifications and initial verification. *Cryosphere*, **8**, 997–1018, doi:10.5194/tc-8-997-2014.

Tilling, R. L., A. Ridout, and A. Shepherd, 2018: Estimating Arctic sea ice thickness and volume using CryoSat-2 radar altimeter data. *Adv. Space Res.*, **62**, 1203–1225, doi:10.1016/j.asr.2017.10.051.

Tonboe, R. T., G. Dybkjaer, and J. L. Hoyer, 2011: Simulations of the snow covered sea ice surface temperature and microwave effective temperature. *Tellus a*, **63**, 1028–1037, doi:10.1111/j.1600-0870.2011.00530.x.

Tschudi, M., W. N. Meier, J. S. Stewart, C. Fowler, and J. Maslanik, 2019: Polar Pathfinder daily 25 km EASE-Grid sea ice motion vectors, version 4. *Boulder, Colorado USA. NASA National Snow and Ice Data Center Distributed Active Archive Center [data set]*, doi:10.5067/INAWUWO7QH7B.

Tschudi, M. A., W. N. Meier, and J. S. Stewart, 2020: An enhancement to sea ice motion and age products at the National Snow and Ice Data Center (NSIDC). *Cryosphere*, **14**, 1519–1536, doi:10.5194/tc-14-1519-2020.

Tsujino, H., L. S. Urakawa, S. M. Griffies, G. Danabasoglu, A. J. Adcroft, A. E. Amaral, T. Arsouze, M. Bentsen, R. Bernardello, C. W. Boning, A. Bozec, E. P. Chassignet, S. Danilov, R. Dussin, E. Exarchou, P. G. Fogli, B. Fox-Kemper, C. C. Guo, M. Ilicak, D. Iovino, W. M. Kim, N. Koldunov, V. Lapin, Y. W. Li, P. F. Lin, K. Lindsay, H. L. Liu, M. C. Long, Y. Komuro, S. J. Marsland, S. Masina, A. Nummelin, J. K. Rieck, Y. Ruprich-Robert, M. Scheinert, V. Sicardi, D. Sidorenko, T. Suzuki, H. Tatebe, Q. Wang, S. G. Yeager, and Z. P. Yu, 2020: Evaluation of global ocean-sea-ice model simulations based on the experimental protocols of the Ocean Model Intercomparison Project phase 2 (OMIP-2). *Geoscientific Model Development*, **13**, 3643–3708, doi:10.5194/gmd-13-3643-2020.

Tsujino, H., S. Urakawa, H. Nakano, R. J. Small, W. M. Kim, S. G. Yeager, G. Danabasoglu, T. Suzuki, J. L. Bamber, M. Bentsen, C. W. Boning, A. Bozec, E. P. Chassignet,

E. Curchitser, F. B. Dias, P. J. Durack, S. M. Griffes, Y. Harada, M. Ilicak, S. A. Josey, C. Kobayashi, S. Kobayashi, Y. Komuro, W. G. Large, J. Le Sommer, S. J. Marsland, S. Masina, M. Scheinert, H. Tomita, M. Valdivieso, and D. Yamazaki, 2018: JRA-55 based surface dataset for driving ocean-sea-ice models (JRA55-do). *Ocean Modelling*, **130**, 79–139, doi:10.1016/j.ocemod.2018.07.002.

Turner, A. K. and E. C. Hunke, 2015: Impacts of a mushy-layer thermodynamic approach in global sea-ice simulations using the CICE sea-ice model. *Journal of Geophysical Research-Oceans*, **120**, 1253–1275, doi:10.1002/2014jc010358.

Untersteiner, N., 1964: Calculations of temperature regime + heat budget of sea ice in central Arctic. *Journal of Geophysical Research*, **69**, 4755–4766, doi:10.1029/JZ069i022p04755.

von Albedyll, L., C. Haas, and W. Dierking, 2021: Linking sea ice deformation to ice thickness redistribution using high-resolution satellite and airborne observations. *Cryosphere*, **15**, 2167–2186, doi:10.5194/tc-15-2167-2021.

von Albedyll, L., S. Hendricks, R. Grodofzig, T. Krumpen, S. Arndt, H. J. Belter, G. Birnbaum, B. Cheng, M. Hoppmann, J. Hutchings, P. Itkin, R. B. Lei, M. Nicolaus, R. Ricker, J. Rohde, M. Suhrhoff, A. Timofeeva, D. Watkins, M. Webster, and C. Haas, 2022: Thermodynamic and dynamic contributions to seasonal Arctic sea ice thickness distributions from airborne observations. *Elementa-Science of the Anthropocene*, **10**, doi:10.1525/elementa.2021.00074.

Wang, M. Y. and J. E. Overland, 2015: Projected future duration of the sea-ice-free season in the Alaskan Arctic. *Progress in Oceanography*, **136**, 50–59, doi:10.1016/j.pocean.2015.01.001.

Wang, X. J., J. Key, R. Kwok, and J. L. Zhang, 2016: Comparison of Arctic sea ice thickness from satellites, aircraft, and PIOMAS data. *Remote Sensing*, **8**, 9, doi:10.3390/rs8090713.

Willmes, S. and G. Heinemann, 2016: Sea-ice wintertime lead frequencies and regional characteristics in the Arctic, 2003-2015. *Remote Sensing*, **8**, doi:10.3390/rs8010004.

Wingham, D. J., C. R. Francis, S. Baker, C. Bouzinac, D. Brockley, R. Cullen, P. de Chateau-Thierry, S. W. Laxon, U. Mallow, C. Mavrocordatos, L. Phalippou, G. Ratier, L. Rey, F. Rostan, P. Viau, and D. W. Wallis, 2006: CryoSat: A mission to determine the fluctuations in Earth's land and marine ice fields. *Natural Hazards and Oceanographic Processes from Satellite Data*, **37**, 841–871, doi:10.1016/j.asr.2005.07.027.

Wolf, E. T. and O. B. Toon, 2015: The evolution of habitable climates under the brightening sun. *Journal of Geophysical Research-Atmospheres*, **120**, 5775–5794, doi:10.1002/2015jd023302.

Zhang, J. L. and D. Rothrock, 2001: A thickness and enthalpy distribution sea-ice model. *Journal of Physical Oceanography*, **31**, 2986–3001, doi:10.1175/1520-0485(2001)031<2986:ataeds>2.0.co;2.

Zhang, J. L. and D. A. Rothrock, 2003: Modeling global sea ice with a thickness and enthalpy distribution model in generalized curvilinear coordinates. *Mon. Weather Rev.*, **131**, 845–861, doi:10.1175/1520-0493(2003)131<0845:mgsiwa>2.0.co;2.

Zhou, L., S. M. Xu, J. P. Liu, and B. Wang, 2018: On the retrieval of sea ice thickness and snow depth using concurrent laser altimetry and L-band remote sensing data. *Cryosphere*, **12**, 993–1012, doi:10.5194/tc-12-993-2018.